Novel lab-on-a-chip design for biomolecular diagnosis

Bekou, Sofia

Award date:
2019

Awarding institution:
University of Bath

PhD 2019 S. BEKOU

Front cover

NOVEL LAB-ON-A-CHIP DESIGN FOR BIOMOLECULAR DIAGNOSIS

SOFIA BEKOU

A THESIS SUBMITTED FOR THE DEGREE OF DOCTOR OF PHILOSOPHY

UNIVERSITY OF BATH

DEPARTMENT OF CHEMICAL ENGINEERING

JANUARY 2019

SUPERVISORS: PROF. DAVIDE MATTIA

DR. PEDRO ESTRELA

COPYRIGHT

To My Son, Nikolaos Ioannis

Στο γιό μου, Νικόλαο Ιωάννη:

Στη ζωή σου μπορείς να πετύχεις τα πάντα,

φτάνει να το θές.

By believing passionately in that which doesn't exist,

you create it (N. Kazantzakis). That’s also research.

Acknowledgements

This work was supported by **EPSRC** funding.

I would like to thank my husband Dr. Fanis Tsoligkas for his support and love throughout these years. And then, my family Athanasios, Maria and Michalis for being there in all the steps of my life.

I would like to thank my supervisors Prof. Davide Mattia and Dr. Pedro Estrela for this great collaboration.

Davide's research group: Hannah, Kah Peng, Daniel et el was the best. We spent together precious moments.

I would like to thank all the technical team of the departments of Chemical Engineering, Physics and Electrical and Electronics Engineering for their assist on this PhD research with their important advice, support and help.

Abstract

This research thesis was conducted to design and fabricate a novel design of a lab-on-a-chip microfluidic device to enable blood separation and blood analyses at the nanoscale via nanopores integrated into microchannel. Furthermore, the same lab-on-a-chip microfluidic device could be used for blood examination and diagnoses by changing just one step during the fabrication. The development of the novel lab-on-a-chip device able to carry out a range of biomolecular analyses, providing reliable results, incorporates nanochannels obtained via an innovative manufacturing process, combining traditional micro-fabrication methods and electrochemical anodization. The lab-on-a-chip device consists of glass substrate sealed with poly-dimethyl siloxane (PDMS) in which microchannels have been etched. The different metals deposited determined the use of the device. Physical vapor deposition was applied to deposit either aluminium or gold. The aluminium has been anodized inside the microchannel to obtain nanoporous alumina channels. The gold metal has been used for biosensing experiments. DNA aptamers were attached to the gold using thiol ligands, enabling the detection of ochratoxin-A and A-human thrombin. Cyclic voltammetry and electrochemical impedance spectrometry have been used to detect both biomolecules. The shift of the curve confirms the presence of the biomolecule. When sodium chloride was used to wash away the A-human thrombin, the curve went back to the initial measurement when only the DNA aptamer was present, enabling repeat use of the device.

Table of Contents

ACKNOWLEDGEMENTS IV

ABSTRACT IV

LIST OF FIGURES VIII

LIST OF TABLES XIV

1. INTRODUCTION AND THESIS STRUCTURE 1

1.1 Thesis Structure 2

2. LITERATURE REVIEW 4

2.1 Fundamentals of microfluidics devices 4

2.1.1. Introduction 4

2.1.2. Physics and Modelling 6

2.1.3. Microfluidics' Components 8

2.1.4. Fabrication Techniques of Microfluidic Devices 8

2.1.5. Biological Applications of Microfluidic Devices 16

2.1.6. Conclusion 18

2.2 Separation in microfluidics devices 18

2.2.1. Introduction 18

2.2.2. Passive Techniques of Microfluidics Separation 19

2.2.3. Active Techniques of Microfluidics Separation 20

2.2.4. Combined Techniques of Microfluidics Separation 23

2.3 Biosensing in Microfluidics Devices 24

2.3.1. Introduction 24

2.3.2. Biosensors Categorization 25

2.3.3. Microfluidics Integration with Biosensor Technology 29

2.3.4. Conclusion 34

2.4 Separation using Anodized Nanomaterials 35
2.4.1. Introduction 35
2.4.2. Nanoporous Anodic Aluminium Oxide Structure and Fabrication 36
2.4.3. Nanoporous Anodic Alumina Properties, Surface Functionalization and Surface Chemistry 39
2.4.4. Separation 43
2.4.5. Conclusion 45

3. MATERIALS AND METHODS 47

3.1 Lab-on-a-chip device fabrication 47
3.1.1. Fabrication of microhills by wet chemical etching 47
3.1.2. Surface profile measurement of the microhill 55
3.1.3. Fabrication of microchannels using poly-dimethyl-siloxane 56
3.1.4. Physical vapor metal deposition on the wafer 58
3.1.5. PDMS and glass surface exposure to oxygen plasma 64
3.1.6. Wire connections and holes punched to reach the microchannels 72

3.2 Lab-on-a-chip for aluminium anodization 75
3.2.1. Aluminium anodization 75

3.3 Lab-on-a-chip with gold for biosensing 77
3.3.1. Recognition and capture of ochratoxin A 80
3.3.2. Recognition and capture of α-human thrombin 82

3.4 Conclusions 85

4. RESULTS 86

4.1 Lab-on-a-chip devices 86
4.1.1. Lab-On-A-Chip Device Fabrication 86
4.1.2. Fabrication of microhills by wet chemical etching 87
4.1.3. Microchannel Fabrication using poly-dimethyl-siloxane (PDMS) 89
4.1.4. Physical Vapour Deposition of Metal on the Wafer 89
4.1.5. Oxygen Plasma exposure of PDMS and Glass Surface 94
4.1.6. Wires connection and holes punched to reach the microchannels 94
4.1.7. Lab-on-a-chip for Aluminium anodization 97
4.1.8. Aluminium and titanium metals 102

4.1.9. Aluminium and zinc metals 104
4.1.10. Aluminium with silicon dioxide 110

4.2 Biomolecular diagnosis 113
4.2.1. Recognition and capture of ochratoxin A 113
4.2.2. Recognition and capture of α-human thrombin 119
4.2.3. Discussion 129

4.3 Oxygen Plasma Equipment Fabrication 129

5. CONCLUSIONS 131

6. FUTURE WORK 133

APPENDICES 135

Appendix 1 135
Publication 135
Conferences & Workshops 135

Appendix 2 136
Cleanroom definition 136

Appendix 3 136
Calculations for Nernst equation 136
Calculation for electrochemical impedance spectroscopy and cyclic voltammetry 137

7. REFERENCES 139

List of figures

Figure 1. the three main steps of the photolithography procedure. 9

Figure 2. State of art fabrication of microfluidic devices by Injection moulding, hot embossing and soft lithography 12

Figure 3. Process flow for PDMS stamp fabrication from a silicon master 14

Figure 4. Demonstration of the injection moulding process 15

Figure 5. Representation of the components of a biosensor including transducers, detectors and bio-recognition elements 25

Figure 6. a. Nanoporous AAO structural characteristics 37

Figure 7. The fabrication procedure to make microhills on a glass surface 48

Figure 8. Different etched geometries after isotropic and anisotropic etching 49

Figure 9. a) UV rays attack the photoresist layer giving a minimum error of a couple of nanometres, instead in b) the beam of rays attacks a much wider surface area..... 52

Figure 10. Standard dimensions of the photomask and exposure area that can be effectively uncovered and attacked by UV light. 53

Figure 11. a) Stylus profilometer. b) The graph of the microhill profile with dimensions of the microhill; 1 mm width and 4 μm height 56

Figure 12. Working with PDMS: a) the liquid mixture after stirring in air with visible air bubbles; b) after one hour under vacuum air bubbles are removed and the mixture became transparent. 57

Figure 13. The electron beam evaporator on the right-hand side and its power supply on the left hand side 59

Figure 14. Oval shaped nanopores, due to insufficient vacuum in the chamber during metal deposition .. 60

Figure 15. Metal deposition inside the glass microchannel using a copper mask in order to protect the sample and leave exposed only the part where the metal should be deposited. 62

Figure 16. The metal deposition method on a glass surface using a copper shadow mask in order to obtain the deposition in the determined area of the sample with predetermined design. 63

Figure 17. Zepto plasma equipment..... 65

Figure 18. Schematics to show the oxygen plasma bonding process with a) the metal deposited on the glass surface and b) on PDMS. 65

Figure 19. The poly-dimethyl siloxane (PDMS) chemical formula in which the outer methyl groups changes to hydroxyl groups after oxygen plasma exposure known as surface oxidization. 67

Figure 20. Permanent bond occurs between PDMS and glass surfaces after oxygen plasma treatment and heating..... 68

Figure 21. Traces of PDMS on glass surface after peeling is an indication of the irreversible bond and permanent adhesion. The thickness of the PDMS in this picture is 1.6 mm..... 69

Figure 22. Fluorescent dye dissolved in DI water and flowed inside the microchannel to capture the filling of the microchannel with water. 70
Figure 23. Contact angle measurement on a solid flat surface..... 71
Figure 24. Contact angle measurements 72
Figure 25. Lab-on-a-chip with aluminium layer deposited in the middle of the cross, connected with electrodes and tubing fitted across the other microchannel. 73
Figure 26. Three methods to introduce wires into the device..... 74
Figure 27. A syringe pump connected to the lab-on-a-chip, to pump acid inside the microchannel in order to carry out aluminium anodization. 76
Figure 28. The device containing a gold layer and electrodes across the gold with deposited titanium. 78
Figure 29. Chemical structure of ochratoxin A; structurally consists of a para-chlorophenolic group containing a dihydroisocoumarin moiety that is amide-linked to L-phenylalanine..... 80
Figure 30. Structure of complex involving α-human thrombin in blue 80
Figure 31. Two electrode cell set up using a sample with wires as electrodes 81
Figure 32. Schematic to represent a) the immobilization procedure b) for immobilizing DNA on the gold surface and c) capturing of ochratoxin A. 82
Figure 33. Profilometer measurement shows the microhill with depth 4 μm and width 1 mm. 86
Figure 34. Picture taken under Zeiss microscope using 10x lens. The glass substrate anisotropically etched, showing microhills on the surface. 88
Figure 35. The metal deposition on the PDMS surface initially gave inconsistent results, with both (a) a uniform layer and (b) a broken, flaky one, which also damaged the PDMS. 92
Figure 36. The picture is taken under Zeiss optical microscope, using 20x lens, and show of the layer of metal deposited on a glass surface. 93
Figure 37. Representation of the aluminium surface before anodization using FESEM. 93
Figure 38. Three different electrode assemblies used: a) shows the Ti deposited metal layer throughout the channel with the determining metal layer; b) shows the part with the determining metal layer connected with a Ti deposited layer and the other part with a Ti wire fitted; and c) shows Cu and Ti wires connected to the device. 96
Figure 39. The holes of the lab-on-a-chip where fitted with tubing and sealed with silicon glue..... 97
Figure 40. Aluminium anodization procedure. 98
Figure 41. The graph shows the current against the time of the aluminium anodization in 0.5M Sulphuric acid at 20 V for 1 hour. The experiment was performed at room temperature (with sporadic cooling). 100

Figure 42. The picture shows the SEM representation the anodized aluminium to alumina nanopores (Al_2O_3) on the right hand side and on the left hand side shows the metallic aluminium (Al) which is not anodized. 100
Figure 43. Anodized alumina; it can be seen the long pores up to 1µm and the nanodomes on top making the barrier layer. 101
Figure 44. The graph shows the aluminium anodization in 0.5M Sulphuric acid by applying 20V current for 1 hour, performed at room temperature (with sporadic cooling)..... 102
Figure 45. SEM of alumina nanodomes (Al_2O_3) and a flaky layer of titanium (Ti) on top. 103
Figure 46. SEM micrograph of Ti nanodomes covering the alumina anodized structured. The bright edges are alumina nanochannels and the opaque surface is porous alumina. 104
Figure 47. Aluminium-Zinc layer under optical microscope, an n-Plan lens was used. 105
Figure 48. The graph shows the current against the time of the aluminium anodization, performed in sulphuric acid, in 20V for 20min. 106
Figure 49. The SEM micrograph shows a zinc oxide petal structure 107
Figure 50. The SEM micrograph shows two types of ZnO structure one following the other in the same sample surface. On the left-hand side is the ZnO petal structure and on the right porous ZnO. 108
Figure 51. Elemental line analysis on the sample 108
Figure 52. Alumina layer with zinc oxalate stone-like structure on top. The inset at the top right of the picture shows a closer view of the alumina, which is shiny, and the zinc oxalate 109
Figure 53. The procedure to roughen the glass surface in a specific area..... 111
Figure 54. Glass surface after 2 minutes HF treatment 112
Figure 55. Alumina layers after anodization. The opaque grey with pores is porous alumina, the shiny part with dark on the bottom are SiO_2, and the Ti-dark layer. 113
Figure 56. A syringe was used to pump the solution continuously through the microchannel and out to a collection vial. 114
Figure 57. The cyclic voltammetry measurement for the Ochratoxin A is shown in the graph. This is the representation of the quantity of the developed electric charge in the electrochemical cell where: only phosphate buffer was in the microchannel across the electrodes, CV1, the DNA-aptamer was added in the microchannel, CV2, and when the ochratoxin A was in the microchannel, CV3. 116
Figure 58. Electrochemical impedance spectroscopy measurements. The blue diamond shape is for phosphate buffer, the red circle shape is for DNA chain and the green triangle is for ochratoxin A. 117
Figure 59. The graph shows the decrease of the capacitance over the range of frequencies..... 118
Figure 60. The resistance in between the electrodes increases as the frequency increases. 118
Figure 61. The graph shows the change of the surface properties of the electrode by conducting EIS measurement in between the electrodes 121

Figure 62. EIS measurement shows the interaction of the analyte with the molecules immobilized on the electrodes surface 122
Figure 63. Three electrode cell set-up of the device, consists of a working gold electrode, a counter and a reference platinum electrode. 123
Figure 64. The three-electrode cell set-up is presented 124
Figure 65. EIS measurements 125
Figure 66. Three-electrode cell set up with electrodes: gold (Au) as working, platinum (Pt) as counter and silver (Ag) as reference. 126
Figure 67. EIS measurements of α-human thrombin in a three-electrode cell set-up with electrodes gold (Au) as working, platinum (Pt) as counter and silver (Ag) as reference 127
Figure 68. Capacitance measurements of α-human thrombin in a 3-electrode cell set-up with electrodes gold (Au) as working, platinum (Pt) as counter and silver (Ag) as reference 128
Figure 69. The sample chamber fabricated in the lab can be seen here 130

List of abbreviations

AAO	Anodic Aluminium Oxide
ALD	Atomic Layer Deposition
anti-AI	Avian Influenza Antibodies
BioMEMS	Biological Microelectromechanical systems
BOE	Buffered Oxide Etch
CNT	Carbon Nanotubes
CV	Cyclic Voltammetry
CVD	Chemical Vapour Deposition
DEP	Dielectrophoresis
DI water	Diionized Water
DNA	Deoxyribonucleic Acid
e-beam	Electron Beam
E. coli	Escherichia Coli
EDTA	Ethylenediaminetetraacetic Acid
EIS	Electrochemical Impedance Spectroscopy
EOF	Electroosmotic Flow
FACS	Fluoreschent Activated Cell Sorting
FET	Field Effect Transmition
FIB	Focused Ion Beam
FITC-BSA	Fluorescein Isothiocynate-Bovine Serum Albumin
HCl	Hydrochloric Acid
HF	Hydrofluoric Acid
ICP	Inductively Coupled Plasma
IgE	Immunoglobin E
MCH	Mercapto Hexanol
MEMS	Microelectromechanical Systems
MPTES	Mercapto Silane
MT-DACS	Multitarget Dielectrophoresis Activated Cell Sorter
OEPFF	Optically Enhanced Pinched Flow Fractionation
OTA	Ochratoxin A
PCR	Polymerase Chain Reaction
PDMS	Polydimethyl Siloxane
PEG	Polyethyleneglycol
PEI	Polyethylenimine
PEI-NAA	Polyethylenimine-Nanoporous Anodic Alumina
PEM	Polyelectrolyte multilayer
PFF	Pinched Flow Fractionation
PMMA	Polymethyl Methacrylate

POC	Point of Care
PSG	phosphorus Silicate Glass
pSi	porous Silicon
PVD	Physical Vapor Deposition
QCM	Quartz Crystall Microbalance
RF	Radio Frequency
SAM	Self Assembled Monolayer
SELEX	Systematic Evolution of Ligands by Exponential Enrichment
SERS	Surface-Enhanced Raman Scattering
SWV	Square Wave Voltammetry
TAFI	Thrombin Activable Fibrolysis Inhibitor
TiNT	Titanium Nanotubes
UV	Ultra Violet
µTAS	micro Total Analysis Systems

List of tables

Table 1. Examples of bio-sensitive recognition elements used in microfluidic devices..... 28

Table 2. Colour characterization of plasma purity and oxygen flow purity. 66

Table 3. Common Electrical elements 79

Table 4. The crucible type and the amount of current used for each different metal, using thermal and e-beam evaporators. The crucible type differs for each different metal in order to remain inert during the evaporation process. 91

1. Introduction and Thesis Structure

As part of the broader trend towards personalized medicine and decentralized treatment, a key requirement is the development of simple lab-on-a-chip designs yet capable of conducting a wide range of laboratory analyses, with short response time and high reproducibility. The ability to conduct different laboratory analysis gives the opportunity to use it for more than one operation. Lab-on-a-chip is an abbreviation of the phrase laboratory on a microchip device which means the embodiment of a laboratory function or equipment on a miniaturized chip. The overall aim of this research was to manufacture a simple lab-on-a-chip device with the ability to carry out different analyses and provide consistent and reliable results, relatively easy to make and use, cost- and analysis time- effective, and requiring reduced analyte quantities. The aim of this work was achieved by meeting the following objectives:

1. To manufacture a lab-on-a-chip device with parallel metal oxide nanochannels for biomolecular separation based on molecular size, using the anodization of aluminium.
2. To manufacture a lab-on-a-chip device for integrated biosensing applications using gold functionalised with immobilised DNA-aptamers.

For all fabricated devices, the metal was precisely placed inside the microchannel with metal deposition, using physical vapour deposition (PVD). By using PVD, the metal passes from the solid phase to vapor phase by evaporation or sublimation and then back to the solid phase. The final stage of solidification is where the thin metal film is formed. The device was composed of a glass substrate where the microchannels were implemented, and the thin metal film was deposited, and a sealing layer made from poly-dimethyl siloxane (PDMS) was

attached and stuck permanently on the glass using oxygen plasma. Oxygen plasma cleaned both surfaces, changing their chemical properties making them very hydrophilic, resulting in a permanent bond. This technique offered a hermetical and irreversible seal to the device in between the two surfaces.

1.1 Thesis Structure

Chapter two contains an extensive discussion of the history of miniaturized devices, the challenges faced throughout the years of development and an analysis of other academic work related to the subject. The literature review chapter provides an overview of current state-of-the-art lab-on-a-chip devices and their improvement throughout the years. This analysis highlighted a gap in the research, the need for inexpensive, easy to assemble devices which were also reusable and reliable. The research presented here has made a significant contribution towards achieving such a device.

Chapter three contains a detailed description of all the materials and techniques used to fabricate the devices. The fabrication of each device and the optimization of each step are shown which lead towards the goal of offering reproducibility for all samples reported.

Chapter four reports on all results, including each step of the lab-on-a-chip fabrication: microhills fabrication by wet chemical etching, microchannels fabrication using poly dimethyl siloxane (PDMS) elastomer, metal deposition on the wafer using physical vapour deposition, PDMS and wafer surface treatment using oxygen plasma and wires connection as the final step to close and seal the device and start the analysis. Reusable devices were investigated as part of the biosensing investigation.

The final chapter concludes the work, where a summary of all significant findings is presented, giving the reader an overall view of this thesis and its outcomes. Suggestions for future work are also included.

2. Literature Review

2.1 Fundamentals of microfluidics devices

2.1.1. Introduction

The term microfluidics describes the research discipline that is concerned with transport phenomena occurring at microscopic scales (1-500 μm) including techniques and components used in the control and actuation of fluids. Categories such as micro total analysis systems (μTAS) or lab-on-a-chip use microfluidics which rests on the premise of fluid manipulation and analysis in microchannels. A micro total analysis system is a system which is capable of compressing an entire laboratory work into a chip, also known as lab-on-a-chip. Due to its small size it helps save on space, offers time and cost of required technologies. The fluid flow at the microscale is performed through microchannels. These microchannels are microfabricated through the use of techniques borrowed from plastic and semiconductor industries (Pierce and Zhao, 2011), for example, photolithography, micromachining, injection moulding, replica moulding and embossing (Addae-Mensah, et al., 2010).

Microfluidic technologies demonstrate that fluidic devices could be integrated and miniaturized together, therefore, generating an idea of supporting the possibility of fitting the whole “laboratory on a chip”. The whole “laboratory on a chip” means the incorporation of one or more laboratory function on a single chip. The “lab-on-a-chip” is similar to the idea of a microelectronic circuit which is a whole computer on a chip. Moreover, the miniaturization science was initially triggered by the microelectronics industry following the production of miniature silicon-based electronic devices (Terry et al., 1979). Silicon

miniaturization and fabrication techniques were then extended to mechanical device fabrication, also referred to as microelectromechanical systems (MEMS). MEMS technology later evolved allowing the fabrication of devices that could be used in the fields of medical and life sciences. The devices fabricated for use in the fields of medical and life sciences were specifically referred to us as biological microelectromechanical systems (BioMEMS). BioMEMS' broad definition would include applications and devices fabricated through the use of modern microfluidics techniques developed in the 1990s by Manz and his colleagues (Harrison et al., 1993).

Nanofluidics emerged recently following developments in the field of nanotechnology. Nanotechnology refers control of matter at the scales of 1-100 nm. This means that the difference existing between nanofluidics and microfluidics is the scale of the systems, which can result in a major difference in the flow behaviour of liquids at the nanoscale compared to that of the microscale. In the early 20th century Majumder and his colleagues proved that the liquid flow behaviour at the nanoscale is four to five orders of magnitude faster than the predicted behaviour at the macroscale using the classical Hagen-Poiseuille fluid-flow theory (Majumder et al., 2005).

Techniques, Scientific Aspects and Commercialization of lab-on-a-chip Technology

The areas of microfluidics and MEMS have stretched beyond the traditional fields of pressure sensors and inkjet heads (Bassous et al., 1977) to fields of protein crystallization, drug delivery, cell culture, chemical synthesis, proteomics, drug discovery, point-of-care diagnostics, genomics and genetic sequencing. Microfluidics can change the techniques used in pharmaceutical industries for screening drugs and targets, allowing for the increase in

performance. The above-mentioned performance increment is a result of being able to conduct parallel experiments at increased speed and high-throughput, with minimal reagents used per chips. This level of performance cannot be achieved with benchtop techniques (Mohammed et al., 2015).

The development of fluidic systems at the microscale, their advantages and the reliability have had a profound impact on the scientific community. Microfluidics use has become common amongst biologists, engineers, physicists and chemists. Microfluidics use in the above-mentioned fields has made it a multidisciplinary platform facilitating the advancement of various scientific and engineering fields. Additionally, microfluidics utilization has facilitated the progress of understanding the theory and the applications of fluid dynamics. Microfluidics technology is being used by the life scientists to investigate phenomena in a controlled and well-defined environment at the single-cell level. Microfluidics technology has enabled the biophysicists and chemists to conduct protein crystals growth and analysis, and DNA sequencing in a time-saving manner. The significance of microfluidics from the mid-1990s to the current time is evident from the large and consistent progress of publications in journals and conferences (Nguyen and Wereley, 2006).

2.1.2. Physics and Modelling

Microfluidics can be understood through the analysis of microscale fluid flow including the consideration of forces that come into play at this microscale dimension. Notably, the inertial forces are dominant in large dimensions. However, a reduction in dimension increases the dominance of the surface forces due to the increase in surface area in relation

to volume ratio. The surface viscous forces and body force are compared using the Reynolds dimensionless number (H.A. Stone et al., 2004).

The reduction in dimensions increasingly challenges the assumption of continuity. Fluid modelling approaches are divided into two major classes namely molecular-level models and continuum models. Navier-Stokes equations are used in the generation of most continuum models (Peyret, 1996). The continuum models show an assumption that there is no discontinuity among discrete molecules. The continuum models' assumption becomes valid when the system's dimension is greater than the molecular dimension. This means that the assumption is not valid in a scenario where the molecular dimension and system's dimension are comparable. Molecular-based models can be statistical, hybrid, or deterministic when considering the simulation of small dimensional systems. The Knudsen number is the dimensionless number that can be used in determining a more appropriate model between discrete molecular and continuum flow models (Kumar, 2010).

Modelling Approaches

Independent variables namely density, pressure, and velocity are used to define continuum models. The independent variables are determined for all nodes of the fluid element per time step. Smaller elements are more accurate when considering the simulations of a finite element relative to the complexity of the computational procedure. The conservation of momentum and mass, in this case, would be expressed as shown below:

$$\mathbf{d_\rho/d_t + \nabla.\ (\rho\mu) = 0}\ \textbf{the continuity equation} \qquad \textbf{[1]}$$

Where μ is the fluid velocity, ρ is the fluid density, while p is the pressure. Navier-Stokes equation in viscous flow is represented by a partial differentiation equation of a second-order requiring two boundary conditions (Peyret, 1996). The normal component of velocity at the

impermeable boundaries is initially set to zero. The Navier-Stokes equation in the target area is solved using the extra tangential boundary conditions. The second boundary condition in the case of continuum flow represents the no-slip boundary condition. The assumption holds for a low value of Knudsen number (Kn<0.1).

2.1.3. Microfluidics' Components

A wide variety of microfluidic components, for example, micromixers and micro-pumps have been produced since the implementation of microfluidic technology. The microfluidics' components facilitate accurate fluids manipulation and control. The design of these components depends on the intended use of a microfluidic device, type and volume of fluid.

Actuation of Fluid

Fluids are driven through microfluidic systems using different techniques. External syringe pumps are normally used in driving fluids through the system of microfluidic devices (Seyed-Yagoobi, 2005). The design and fabrication of micropumps is based on several crucial parameters, for example, efficiency, dealing with back pressure, power consumption and ability to attain maximum flow rates. (Yobas et al., 2008, Jang and Yu, 2008, Chang et al., 2007, Lin et al., 2014).

2.1.4. Fabrication Techniques of Microfluidic Devices

Glass, hard plastics, elastomeric polymers, and silicon are materials commonly used in microfluidic device fabrication. Lithography techniques are needed in the micro fabrication of microfluidic devices based on the above-listed materials.

Lithography Method of Microfluidic Device Fabrication

Lithography is a fundamental technique of nano- and microstructure fabrication. Lithography is classified based on the type of energy applied in the illumination process: ion beam lithography, electron beam lithography (e-beam lithography), deep UV lithography, X-ray lithography and soft photolithography (McDonald et al., 2000). X-ray lithography and photolithography are the commonly used lithography techniques in microfluidic device fabrication. However, deep UV and e-beam lithography techniques are becoming important in the production of submicron fluidic structures. The photolithographic microfluidic device fabrication procedure is conducted using three major steps (Figure 1):

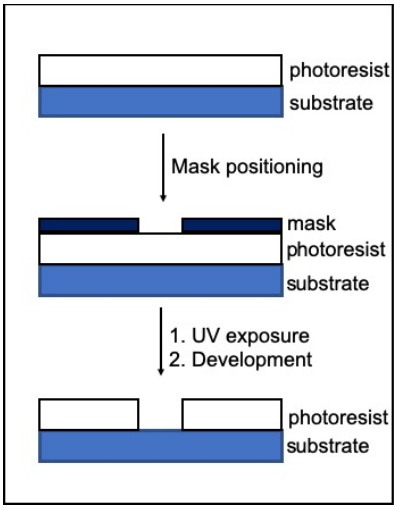

Figure 1. The three main steps of the photolithography procedure.

- Positioning- This step involves the alignment of a photolithography mask with the substrate being coated with a photoresist material.

- Photoresist exposure- The substrate is exposed to UV-light.

• Development Process- The development process involves the generation of a pattern on the photoresist material by etching.

Silicon-Based Method of Microfluidic Device Fabrication

This method of fabrication involves bulk micromachining or surface micromachining.

Bulk Micromachining

Bulk micromachining is a subtractive technique by the removal of silicon material to generate the desired structure. The selective removal is guided by a patterned photoresist material that shields other silicon from the etchant. After the etching process of the exposed silicon material, the photoresist material is removed to give the final microstructure. There are two methods of etching: wet chemical etching and dry reactive ion etching. Wet chemical etching removes silicon material on the basis of its crystalline structure. The anisotropic etching process is used in wet chemical etching depending on the orientation of silicon crystals to produce various channel geometries. Dry reactive ion etching is independent of the silicon crystal orientation. Dry reactive ion etching is done using chemical vapor at standard or cryogenic temperatures. (Kovacs et al., 1998)

Surface Micromachining

Surface micromachining is an additive process that involves materials such as single crystal silicon, phosphorus silicate glass (PSG) and polysilicon (Bustillo et al., 1998). The surface micromachining process is conducted in four steps: substrate passivation, deposition and patterning of a sacrificial layer, doping and stress annealing of the deposited polysilicon structure, and etching of the deposited sacrificial layer to release the final microstructure.

Glass-Based Method of Microfluidic Device Fabrication

Glass is a suitable microfluidics material due to its chemical resistivity, stability at high temperatures, high electrical resistivity, and optical transparency. Additionally, glass as a microfluidic material possesses commendable biological compatibility features that make it suitable for clinical and medical application. Glass based methods of microfluidic device fabrication are similar to the silicon's bulk micromachining technique. However, the mask pattern is placed on the glass material for the channel micromachining process, and then a metal film is evaporated, for example, gold, chromium or polysilicon (which is not a metal, but it can be deposited as a thin film with the evaporator). The pattern is made, and the glass etching is done using buffered oxide etch (BOE). BOE consists of hydrofluoric acid and ammonium fluoride. Etching of glass using BOE is an isotropic process. The patterned glass is covered using another piece of glass containing drilled access holes. The final microfluidic chip is formed once the etched glass piece and its cover piece are aligned and stuck together. However, cheaper and faster glass-based microfluidic device fabrication techniques are being invented, for example, substituting evaporated metal films with hardened photoresist as the etch mask (Bahadorimehr and Majlis, 2011).

Polymer-Based Methods of Microfluidic Device Fabrication

Polymers are a more cost effective alternative to silicon and glass. The techniques used in the fabrication of polymer-based microfluidic devices include soft lithography and thick polymer photoresist techniques (Haraldsson, 2005).

Soft Lithography Techniques

Polydimethylsiloxane (PDMS) is an elastomeric polymer and therefore the technique is known as soft lithography (Bratton et al., 2006). The main procedural steps of the soft lithography technique are:

• Master moulds are produced using a thick polymer photoresist.

• PDMS liquid is placed into the master mould.

• PDMS liquid is then oven-cured to produce a thick polymer photoresist pattern.

• The patterned PDMS is peeled off and stuck on a flat glass piece hence forming a microfluidic device.

Other soft lithography techniques include micromoulding in capillaries, solvent-assisted micromoulding, and microtransfer moulding. Figure 2 shows a microfluidic device made by injection moulding, hot embossing and soft lithography.

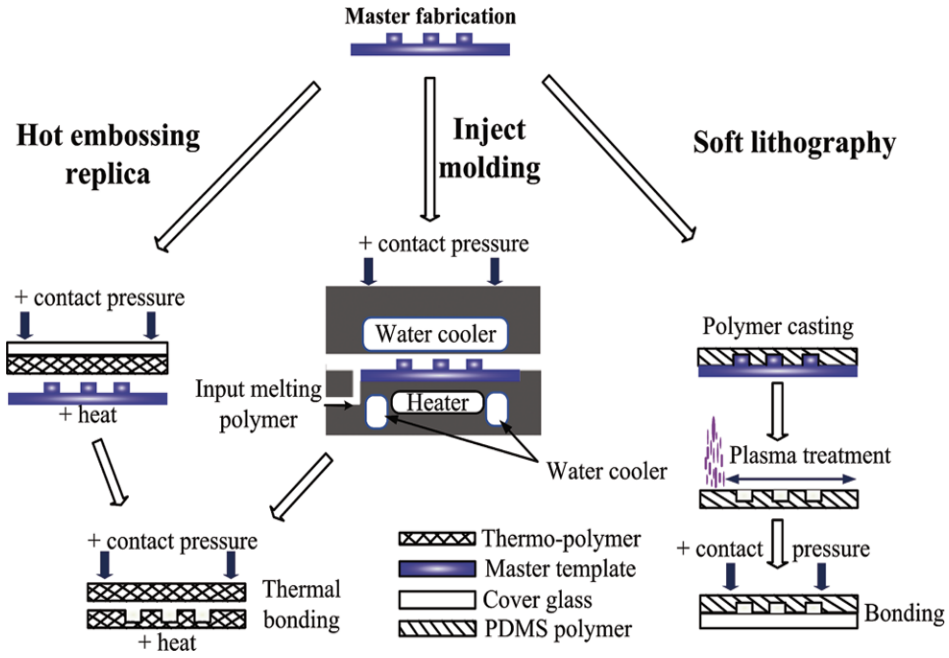

Figure 2. State of art fabrication of microfluidic devices by Injection moulding, hot embossing and soft lithography (Wu and Gu, 2011)

Thick Polymer Photoresist Techniques

These techniques use polymethylmethacrylate (PMMA) polymer as the microfluidic device material. Microfluidic structures are fabricated on the PMMA using collimated X-rays. The mask materials used in this case include titanium and beryllium whose effectiveness is due to their ability to absorb X-rays. The PMMA polymer regions exposed to the X-ray beams are etched depending on the user specification. However, using PMMA requires an expensive source of collimated X-rays, as well as expensive mask materials including titanium and beryllium (Cash Jr, 2000).

Cyclopentanone (SU-8) can serve as a replacement for PMMA since it is cheaper and can be etched using UV-I. Microfluidic device fabrication using SU-8 can be completed within a shorter time compared to PMMA. Figure 3 shows the PDMS stamp fabrication from a silicon template.

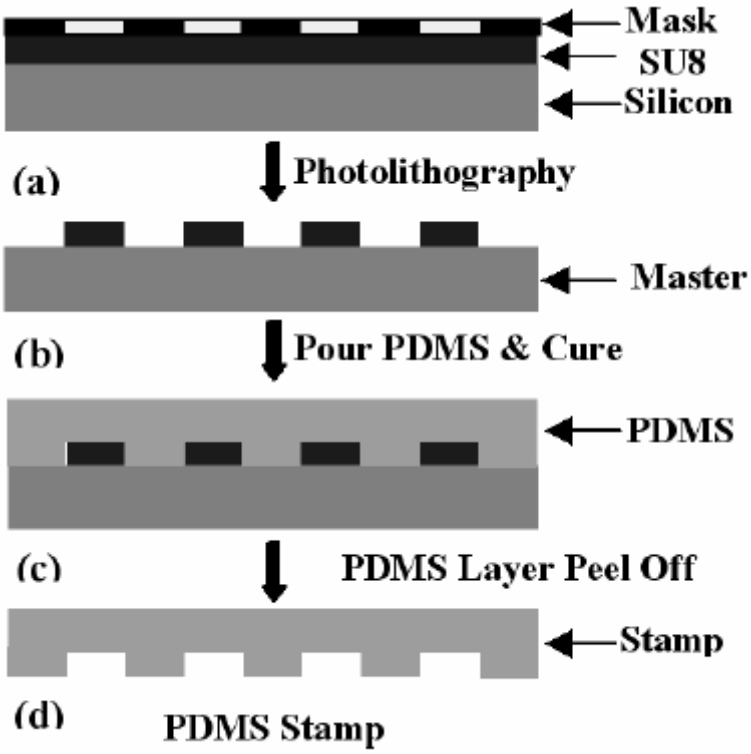

Figure 3. Process flow for PDMS stamp fabrication from a silicon master (Singh et al., 2007)

Plastics in Microfluidic Device Fabrication

The techniques of microfluidic device fabrication using plastics include hot embossing, thermoforming, injection moulding, injection compression moulding and reaction injection moulding. However, the commonly used methods are injection moulding and hot embossing (Sudarsan, 2004). Figure 4 shows the injection moulding procedure.

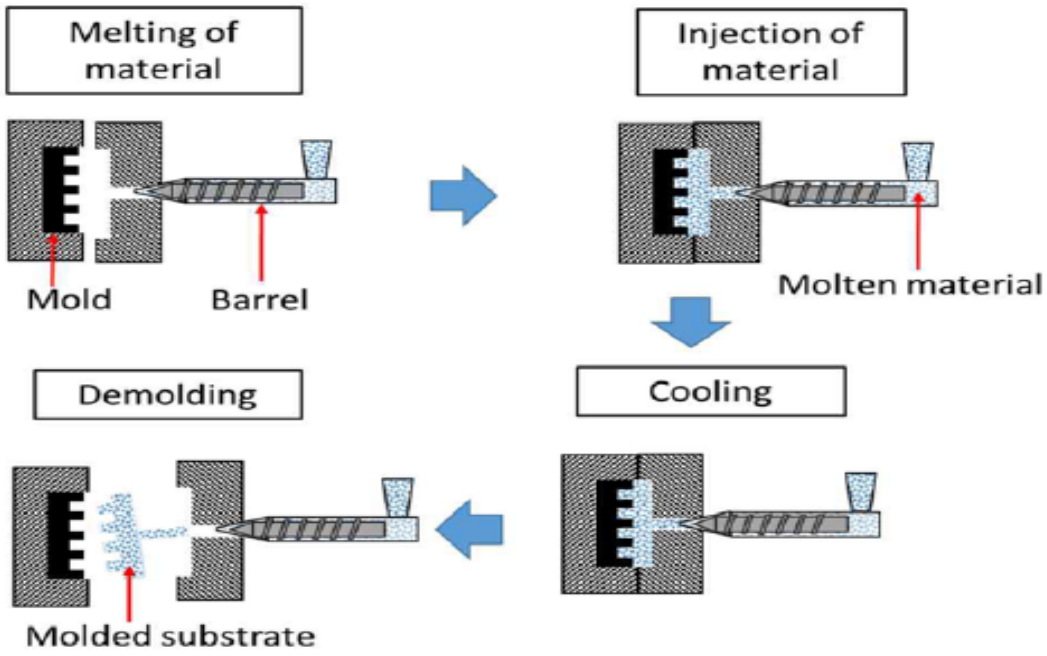

Figure 4. Demonstration of the injection moulding process (Saha et al., 2015). The principal steps are: Melting the material before the mold is injected with material, with both halves of the mould closed; injection, where the material is injected through a hopper into the injection moulding machine; cooling, where the system has to cool down; and the final step is Ejection, where the substrate is ejected from the machine.

Submicron Techniques of Microfluidic Device Fabrication

This is a subtractive technique where bulk material is removed to form the submicron fluidic channels. Examples of submicron techniques include focused ion beam (FIB) micromachining and the laser ablation technique. FIB micromachining is one of the subtractive techniques used to fabricate these submicron fluidic channels. FIB micromachining involves the use of a high-energy ion beam to scan, etch channels and drill holes on the substrate material. The FIB micromachining for example has been used in the fabrication of nanochannels of width 40 nm, length 50 mm and depth 60 nm intended for DNA molecules' manipulation (Winkler et al., 2008).

The laser ablation technique is also used in the fabrication of submicron fluidic channels in nonsilicon-based materials. The micromachining procedure is similar to that of the focused ion beam technique. Laser ablation for example has been used to produce nanochannels of diameters below 700 nm in glass (Dittrich and Manz, 2006b). A couple of limitations when using the laser ablation technique can be the difficulties in removing the ablated materials (Malek, 2006) and the production of rough micromachined structures.

2.1.5. Biological Applications of Microfluidic Devices

DNA Amplification

DNA amplification is made using a range of techniques, the most common being the polymerase chain reaction (PCR) technique, which amplifying small segments of DNA. The advantages of PCR miniaturization (Kim et al., 2006) are: the reduced fabrication cost, the reduced DNA amplification time, the reduced reagent consumption, the increased portability, and the safe PCR reaction vessel disposal.

Immunoassays

Immunoassays are biochemical assays to detect specific proteins and they are used in analyte (protein) measurements (Darwish, 2006). The advantages of microfluidic devices for immunoassay experiments are: reduced sample consumption, reduced experimental cost, and reduced result processing time.

Cell-Based Assays

Cell-based assays are used in the assessment of chemical stimuli effects on biological cells. This assessment helps in the collection of data reflecting a higher level biological response. This assay is commonly used in the pharmaceutical industry in experiments

revolving around drug development (Fujii, 2002). The benefits of using microfluidics in cell-based assays (Zhang and Austin, 2012) are: reduced experimental cost, high quality data, improved control over the three-dimensional cell culture environments, improved biological analysis using multiplexed nanolitre arrays created using microfluidic devices, generation of a high chemical gradient resolution, laminar flow in channels and reduced analyte dilution.

Drug Delivery

The combination of biological science and microfluidics offers a powerful platform for multiple dose drug delivery, precise drug release control, protection of labile active ingredients and elimination of frequent injections. The microfluidic devices offer unique benefits in reagent mixing, sample handling, detection, separation, mobility, and control of reaction rates (Dittrich and Manz, 2006a).

Microfluidic devices fitted with microvalves and micropumps offer drug delivery solutions. These microfluidic devices of drug delivery promote accuracy in dosage, increase the stability of drugs and improve drug therapeutics.

Diagnostics for Point of Care

Use of microfluidic devices in point of care (POC) diagnostics is beneficial in terms of their small size that promotes easier handling, reduced experimental cost, reduced reagent consumption, and shortened analysis time. The portability and accuracy of the microfluidic apparatus in diagnostic tests leads to the correct diagnosis and treatment of diseases (Martinez et al., 2010).

2.1.6. Conclusion

Miniaturization of laboratory processes into a chip has been beneficial to the field of science in general. The microfluidic devices have been fabricated using different materials and procedures making them readily available to users. Microfluidics technology has played a significant role in the field of clinical and medical biology including disease diagnosis and treatment including drug production and drug delivery.

2.2 Separation in microfluidics devices

2.2.1. Introduction

Microfluidic devices play an important role in separation experiments. Bio-separation can facilitate sample purification. The microfluidic device separation technique is used in the fields of food and chemical processing, medical diagnostics, environmental assessment, chemical and biological analysis. The separated biological objects are used in analytical experiments where these objects are studied carefully. The food industry uses separation techniques to prevent the progress of harmful biological activity. Notably, separation experiments are coupled with the sorting of particles into different populations based on their distinct physical properties (Beech, 2011). Medical diagnostics technology utilizes separation techniques to separate normal cells from cancer cells; malaria infected cells from healthy cells and dead cells from the living cells. Diseases normally change cells physical properties hence the necessity for separation. Considering the case of separation of malarial cells from the healthy ones, malarial cells are identified since they are more rigid than the healthy ones. It is this rigidity that makes the infected cells caused by malarial parasites to

block blood capillaries. Additionally, healthy cells have a smaller size compared to the cancer cells. In general, separation of micron-sized particles, droplets, parasites, and cells relies on their size, intrinsic properties and presence of deformities. The performance of microfluidic separation devices is based on applicability, throughput, separation time, and efficiency of particle separation. The separation techniques are broadly categorized as passive, active and combined (Beech, 2011).

2.2.2. Passive Techniques of Microfluidics Separation

The passive techniques of microfluidics separation make use of the interaction of particles, flow field and microchannel structures. Passive techniques of microfluidic separation include pinched flow fractionation (PFF), inertia flow fractionation (two microfluidic techniques which use the laminar flow profile for continuous particles separation by size), micro vortex manipulation, deterministic lateral displacement, the Zweifach-Fung effect (Gossett et al., 2010), filtration, hydrodynamic filtration and micro hydrocyclone effects.

Filtration

The filtration technique facilitates size-based particle separation. Blood fractionation can be conducted using microfabricated filters. Different types of microfilters can be fabricated including weir, membrane, cross-flow and pillar filters (Crowley and Pizziconi, 2005).

Considering plasmapheresis (which is the blood plasma removal, by withdrawing blood from the body, separation into plasma and cells, and transfusion of the cells back into the bloodstream (Nguyen et al., 2012) experiments conducted using a membrane filter, plasma flux formation relies on wall shear rate, transmembrane pressure, and hematocrit. A large hematocrit concentration leads to a reduction in plasma flux. The increase in membrane

pressure increases the plasma flux until a state of equilibrium is reached due to red blood cells' deposition on the filter. An increase in the shear rate leads to the modulation of red blood cells' deposit through shear-enhanced diffusion. The efficiency of the filter face lowers with the particles accumulation. However, the filter membrane can be cleaned through a reverse flow process. An example of a microfiltration membrane device involved the fabrication of microchannels onto PDMS. The microchannels in this device were linked to semipermeable polycarbonate membranes that had a 3-amino propyl triethoxysilane (APTES) coating. This single membrane device was used for plasma separation of a blood sample. The separation of the white blood cells and red blood cells from other blood components was conducted with weir-type and pillar-type microfiltration chips. The blood sample was pumped into the system through an inlet while the red blood cells and white blood cells are collected in different outlets. The microchannel consists of three sub-microchannels made up of two parallel filtration barriers (Di Carlo et al., 2008).

2.2.3. Active Techniques of Microfluidics Separation

The active method of particles separation involves the application of an external field (e.g. electric or magnet) on the particles. The separation is made possible by the fact that particles react differently to the external field and hence have different migration patterns.

Dielectrophoresis Technique

Dielectrophoresis (DEP) is a force that a neutral particle experiences due to magnetic polarization. Magnetic polarization leading to DEP force on a particle can only occur in a nonuniform electric field. This means that the DEP force is zero for a particle placed in a homogenous electric field. The DEP technique is applied in fractionation, following the steps of particle characterization, chemical and biological analytics (Qian et al., 2014). The DEP force is given by the formula:

$$\mathbf{F_{DEP}=2\pi r^3 \varepsilon_m Re\left[\frac{\varepsilon_p^* - \varepsilon_m^*}{\varepsilon_p^* - 2\varepsilon_m^*}\right] E^2} \qquad \mathbf{[2]}$$

Where F_{DEP} is the DEP force, r is the radius of a particle; ε_p^* is the complex permittivity of the particle, while ε_m^* is the complex permittivity of the medium. ε*, in this case, depends on permanent dipolar, electronic, and interfacial mechanism of electrical conductivity and polarization, while E^2 is the rms value of the electric field.

When ε_p^* is greater than ε_m^*, the DEP force occurs in the same direction as the electric field gradient. The positive DEP force leads to the attraction of particles towards a strong electric field. When ε_p^* is less than ε_m^*, the DEP force occurs in an opposing direction to that of the electric field gradient. The negative DEP force leads to the attraction of particles towards a weaker electric field (Doh and Cho, 2005).

The AC field makes DEP versatile. DEP can be applied in various separation activities of particles from a mixture. The separation of particles is based on the frequency-dependent behaviour of the particles' dielectric property. Steric force prevents a particle from advancing past the electrode where it is trapped by the positive DEP. This behaviour of a particle in a

positive electric field can be used in the separation of a single suspended particle. The equation of DEP force evidences the proportionality of the electric field's gradient and the particle's dielectric properties including its radius. This proportionality means that the magnitude of the DEP force on the particle will be dependent on the intrinsic particle's property and size. Two different particles in a mixture may experience different DEP forces. Particles that experience a negative DEP force migrate towards the region of weak field while the particles in the same mixture experiencing positive DEP migrate towards the strong field. This migration tendency of dissimilar particles is known as "differential affinity" and it facilitates their separation. This method has been utilized in the separation of elute cells (Church et al., 2010).

However, the application of the DEP-based technique of particle separation is dependent on the difference in particles' dielectrophoretic response. There are cases where the target and non-target particles exhibit similar DEP response characteristics, making their separation based on their intrinsic properties impossible. This issue is addressed through the use of labelling techniques using labelling beads. An example of such a device is the MT-DACS device for multitarget bacterial separation (Becker et al., 1995).

Magnetic Technique

Separation of particles, specifically blood cells, based on their intrinsic properties can lead to their damage from heat (electrophoresis), membrane pressure (filtration) and shear stress (centrifuging). The magnetic method of separation prevents additional particle damage while providing additional benefits including short separation times and high specificity. Magnetic methods of cell separation require cheaper apparatus compared to other active

techniques (Liu et al., 2007). Fluorescence-activated cell sorting (FACS) is an example of magnetic based method of particle separation (Bonner et al., 1972).

Optical Technique

When a particle is subjected to an incident beam of light, the light is scattered, therefore, causing a change in the light beam's photons. The change in the light beam's photons generates a force. Notably, a beam of light has a Gaussian intensity profile whose value is maximum at the centre where this value reduces away from the centre. When the ratio of a particles' refractive index relative to the medium's refractive index falls below one, the beam scattering generates a scattering force that attempts to attract the particle towards the centre of its profile. This scenario is known as 'optical tweezers'. The 'optical tweezer' effect can be used to separate particles. The separation is facilitated by an adjustment on trap geometry, laser wavelength and power (Xiao and Grier, 2010).

2.2.4. Combined Techniques of Microfluidics Separation

Combined separation techniques i.e. both active and passive are used to produce highly efficient, cost effective and faster devices. An example includes the combination of tuneable electroosmotic flow (EOF) and tuneable pinched flow fractionation (PFF). Such a device can be used in the separation of yeast cells and *E. Coli* bacteria. The PFF can also be optically enhanced to form optically enhanced PFF (OEPFF). Additionally, dielectrophoresis and deterministic lateral displacement techniques can be combined to enable separation efficiency (Adams et al., 2009).

2.3 Biosensing in Microfluidics Devices

2.3.1. Introduction

Biosensors are powerful tools of analysis that have different uses in food safety testing, medical diagnostics, drug discovery, security and defence, environmental and agricultural monitoring (Rana et al., 2010). Biosensors are analytical devices that have the following components:

- Bio-sensitive recognition element- A biomolecule which can be aptamers, nucleic acids, antibodies or enzymes.
- Physicochemical transducer- Immobilizes the bio-sensitive recognition element.
- Detector- The physicochemical transducer is connected to the detector. The detector is used to determine the presence of specific analytes in a sample including their kinetics and concentration (Liu et al., 2010a).

An affinity for the bio-sensitive recognition element or catalytic characteristics determine the selectivity and specificity of a biosensor. The interaction between the bio-sensitive recognition element and an analyte generates a signal which is transformed into an electrical or optical output by a transducer. The use of biosensors has a wide range of benefits including cost effectiveness, reliability, and accuracy. Biosensors are also easier to use compared to conventional laboratory detection devices due to their selectivity, high specificity, real-time response and reusability characteristics (Bange et al., 2005).

The integration of biosensor technology in microfluidics has transformed biosensing in the fields of environmental engineering, biological engineering, agricultural engineering, industrial monitoring, and point-of-care diagnostics.

The following Figure 5 shows the steps followed for analysis using biosensor technology.

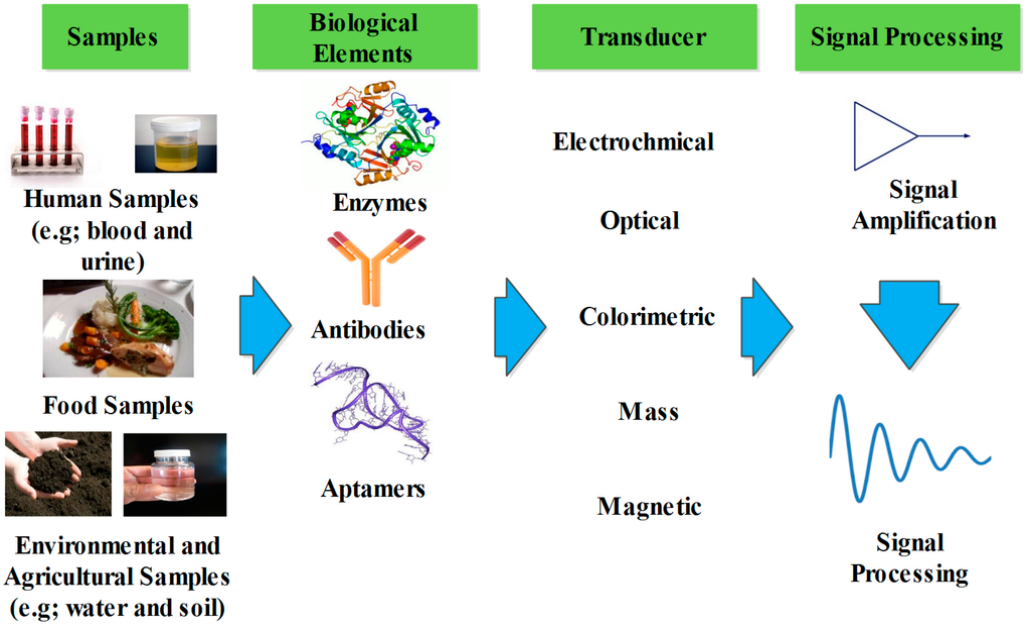

Figure 5. Representation of the components of a biosensor including transducers, detectors and bio-recognition elements (Luka et al., 2015)

2.3.2. Biosensors Categorization

Biosensors Categorization Based on Immobilization Techniques and Recognition Elements

A bio-sensitive recognition element enables a biosensor to respond to particular target analytes, and in turn, lower the chance of interference from undesirable substances. The selection of a bio-sensitive recognition element is based on the objective of the experiments, for instance, enzymes are selected for catalytic reactions while aptamers and antibodies are selected for pathogens or bacteria detection experiments (Koyun et al., 2012).

Different methods of bio-sensitive recognition element immobilization exist, for example, membrane confinement, covalent binding, entrapment, and adsorption. The most commonly used immobilization method is covalent bonding since it is irreversible and stable.

Enzyme-Based Biosensors and Antibody-Based Biosensors

Enzymes are proteins that are able to catalyse chemical reactions. Biosensor enzymes are used as catalysts for redox reactions. Monitoring biosensor enzyme turnover is conducted using a variety of electrochemical techniques making them ideal biosensors. Enzymes are highly selective to specific substrates which makes the use of them as a bio-sensitive recognition element very advantageous, and in addition to their ability to produce measurable parameters including protons, electrons, ions, heat and light (Yoo and Lee, 2010). Enzymes also present limitations, including limited thermostability, narrow substrate scope, and low or wrong stereo-and/or and/or regioselectivity (Reetz, 2016). Glucose oxidase-based biosensors, for instance, is an enzyme biosensor. Glucose oxidase biosensors involve oxidoreductase in the transfer of electrons from glucose to oxygen molecules. Immobilized glucose oxidase is used in the glucose biosensor to determine glucose concentration in body fluids (Rivet et al., 2011).

Antibody-based biosensors present a rapid detection biosensor system by using antibodies as the bio-sensitive recognition element. In the antibody-based biosensor system the analyte of interest (immunogen) does not require purification before detection (Byrne et al., 2009).

Aptamer-Based Biosensor

Aptamers are nucleic acid strands which have selectivity and affinity towards target analytes in the range of small molecules to whole cells. Aptamer isolation is conducted using the systematic evolution of ligands by exponential enrichment (SELEX) *in-vitro* selection method. Aptamers are isolated from large combinatorial libraries made up of close to 10^{15} different sequences. Additionally, aptamers can bind to specific ligands having dissociation constants in micromolar to picomolar range. Aptamer selection can be used for a wide variety of analytes, for example, proteins, pathogens, and toxins (Song et al., 2008). The aptamers offer benefits over antibodies such as: they are cheaper, have long-term stability, are able to react freely with their substrates even when immobilized onto solid supports, can also be separated easily from the reaction mixture, are able to control reaction times, and minimize the loss of bio-sensitive recognition in the reaction mixture (Lee et al., 2008).

Table 1 shows the advantages and limitations of each bio-sensitive recognition element: aptamer, antibody and enzyme (Cao et al., 2009).

Table 1. Examples of bio-sensitive recognition elements used in microfluidic devices (Luka et al., 2015).

Bio-sensitive Recognition Elements	Advantages	Limitations
Aptamers	• High sensitivity • Ability to detect a large number of analytes • Inexpensive, Rapid synthesis and long-term stability • Flexibility of use while preserving efficiency	• Usually forms weaker bonds with analytes • Excreted faster since they are small • More toxic than antibodies (Cao et al., 2009)
Antibodies	• Can be analysed rapidly using direct immunoassays • Effective for large target detection • Appropriate for bio-affinity interaction	• Costly and time consuming due to labelling requirement for indirect immunoassays • Not suitable for small target detection • Not suitable for redox reactions
Enzymes	• Suitable for redox reactions • High level of target selectivity • High level of sensitivity	• They are susceptible to activity loss once immobilized • Suitable for small analytes including urea, lactate and glucose

Biosensors Categorization Based on the Type of Transducers

There are different types of biosensors based on the applied type of transducer. The working of a transducer follows the transformation of the interaction between biomolecule and analyte into measurable electrical or optical signals. The type of physicochemical change in a reaction occurring at the generated sensing layer determines the choice of a biosensor's transducer component. The most common type of transducers used in biosensors are based

on the quartz crystal microbalance (QCM), using a liquid medium to give a direct response signal, which characterizes the binding event between a sensitive layer, placed onto the surface transducer, and the analyte to be detected (Bizet et al. 1999). The detection limit and sensitivity of a transducer depend on the bio-sensitive recognition (Korotkaya, 2014).

2.3.3. Microfluidics Integration with Biosensor Technology

The integration of biosensors with lab-on-chip technology has greatly improved the effectiveness of biosensor technology. This integration provides a miniaturized and integrated alternative to traditional laboratory methods that were repetitive in nature. Moreover, the integration of biosensors with lab-on-chip devices significantly reduces energy, reagent, and sample consumption during the experiments including a reduction in the amount of generated waste products. The reduced energy, reagent and sample consumption means that the cost of experiments are lowered and at the same time levels of detection sensitivity and specificity are increased relative to conventional methods of detection (Srinivasan et al., 2003).

The integration of a biosensor into a microfluidic device results into a microfluidic biosensor. A microfluidic biosensor is composed of numerous microsystems meaning that one biosensor is capable of performing a full analysis including treatment, sample separation, preconcentration and continuous sampling. Additionally, microfluidic biosensors manifest important characteristics including fast reaction rates, high throughput, and enhanced analytical performance. These characteristics make the microfluidic biosensors detection

adaptable to point of care uses. Microfluidic biosensors serve as powerful analytical tools that are also affordable (Luka et al., 2015).

Continuous Microfluidic-Based Biosensors

Continuous microfluidic-based biosensors enable continuous flow analysis in a microfluidic-based biosensor and reduce the complexity associated with the recycling of the biomolecules. Biomolecules such as nucleotides or oligonucleotides are provided in excess amounts to favour high reaction yield. Similarly, enzymes are used as catalysts in the reaction and are not consumed. In both cases the biomolecules are washed away after the experiment. These biomolecules can be recapture and recycling, and in consequence introduced to the same or a different sample (Zhao, 2016).

Enzyme-Based Continuous Microfluidic Biosensors

Enzyme-based biosensors operate on the integration of biosensor technology with microfluidic platforms. An example of an enzyme-based continuous microfluidic biosensor is one produced through bienzyme functionalized nanocomposite integration with the microfluidic biosensor (Ali et al., 2013).

Antibody-Based Continuous Microfluidic Biosensors

An example of an antibody-based continuous microfluidic biosensor was fabricated by Lee et al. (Lee et al., 2007b) in an experiment for breast cancer detection. They used surface plasmon resonance imaging (SPRi) where they installed temperature control units as the method is dependent on temperature. The temperature control unit consisted of micro-temperature sensors and heaters to maintain a constant temperature level. They immobilized anti-rabbit IgG on a gold surface using a regular self-assembled monolayer (SAM). The system of micropumps and microvalves ensured high accuracy, selectivity, and specificity in

the delivery of IgG solution. Additionally, the designed and fabricated microfluidic biosensor fabricated by Lee et al. proved to be a cost-effective method for detecting the presence of both protein-protein interaction and biomedical sample (Mairhofer et al., 2009).

Aptamer-Based Continuous Microfluidic Biosensors

Aptamers are biomolecules consisting of oligonucleotides made to bind a specific target molecule. Aptamers are usually created by selecting them from a large sequence of peptides. The comparison between aptamer and antibodies as bio-sensitive recognition elements shows aptamers present better qualities. This comparison shows that aptamer-based structures are easier to design and fabricate. Moreover, aptamer-based structures do require washing steps and secondary labelling for them to generate electrical or optical signals hence making their use in experiments to save time and money. An example of an aptamer-based continuous microfluidic biosensor was the one designed and fabricated by Zhou et al. (Zhou et al., 2014) in an experiment whose target was to detect living cells continuously. The microfluidic biosensor was fabricated on a glass substrate with two layers of PDMS and a gold electrode. The first PDMS layer had semi-circular microcups and microchannels while the second layer functioned as a pneumatic control unit. When cells' secretion was taking place the microcups were rising to speeded up the diffusion of protein towards the sensory area. Lowering the microcups facilitated cells' physical separation from the electrode's sensory area. The interaction between the specific aptamer and cell-secreted protein was confirmed using square wave voltammetry (SWV) measurements (Luka et al., 2015).

Droplet Microfluidic-Based Biosensor

The droplet microfluidic biosensors present three categories: enzymes-based, antibody-based and aptamer-based droplet microfluidic biosensors.

The enzyme-based droplet microfluidic biosensor was the one used, for example, by George Luka (Luka et al., 2015) for glucose detection using enzymes and a Platinum-black microelectrode. The electrochemical current variation (as a result of the β-D-glucose oxidation forming H_2O_2 as a byproduct) was measured using cyclic voltammetry (CV) and electrochemical impedance spectroscopy (EIS). Notably, this microfluidic biosensor was observed to be cost effective and of high sensitivity.

The antibody-based microfluidic biosensors have been used in the detection and capture of *E. coli* bacteria in drinking water quality control experiments. An example of the experiment that used this type of biosensor is the one conducted by Golberg (Golberg et al., 2014).

Digital Microfluidic-Based Biosensor

Biosensor integration with digital microfluidics has led to an improved performance of various fluidic operations, including mixing, separation, splitting, and transport. Digital microfluidic-based biosensors are also categorized in terms of the bio-recognition element used (Soper et al., 2006): The most common type of digital microfluidic system is glass based. The substrate layer, usually glass, of the device contains a patterned array of individually controllable electrodes. The substrate layer is the dielectric layer of the device used for building up charges and electrical field. The applied voltage activates the electrodes and allows changes through the device's surface in order to manipulate microdroplets (Wang et al., 2017). The advantages of DMF are portability, less sample consumption, shorter

chemical reaction time and flexibility. Nevertheless, the digital microfluidic technique presents an important disadvantage such us the need for piezoelectric substrate (Choi et al., 2012b).

Enzyme-Based Digital Microfluidic Biosensor

Srinivasan et al. studied different types of enzyme-based digital microfluidic-based biosensors, conducting experiments to determine the effectiveness of enzyme-based microfluidic biosensors using an optical absorbance measurement integration system with digital microfluidics for detection of metabolites found in the body (Srinivasan et al., 2003). The experiment used glucose oxidase as the bio-recognition element. Srinivasan and his colleagues also conducted another experiment with the same enzyme-based microfluidic biosensor which involved colorimetric enzyme-kinetic assay application for glucose detection in a droplet sample (Kumar et al., 2013).

Antibody-Based Digital Microfluidic Biosensor

Antibody-based digital microfluidic biosensors were tested by Choi et al. (Choi et al., 2012). Their digital microfluidic biosensor integrated the field effect transistor (FET) based biosensor into digital microfluidic technology where antibodies were used as the bio-recognition element in an experiment conducted to facilitate the detection of avian influenza antibodies (anti-AI). The device functioned on the basis of electrical current measurement. The electric current was from the FET biosensor. The analyte anti-AI droplets were delivered to the sensory area using the electrowetting-on-dielectric technique. The experimental results evidenced current reduction following the binding of specific anti-AI antibodies on the target antigen with a high detection limit. The developed digital microfluidic FET-based biosensor was a significant contribution to digital microfluidic biosensor technology development since

the detection and transportation of biomolecules was effectively conducted without the need of bulky transducers, pumps or microfluidic channels (Zaytseva et al., 2005).

Aptamer-Based Digital Microfluidic Biosensor

Application of aptamers in digital microfluidic biosensors uses antibodies as a complementary bio-recognition element. The functionality of the aptamer-based digital microfluidic biosensor was tested in an experiment involving the interaction between a droplet with fluorescence label immunoglobulin E (IgE) and another unlabelled IgE in the presence anti-IgE coated magnetic nanoparticles (Kratz et al., 2004).

2.3.4. Conclusion

Conventional methods of specific target detection and identification are time-consuming and costly. Additionally, conventional devices are not portable. Biosensor integration with microfluidic technology plays an important role in the replacement of bulky conventional devices due to their ability to combine biological and chemical components on one platform. Biosensors are important analytical tools in different fields of application including food safety assurance, security and defence, environmental and agricultural monitoring, and drug discovery. A biosensor selectivity and specificity depend on the bio-recognition element affinity. Microfluidic technology with integrated biosensor technology has increased the effectiveness of devices in laboratory experiments and in turn has reduced the energy consumption and reagent and analyte volume to reduce waste.

2.4 Separation using Anodized Nanomaterials

2.4.1. Introduction

Nanoporous materials can be engineered using electrochemical methods. The nanomaterials fabricated using this method includes nanoporous anodic aluminium oxide (AAO), titania nanotube arrays (TiNTs), and porous silicon (pSi). Nanoporous AAO, TiNTs, and pSi are some of the most preferred nanoporous materials utilized by researchers for biosensing and chemical substrates. These nanoporous materials can be integrated with optical techniques of particle separation such as reflective interference, Raman spectroscopy, optical waveguiding, plasmon resonance and surface acoustics. Nanoporous anodic alumina engineered through the anodization of aluminium has excellent mechanical, chemical and optical properties, for example, hardness, thermal stability, large specific surface area, chemical resistance, and biocompatibility. The high specific area to volume ratio of nanoporous AAO makes it suitable for use in the enhancement of optical signals in a case where analytes or target molecules are trapped inside the nanopores. This makes nanoporous AAO an outstanding platform for sophisticated applications including drug delivery, template synthesis, generation of energy and its storage, data storage, biological and chemical sensing, selective molecular separation, cell adhesion and culture, and catalysis. Nanoporous AAO substrates facilitate the fabrication of simple, smart, advanced and cost-effective tools of analysis. Nanoporous AAO geometry, surface chemistry, and pore sizes can be engineered hence making it a nanomaterial of high versatility due to the ability to tune its features in a manner facilitating the integration of sensing and separation capabilities into a single device. The AAO nanoporous surface chemistry, flexible structural modification, and optical

properties have facilitated its use in reflected interference and surface plasmon resonance-based systems (Mátéfi-Tempfli et al., 2008).

2.4.2. Nanoporous Anodic Aluminium Oxide Structure and Fabrication

The chemical and corrosion resistance of aluminium oxide has facilitated its use since the 1900s. The structure of nanoporous AAO is an alumina matrix with hexagonally-arranged and close-packed cells having a cylindrical pore at the center. After anodization is complete, any remaining aluminium can be selectively etched to give a free-standing nanoporous AAO substrate. Additionally, the capped pore aluminium oxide barrier layer can be etched to give a nanoporous AAO membrane. This leads to the formation of membranes with straight vertical nanochannels. Nanoporous AAO's fundamental parameters include pore length (L_p), the thickness of the oxide barrier (L_b), and pore diameter (D_p) including the inter-pore distance (D_{int}). Anodization conditions facilitate the control of L_p, L_b, D_p and D_{int} at a high level of precision, an example is given in Figure 6. The nanoporous AAO geometrical features are relatively versatile and can be controlled in the range of 50-600 nm for D_{int}, 10-400 nm for D_p and 30-250 nm for L_b. Other significant nanoporous AAO parameters are porosity (P) and pore density (δ_p).

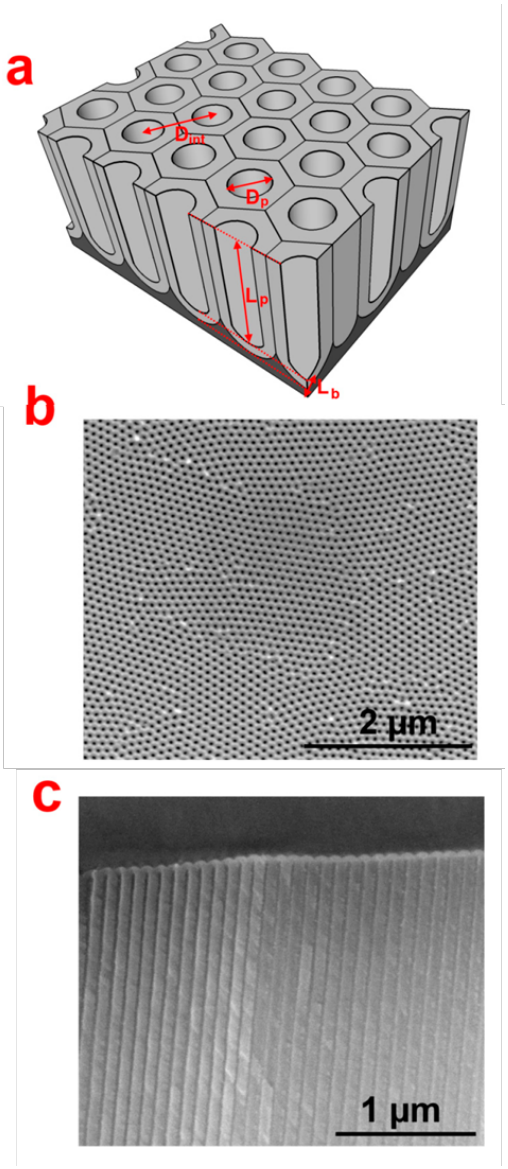

Figure 6. a. Nanoporous AAO structural characteristics pore length (Lp), the thickness of the oxide barrier (Lb), pore diameter (Dp) including the inter-pore distance (Dint) b. top view of an SEM image of a nanoporous AAO, c. cross-section view of an SEM of nanoporous AAO. (Kumeria et al., 2014)

Different anodization conditions lead to different nanoporous AAO structures. These conditions include the type of electrolyte, electrolyte concentration, temperature, and anodization voltage. The commonly used electrolytes in the fabrication of nanoporous AAO

include oxalic acid ($H_2C_2O_4$), phosphoric acid (H_3PO_4), and sulphuric acid (H_2SO_4). These electrolytes require different voltages to effectively generate the nanoporous AAO structure where the optimized voltage parameters for different electrolytes are: 40V for $H_2C_2O_4$, 195 V for H_3PO_4 and 25 V for H_2SO_4 (Schwirn et al., 2008). The process using $H_2C_2O_4$, H_3PO_4, and H_2SO_4 electrolytes is known as "mild" anodization due to moderate temperature and voltage requirement. However, aluminium anodization experiments conducted in other aqueous solutions including tartaric, malic, malonic, sulfamic and citric acids have also yielded positive results (Sulka, 2008). However, these acids achieve poor self-organization of nanoporous AAO pores in comparison to the level of success achieved with $H_2C_2O_4$, H_3PO_4, and H_2SO_4 acids.

An important step was made in the field of nanoporous AAO fabrication when Masuda and Fukuda used a two-step anodization technique to generate a highly self-organized nanoporous AAO successfully in 1995. This self-organized nanoporous AAO structure had high aspect ratios and narrow pore size distribution. The first anodization step involved the production of a porous aluminium oxide layer. The second step involved the selective removal of the porous aluminium oxide layer to facilitate pre-structuring of the aluminium surface. The pre-structuring of aluminium surface led to an improvement of the pore structural arrangement.

However, the mild anodization experiment conducted by Masuda and Fukuda had a limitation: a slow rate of pore growth (2–7 μm/h). Gösele and his colleagues solved this problem by introducing the 'hard' anodization process. The hard anodization introduced by Gösele and his colleagues used low temperature and high voltage conditions to achieve a high rate of pore growth (50–100 μm/h). The mild and hard anodization techniques of

nanoporous AAO fabrication were improved through integration with chemical etching. Moreover, techniques such as periodic anodization profiles were developed so as to fabricate complex pore geometries in nanoporous AAO (Lee et al., 2006). Electrochemical techniques to further manipulate and optimize the structure of nanoporous AAO were introduced which generated different pore morphologies including hierarchical and multi-structured pores and branched pores (Sulka, 2008). Other methods can also be applied in the fabrication of nanoporous AAO with complex structures including Ar plasma etching, electron-beam lithography, colloid sphere lithography (Yu and Zhang, 2013), direct laser writing lithography (Deubel et al., 2004), holographic lithography (Stankevičius et al., 2014) and focused-ion-beam lithography (Melngailis, 1993). These fabrication methods are selected based on the intended pore shape, size, and arrangement (Chu et al., 2005).

2.4.3. Nanoporous Anodic Alumina Properties, Surface Functionalization and Surface Chemistry

Nanoporous Anodic Alumina Properties

Nanoporous anodic alumina possesses various optical properties including absorbance, photoluminescence reflectivity, and transmittance. These optical properties make it a highly selective and sensitive particle separation tool. Nanoporous AAO also play an important role in the selection of target molecules including enzymes, DNA, antigens, and proteins. Nanoporous AAO devices can also be modified to enhance their chemical resistance, hydrophobicity, reflectivity, and anti-fouling properties (Law et al., 2016).

Surface Chemistry of Nanoporous Anodic Aluminium Oxide

Nanoporous AAO has layered surface chemistry characterized by a distribution of electrolytic impurities forming an onion-like structure. Nanoporous AAO's chemical structure is composed of inner and outer layers. The outer layer is located near the central pore while the inner layer is located far from the pore. The inner layer is made up of pure aluminium oxide while the outer layer is made up of contaminated aluminium oxide where the acid electrolyte is the impurity (Kumeria et al., 2014).

Nanoporous AAO is subject to chemical dissolution. The nanoporous AAO surface can be modified to protect it from chemical dissolution when placed in an acidic environment. The surface modification on nanoporous AAO includes gas-phase deposition and physical deposition techniques. The gas phase deposition techniques include chemical vapor deposition (CVD), plasma polymerization, atomic layer deposition (ALD), and thermal vapor deposition. Chemical modification methods include electrochemical and electroless deposition, sol-gel processing, layer-by-layer deposition, use of phosphoric and organic acids and silane self-assembly processes. The surface modification of nanoporous AAO can be used to attach biomolecules to nanoporous AAO pores and in the preparation of functional nanomaterials, for example, nanotubes, nanorods, and nanoparticles (Lee, 2010).

The techniques of surface functionalization include plasma polymerization, thermal vapor deposition, pulsed laser deposition and sputtering. They are used for the deposition of materials inside nanoporous AAO including carbon, nitrides, metals, and other metal oxides.

Metal coating can be carried out through sputtering, thermal vapor, and electron-beam deposition. Metal films deposited on nanoporous AAO using vapor deposition methods include nickel, palladium, silver, gold, titanium and platinum. These metal deposits are used

to improve nanoporous AAO substrates' chemical stability, reflectivity, and conductivity (Masuda and Satoh, 1996). The coating of nanoporous AAO is based on its catalytic properties. The metal coating process acts as a basis for further nanoporous AAO's chemical modification to facilitate biological and chemical species bonding for molecular separation and optical sensing operations. One main drawback associated with the use of deposition techniques is the limited penetration depth into the nanoporous AAO (Elam et al., 2003).

Nanoporous AAO can be platinum coated and used in charged proteins' separation. The thickness of a platinum layer can be increased to increase the efficiency of particle separation based size (Gong et al., 2001). The hexagonal arrangement of nanoporous AAO can be applied in the preparation of surface-enhanced Raman scattering (SERS) substrates (Chu et al., 2005).

Plasma polymer deposition is polymerization using plasma which can be applied in the deposition of biocompatible and reactive polymer films. The films have a controlled chemical functionality with aldehyde, carboxyl, epoxy, hydroxyl and amine groups (Yasuda and Wang, 1985).

Atomic layer deposition (ALD) facilitates accurate deposition of a wide range of materials including metal coatings, nitrides, oxides, and sulfides. The coatings generated depict high thermal, optical, chemical, and mechanical stability. These techniques can penetrate deep into nanopores enabling modification of nanoporous AAO's inner surface. Titania, silica, and alumina can be deposited controllably inside the pores of nanoporous AAO thus improving its transport, optical and catalytic properties and reducing its dimensions (Lillo and Losic, 2009).

Chemical vapor deposition (CVD) distributes dissociated gaseous molecules by plasma, light and heat to establish conformal and stable films on a substrate. It is possible to deposit carbon inside nanoporous AAO by CVD. This process facilitates the creation of vertically aligned carbon nanotube (CNT) arrays whose dimensions are controlled. The growth of CNTs inside the pores of nanoporous AAO occurs through the pyrolysis of a carbon source at temperatures above 600 ^{o}C. The carbon source used in pyrolysis can be gas, liquid or solid. Nanoporous AAO nanopores can also be modified using organosilane monolayers, for example, mercapto-silane (MPTES) to facilitate separation of mercury and gold in an aqueous sample (Park and Sudarshan, 2001).

Surface Modification of Nanoporous Anodic Alumina

Molecules can be bonded to the surface of nanoporous AAO to make sure the entire surface area is utilized. Notably, the presence of anionic impurities in the nanoporous AAO structure exposes it to oxide attack leading to the production of surface hydroxyl groups (Lee et al., 2004). Wet chemical surface modification techniques of nanoporous AAO are beneficial since the phenomenon of self-assembly can be applied. The self-assembly phenomenon establishes a monolayer coating across the pores' surface. Argosilanes, phosphonic acids, and carboxylic acids can be used for the generation of selective surface chemistry on the surface of nanoporous AAO and are used to form uniform monolayers on the surface (Michalak et al., 2010).

The self-assembled monolayers (SAMs) are assembled using organic molecules. These organic molecules are generated when molecules are attached and arranged spontaneously. SAMs can be assembled using different methods.

The nanoporous AAO organosilanization helps to control adsorption and wettability characteristics. There is a wide range of commercial organosilanes. These organosilanes can be bound covalently to the surface of nanoporous AAO through the incubation of the hydroxylated nanoporous AAO substrate. Hydrophobic terminal groups, for example, perfluoroalkyl-silanes and alkyl-trichloro-silanes can be used in SAMs selective production. The selective production of SAMs can be used to demonstrate how the wettability of nanoporous AAO surface can be tuned. Alkyl-trichlorosilanes having chain lengths C1-C8 can be used to make nanoporous AAO hydrophobic. The hydrophilicity of nanoporous AAO can also be increased using silanes having active functional groups, for example, epoxy-terminated silanes, amine-terminated silanes, and PEG-silanes (Brevnov et al., 2004).

Functionalization using Phosphoric and Organic Acids

Organic acids such as 2,3,4,5,6-pentafluorobenzoic acid, trifluoroacetic acid, octadecanoic acid and perfluoropentanoic acid induce hydrophobicity to the surface of nanoporous AAO. However, the monolayers formed by the organic acids on the surface of nanoporous AAO depict instability when subjected to aqueous environments. On the other hand, the monolayers generated on the surface of nanoporous AAO using phosphoric acids are stable in aqueous environments.

2.4.4. Separation

Nanoporous structures, most importantly, nanoporous AAO has been applied in many separation experiments. The suitability of nanoporous AAO for use in separation experiments is because the pores are uniform and narrow. Additionally, the membrane of nanoporous AAO has high flux rate and selectivity. Nanoporous AAO has mostly played a significant

role in biomolecule separation. Nanoporous AAO membranes are straight, aligned, uniform, mechanically stable and biologically stable hence facilitating the separation of biomolecules. This process of separation is applied in biofiltration experiments. The applicability of biofiltration techniques is based on chemical affiliation and size limitation (Osmanbeyoglu et al., 2009).

The biofiltration mechanism works through size limitation. This mechanism facilitates the separation of different sizes of biomolecules. Notably, the AAO nanopores allow biomolecules of a smaller size to pass through them and prevent those with a bigger size from passing through.

Chemical Mechanism of Biofiltration

The chemical mechanism of biofiltration operates based on the nanoporous AAO membranes tendency to bond with biomolecules selectively. The selective bonding of biomolecules with the surface of nanoporous AAO makes the molecules that are more attracted to the nanoporous AAO travel at a lower velocity in relation to those that are not attracted to the surface.

Lee et al. conducted an experiment to investigate water, nitrogen and ovalbumin molecules transportation on nanoporous AAO. The first step in this experiment involved the physical attachment of polyethyleneimine (PEI) on the surface of nanoporous AAO. The second step involved grafting a polyethyleneglycol (PEG) chain using the polyethyleneimine nanoporous anodic alumina (PEI-NAA) sample. Use of PEG to modify the PEI-NAA sample resulted in a reduction in the rate of molecule transportation as a result of reduced permeability of the membrane. PEG possesses a hydrophilic and neutral chemical structure

which coupled with its brush-like chains lead to the repulsion of selected molecules, for example, proteins (Lee et al., 2005).

Another experiment conducted to investigate the separation and transport properties of biomolecules in nanoporous AAO was the protein adsorption test (FITC-BSA). This experiment capitalized on the fact that nanoporous AAO samples modified with PEG had a lower protein adsorption compared to the unmodified ones. This modification ensured that the protein adsorption purely depended on the protein-AAO nanoporous surface interaction and not by trapping proteins inside the AAO pores (Chen et al., 2008).

The above experiments indicate that the AAO pores have the ability to change the fluid transportation rate, for example, water and nitrogen. Additionally, AAO pore size can be minimized to molecular dimensions through different methods. The reduction facilitates the selective separation of biomolecules based on their difference in size.

2.4.5. Conclusion

The properties of nanoporous AAO have been utilized for various applications in the fields of electrochemistry, nanotechnology, medicine, cell biology, and optics. Different methods of nanoporous AAO structure fabrication have facilitated the control over porosity, pore diameter, pore organization, and length. Notably, the nanoporous AAO structure can be modified further for various uses. The modification of the nanoporous AAO surface has played an important role in particle separation. This is due to the ability to adjust the size of nanopores and/or change the chemical characteristics of the nanoporous AAO surface. The

ability to modify nanoporous AAO has enabled and led to high specificity, efficiency, and selectivity levels.

3. Materials and Methods

3.1 Lab-on-a-chip device fabrication

3.1.1. Fabrication of microhills by wet chemical etching

Microhills were fabricated in order to create the imprint pattern needed to fabricate the microchannels. Etching was used to fabricate the microhills on the wafer. Etching is the method used in micro/nanofabrication to chemically remove layers from a wafer surface. A glass microscopy slide was utilized as the wafer in this work. Silicate glass is commonly used due to their unique properties. Silicate glass is able to resist harsh environmental conditions and they are also optically transparent. Silica glass can also be engineered into a specific shape with relative ease as a result of their unique temperature-viscosity relationship (Steingoetter and Fouckhardt, 2005). Silicate glass also has strong resistance to most liquids and gases. Silicate glass is soluble in hydrofluoric acid (HF) or other aqueous solutions containing HF. HF^- based etchants, under a controlled environment, can be used to remove materials from glass surfaces for various purposes and uses.

In the etching procedure, part of the wafer was protected from the etchant with a mask. This mask was deposited and patterned on the wafer in a prior fabrication step using lithography. This method was used to make the desired design on the wafer. The protection mask is a photoresist material, which after development, exposes the desired area of the wafer to be etched. To make the desired design on the glass a chrome mask is placed on top of the wafer, which is covered with the photoresist and placed under ultraviolet (UV) light. The chrome metal, which forms the protection mask under UV-light, was chosen due to its ability

to absorb UV light, which minimizes the reflection of specific wavelengths. The photomask (chrome protection mask) is a flat piece of quartz with a layer of chrome on one side, containing a nano, micro or macro image suitable for nano/micro device imprinting. The use of a photomask under UV light to imprint a desired design is known as photolithography. The development step removes the photoresist from the glass areas that have been exposed to the etchant. The photolithographic procedure, which is explained in detail subsequently, is shown schematically in Figure 7.

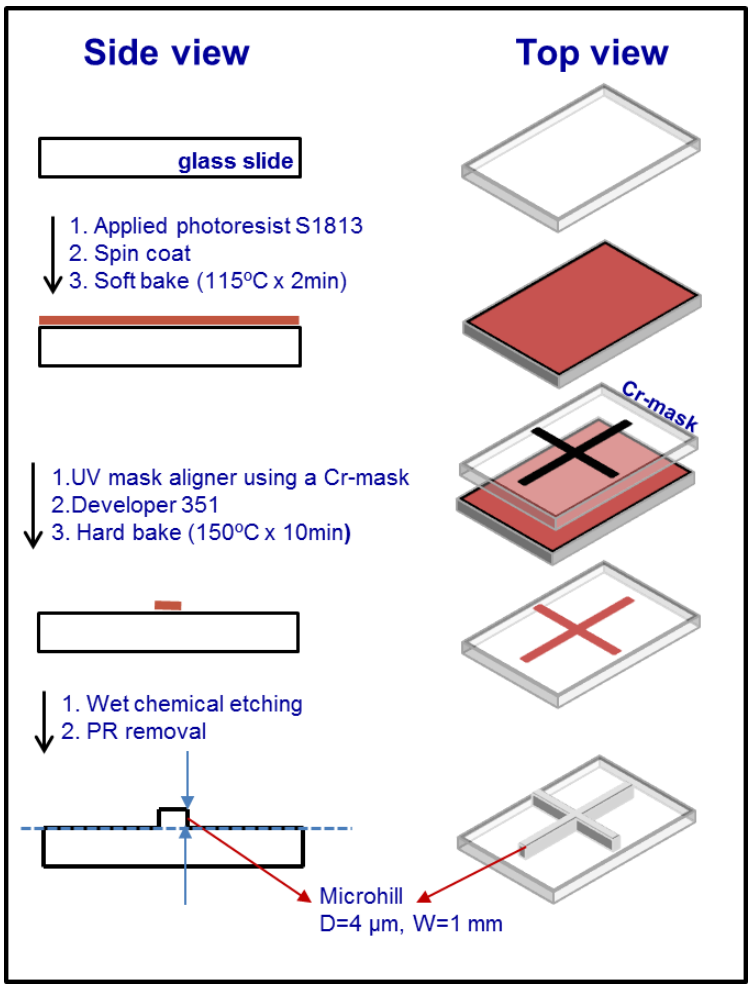

Figure 7. The fabrication procedure to make microhills on a glass surface. In this case the depth of the microhill was 4 µm and width 1 mm. PR is the acronym of photoresist.

When the photolithographic procedure is complete, the exposed wafer is attacked by a liquid etchant. The etchant removes layers from the wafer either by isotropic etching which means layers are etched uniformly in all directions or by anisotropic etching, whereby the surface is etched preferentially in one direction (Figure 8). In order to choose the appropriate etching method, a suitable chemical substance must be selected for use.

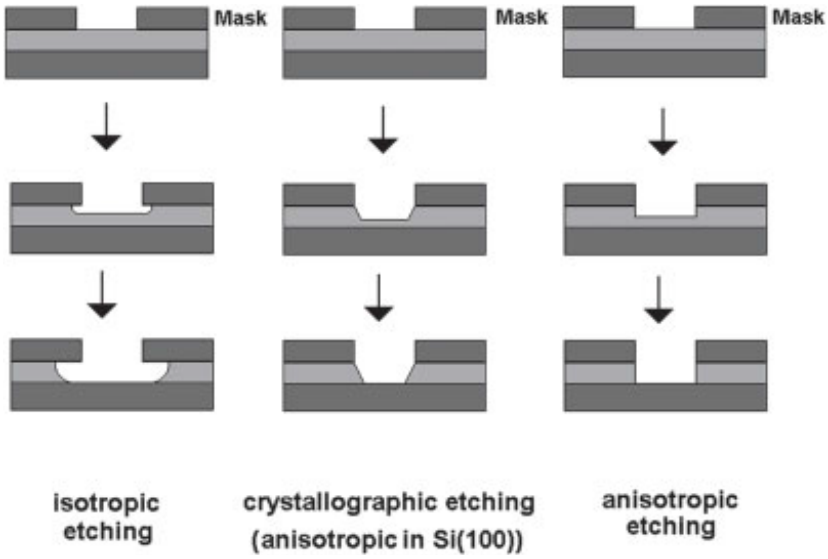

Figure 8. Different etched geometries after isotropic and anisotropic etching. (Köhler and Fritzsche, 2007)

The etching method used in this work is known as anisotropic wet chemical etching. The etchant used was a mix of silicon dioxide etchant 20:1, 20 mL (which contains hydrofluoric acid and ammonium chloride) and concentrated hydrochloric acid (HCl), 1 mL. Wet chemical etching is a hazardous chemical procedure due to the use of HF which is a highly corrosive acid which can dissolve many materials and can cause permanent damage to human

tissue, resulting in tissue death. For this reason, wet chemical etching was only used once in this work in order to fabricate the microhill pattern on the glass slide surface. This sample was then used for subsequent imprinting to make microchannels. Dissolving HF in water forms a weak acid containing F^-, HF^{2-}, H^+ ions including HF molecules that have not yet undergone dissociation. The concentration (K_1 and K_2) of the dissolved HF can be defined using two equations including:

$$K_1 = [HF]\,[F^-]/[HF^{2-}] \quad \textbf{[3]}$$

$$K_2 = [H^+]\,[F^-]/[HF] \quad \textbf{[4]}$$

where K_1 and K_2 are the concentrations of the dissolved hydrofluoric acid, [HF] the concentration of the hydrofluoric acid, $[F^{=}]$ the concentration of the fluorine and $[H^+]$ is the concertation of hydrogen.

The presence of F^-, HF^{2-}, H^+ ions governs the rate at which a HF aqueous solution attacks the glass. The etching process of glass by the HF aqueous solution is kinetically controlled. The reactive species chemisorption, adsorption, and the effect of these processes on siloxane bonds at the surface of glass is what controls the process of dissolution. The adsorption processes of F^-, HF^{2-}, H^+ ions; HF molecules determine the etching rate of glass. The H^+ ions catalyse the etching process through the destruction of siloxane bonds (Menapace et al., 2002).

The microhills fabrication procedure consists of the following steps. Firstly, a photoresist S1813 (company TM G2) is applied to the surface of a glass microscope slide (fisher brand) by spin coating, to give a homogeneous photoresist layer, followed by a two minute post exposure soft bake on a hot plate at 115 °C. Spin coating enables the photoresist solution to

be deposited uniformly onto the glass surface. The wafer is held on a spinner chuck by vacuum and the resist solution coats the glass to uniform thickness by centrifugal spinning (the spin coater was: Headway Research INC, model PWM 32, and the resist spinner was controlled by the controller Headway Research INC, model 1-PWN 101- CB 15). The spin coating parameters for the photoresist S1813 were 3000 rpm for 12 seconds.

Each photoresist gives a certain thickness after being applied onto the sample surface. The thickness of the photoresist can be identified from the name of the photoresist, i.e. S1813 is 1.3 μm, the last two digits of the number states the thickness to be obtained. Thickness is also calculated using an empirical equation (Geschke et al., 2004):

$$t_{coating} \approx \frac{K\nu}{\sqrt{\omega}} \quad \textbf{[5]}$$

where $t_{coating}$ is the thickness of the coating, K is a proportionality spinner constant, typically 80-100, ν is the kinematic viscosity ($mm^2\ s^{-1}$) and ω is the number of revolutions per minute, followed by a two-minute post-exposure soft bake on a hot plate at 115 °C. Heating the photoresist makes it hard and durable for UV exposure step. The whole nanofabrication procedure took place in a cleanroom (see more details in Appendix 8.2.).

There are two different types of photoresist: positive and negative. The positive photoresist breaks chemical bonds in the material when exposed to UV-light, so that the exposed region dissolves in the developer and the unexposed (protected by Cr-mask) region remains. The negative photoresist strengthens the chemical bonds in the material when exposed to UV-light and the exposed regions remain intact and the unexposed regions dissolve in the developer. It should be noted that positive photoresists are more common and

have better precision, because they are able to imprint structures down to nanometer resolution. The S1813 photoresist used in this work was a positive photoresist.

A chrome metal mask was placed on top of the photoresist layer and fixed in position. Both were then placed into the contact mask aligner (KMS Karl Suss mask aligner, model MJB3) and exposed to UV-light for 30 seconds. The closer the mask is placed to the photoresist layers, the better result. For this reason, the chrome metal layer is placed on the photoresist in order to attach to each other. Figure 9 (a) shows the chrome layer touching the photoresist. In this conformation, the error (pathway of UV light) is much lower than in Figure 9 (b) where the supporting chrome glass is attached to the photoresist layer. The UV mask aligner is a high precision microscope with a light source which releases a wavelength capable to transfer the image of the photomask to the wafer.

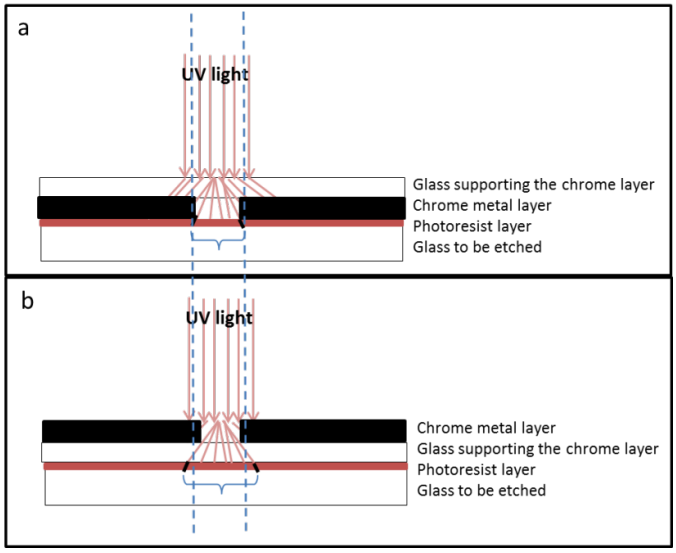

Figure 9. a) UV rays attack the photoresist layer giving a minimum error of a couple of nanometres, instead in b) the beam of rays attacks a much wider surface area.

The area exposed to UV-light changes the chemical properties of the photoresist and allows it to be removed from the developer. The chrome mask was designed with AutoCAD and made by Compugraphics Photomask Solutions Company with standard dimensions and using a standardized pattern of the effective exposure area where the UV light can attack the photoresist (see Figure 10).

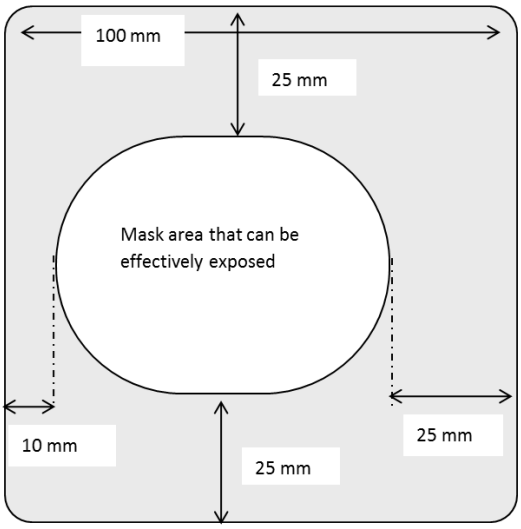

Figure 10. Standard dimensions of the photomask and exposure area that can be effectively uncovered and attacked by UV light.

After pre-baking and UV exposure, the sample was immediately immersed in a developer (Microposit 351 developer, Shilpley Company) for 30 seconds, a solution which also contains sodium hydroxide (NaOH). The UV treated photoresist was removed by the developer and the imprinted pattern was now visible. The sample was immersed in the developer for 5 minutes leaving the glass surface exposed to be treated with the etchant. The etchant attacks the non-protected and clean glass surface, while the sections, which were not

exposed to UV light, are still covered by the photoresist and protected from the etchant. A hard bake was carried out at this stage for 10 min at 150 °C on a hot plate in order to solidify the remaining photoresist and make the protective layer more durable for the next wet chemical etching step. After this process the sample is ready for wet chemical anisotropic etching.

The time spent immersed in the etchant bath determines the depth of the resulting etch. The etching time is calculated from the equation (Köhler and Fritzsche, 2007):

$$\boldsymbol{r_{etch} = d_{etch}/t_{etch}} \qquad [6]$$

where r_{etch} is the rate of etching, d_{etch} is the removed thickness and t_{etch} is the total immersion time. The mass of the material removed m_{etch} (Köhler and Fritzsche, 2007) can be calculated, using equation [6], from the layer to be etched depends on the etched area, *A* and the density, ρ of the material:

$$\boldsymbol{m_{etch} = m_{etch} \cdot t_{etch} \cdot A \cdot \rho} \qquad [7]$$

The etching rate depends on a number of factors including the concentration and composition of the etchant, the material to be etched and accuracy and temperature conditions. Due to the inconsistent nature of etching, the rate is often determined experimentally and optimized prior to the etching process. In this case the sample was immersed in the etchant bath using a plastic Azlon beaker suitable for hydrofluoric acid, for 10 min under very slow agitation, using a magnetic stir plate (IKA-VIBRAX_VXR), to avoid any spillage and under a special fume hood for HF work. All the work was carried out using

special gloves for HF (Marigold Industrial Feather Weight PLUS G31H), an apron covering the body and a face mask covering the face.

Once the etching process was complete, the sample was removed from the chemical bath and washed thoroughly with water. The photoresist removal step then followed. It was easily removed with acetone and the sample was ready for further analysis and characterization.

3.1.2. Surface profile measurement of the microhill

The sample quality was first observed under an optical microscope to confirm that the pattern was successful and ready for further characterization. Then, the geometric dimensions of the microhill (width, height, and roughness) were characterized using a stylus profilometer (Dektak 6M, Figure 11a). The profilometer consists of a sensitive stylus, which can scroll linearly on the sample surface and measure the profile's width, height and roughness. A pre-inserted weight is applied to the stylus. A setting of 2 mg was applied to the stylus in order to carry out the measurement.

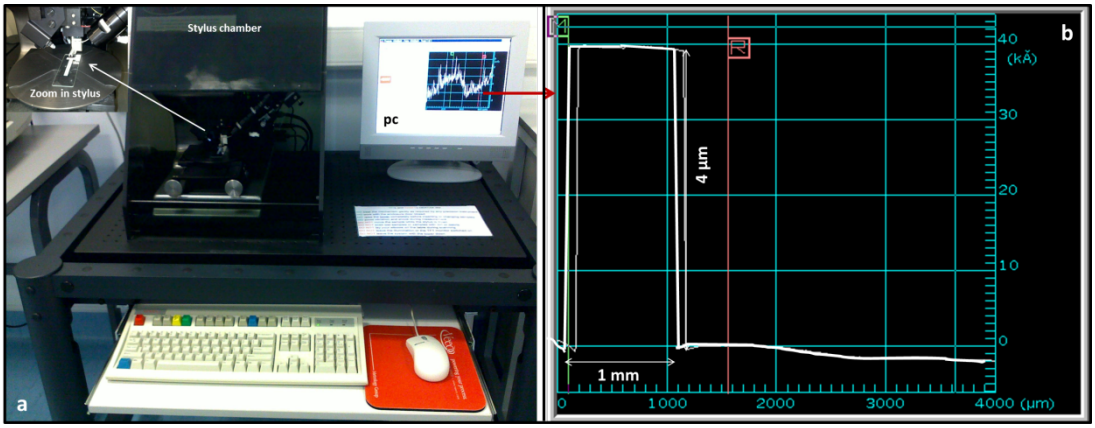

Figure 11. a) Stylus profilometer. b) The graph of the microhill profile with dimensions of the microhill; 1 mm width and 4 µm height

Figure 11b presents the height and width profiles of the microhill, which are 4 µm and 1 mm respectively. The roughness of the walls which are completely straight is also presented. The top of the hill is also straight with a small tilting of 1 nm in the middle. On the right and left-hand side of the microhill, the walls (shown by the surface line) appear not perfectly aligned. In fact, this is an artefact due to a calibration error of the profilometer. At this stage the negative imprint is ready to be used to produce the positive of the proposed design.

3.1.3. Fabrication of microchannels using poly-dimethyl-siloxane

An elastic polymeric material was used to make the microchannels, which after curing can be peeled off from the pattern giving an exact positive image of the microhill pattern. This material is an organosilicone compound, known as poly-dimethyl-siloxane (PDMS). PDMS in an elastomeric silicon based organic polymer with particular rheological properties. It is able to imprint all types of structures in great detail, down to the nanoscale. PDMS

consists of two liquid components: A curing agent and a base. Before mixing, the substances are both in the liquid phase; once mixed they become a flexible solid elastomer after a few hours, baked or not. If the PDMS is baked the final resulting material is more rigid and less sticky; on the other hand, if the mixture is left to solidify at room temperature the material will still become solid but will be more elastic and sticky. The PDMS used in this work was Sylgard 184 (Dow Corning Company). The mixing ratio of the curing agent and base was 1:10 respectively. The procedure to make the microchannels with PDMS follows.

As part of the preparation of PDMS, disposable plastic cups, gloves, and a plastic knife were used. The cup was placed on an electronic scale and 1:10 of the curing agent and base monomers, respectively, were weighed. Subsequently, the mixture was stirred with the knife for 3 minutes, which formed numerous air bubbles (Figure 12a). The mixture was therefore degassed in a desiccator under vacuum for approximately 1 hour (Figure 12b).

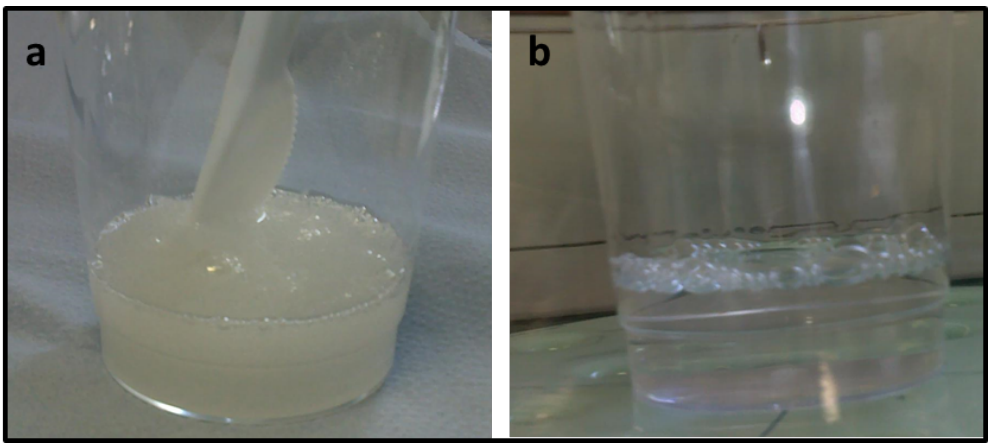

Figure 12. Working with PDMS: a) the liquid mixture after stirring in air with visible air bubbles; b) after one hour under vacuum air bubbles are removed and the mixture became transparent.

Once the PDMS became a transparent liquid it was poured onto the glass slide surface (with the microhills) and cured at 80 °C for 15 minutes (or 90 °C for 10 minutes). After 15 minutes the PDMS exhibits elastic solid behaviour and can be peeled off from the pattern.

At this stage the PDMS is ready to use as a sample substrate and ready to be sealed in a subsequent step. Metal deposition is the intermediate step before sealing the device. This step is critical because it determines the use of the device.

3.1.4. Physical vapor metal deposition on the wafer

Physical vapour metal deposition is the method for depositing thin films with controlled thicknesses by evaporation of a metal to a solid surface under vacuum. The metal deposition takes place under vacuum and allows vapor particles to travel directly to a target substrate where they condense back to a solid state. For the metal evaporation, Edwards Thermal Evaporator FL 400 and Edwards Electron Beam Evaporator Auto 306 (as acronym is used e-beam, it can be seen in Figure 13) were used depending on the desired metal deposited thickness.

The deposited metal was placed in a tungsten boat. The tungsten boat was connected with two electrodes and current was applied across the boat. A suitable current for each metal was passed through the boat to melt and evaporate the metal. A slow deposition rate is used in order to deposit a smooth metal layer. Current and deposition rate values are positively correlated so if a high current is applied across the boat, the deposition rate for the metal deposition increases. A high current may cause bursts and sparks giving a rough indeterminate metal layer. In addition, if the substrate used is not resistant to heat, such as

PDMS, it can be degraded. The vacuum plays an important role for the smoothness of the deposited surface.

Figure 13. The electron beam evaporator on the right-hand side and its power supply on the left hand side.

The vacuum in the deposition chamber should be at least 10^{-6} mbar, in order to leave a free path for the evaporated particles to travel directly to the target without colliding with the background gas. The same applies for the e-beam evaporator to allow the free path of electrons from the electron gun to the metal in the crucible and from the crucible to the wafer substrate. In both cases the deposition chamber was evacuated under pressure of at least 3.6 x 10^{-6} mbar.

If the vacuum is lower than 10^{-6}, evaporated metal particles collide with vapor atoms in the chamber and react with them, which may change their chemical composition. These atoms reach the substrate and make it non-uniform. The reason the aluminium has the oval

porous appearance (Figure 14) is because the atoms of aluminium collide with vapor atoms inside the chamber and the resulting deposited layer is alumina instead of aluminium. In addition, it is easy for this to happen when aluminium is in use, because when aluminium starts melting with any equipment, thermal or e-beam evaporator, it outgases and disturbs the high vacuum in the chamber. Figure 14 shows the aluminium layer after aluminium metal deposition in an insufficient vacuum, 10^{-5} mbar. An alumina layer is clearly observed instead of aluminium. The aluminium metal collides with the vapor atoms and becomes oxidized which results in an alumina layer.

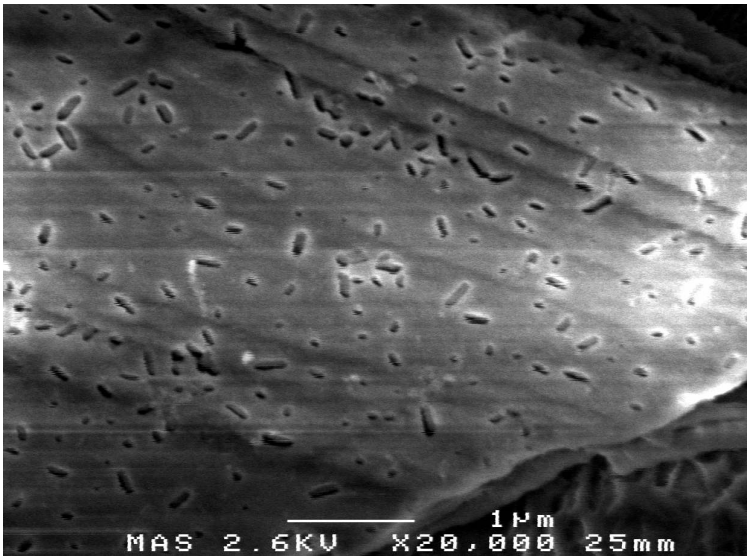

Figure 14. Oval shaped nanopores, due to insufficient vacuum in the chamber during metal deposition.

The e-beam evaporator was used to make a thick Al layer, up to 1 µm, as opposed to the thermal evaporation which can achieve a thickness up to 300 nm. In addition, the choice of the suitable evaporator, e-beam or thermal, depends on the metal. E-beam evaporators use

crucibles which need at least 1 g of metal in order to give up to 1 μm thickness. On the other hand, thermal evaporators use tungsten boats and need a few milligrams of the metal to give the suitable thickness. If the metal is expensive, like gold, platinum or silver, the e-beam evaporator is not suitable as the amount of material necessary would not be cost effective. Therefore, the thermal evaporation method is far more cost effective.

The metal deposition was carried out on two different surfaces. Initially the metal was deposited on PDMS inside the microchannel (Figure 15) and the second approach deposited the metal directly onto a thoroughly clean glass slide (Figure 16). In the first case, PDMS was appropriately cleaned with sellotape, which is an effective method for removing any dust attached onto the PDMS surface. Any glue in contact with PDMS loses its stickiness properties (except glues containing silicon) and they remain liquid for long time (i.e. the glue does not set). However, metal deposition onto PDMS did not yield consistent results. Consequently, the method was changed to depositing the metal onto a glass surface and using the PDMS etched channel to seal the glass.

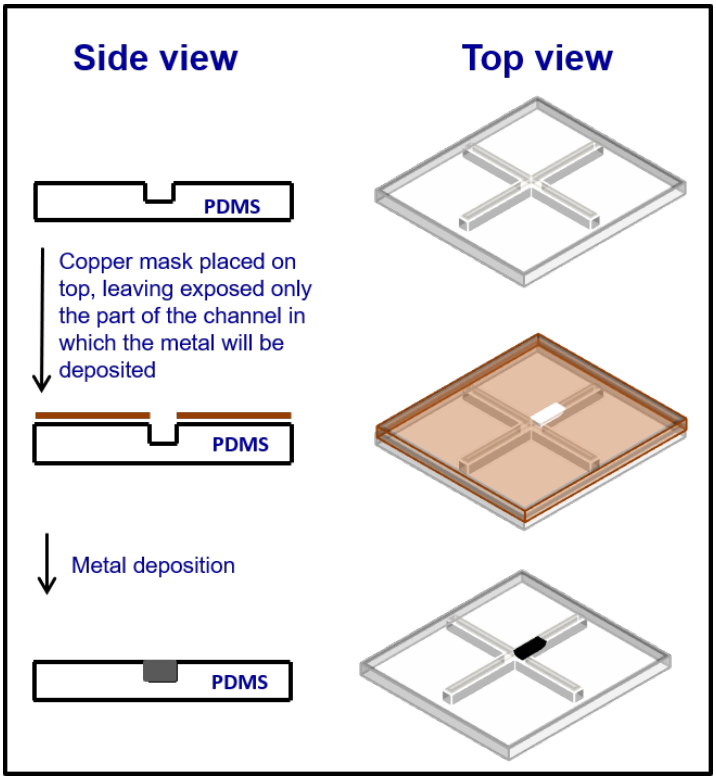

Figure 15. Metal deposition inside the glass microchannel using a copper mask in order to protect the sample and leave exposed only the part where the metal should be deposited.

A copper shadow mask was made with exactly the same width of the microchannel. To deposit the metal in the correct position on a glass surface the same copper shadow mask as the PDMS was used, as it already possesses the correct dimensions of the microchannel. The copper shadow mask was aligned on top of the PDMS microchannel under a Leica stereo microscope (MZ6 with photonic controller CL5 100 x). Kapton tape was used to stabilize the mask on top of the glass to keep them together as it is resistant to the high temperatures occurring inside the evaporator chamber and does not leave traces after peeling it off.

Prior to metal deposition the glass was thoroughly washed as follows: First piranha solution, consisting of 98% sulphuric acid (H_2SO_4) and 30% hydrogen peroxide (H_2O_2) in

ratio (2-4) : (1) respectively (the H_2SO_4 can be used in quantities 2 to 4 depending on the effectiveness needed). Once the two solutions H_2SO_4 and H_2O_2 are mixed together the temperature of the mixture rises to 80 °C. The solution should always be fresh as after an hour the H_2O_2 evaporates and the temperature decreases to room temperature. The piranha solution does not affect the metal layer, so it could also be used for cleaning the substrate after metal deposition.

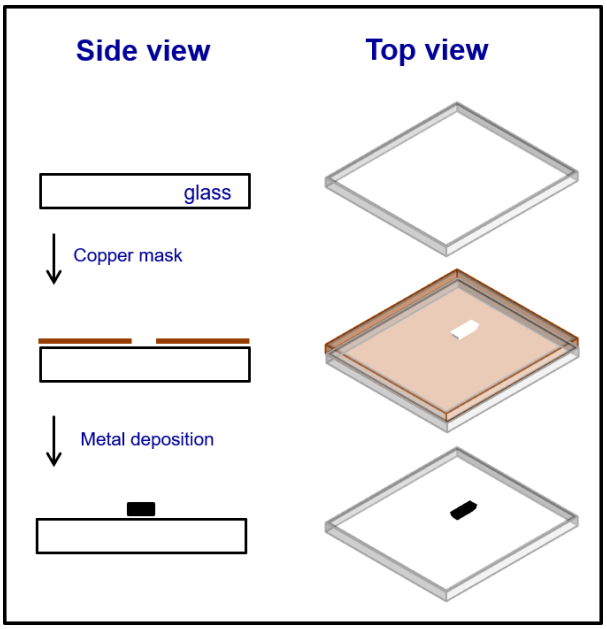

Figure 16. The metal deposition method on a glass surface using a copper shadow mask in order to obtain the deposition in the determined area of the sample with predetermined design.

After thorough cleaning of the glass substrate, the mask must be cleaned. This was carried out in a water bath under sonication for 2 minutes. All glass slides and masks, after thorough cleaning, were placed in the oven at 90 °C to dry out (for at least 5 minutes). Resulting in a smooth layer of metal on the glass surface with no cracks or gaps. The metals or chemical

compounds deposited on the glass surface using these techniques were aluminium (Al), gold (Au), titanium (Ti), chromium (Cr), zinc (Zn) and silicon dioxide (SiO_2). Each metal deposited was used for a different application.

3.1.5. PDMS and glass surface exposure to oxygen plasma

The metal layer was deposited on a clean glass slide and the PDMS was prepared with the microchannels. The device was now ready to be sealed by sticking the two parts together to make a permanent bond. Different methods were attempted but only one gave a strong and consistent bond. Glue was used for the first method; this failed as the glue on the PDMS surface lost its stickiness (the glue does not set), making the bond with the glass impossible. A second way, which also did not work, was to seal the two parts by making them both hydrophilic using a primer or other substances to improve surface hydrophilicity. The third method was to expose both surfaces to ozone (O_3) under UV light, which enriched both surfaces with more oxygen atoms, but again it did not give a permanent bond to the whole surface area – there was only partial bonding. The ozone and UV-light affected the two surfaces, but the result was partially successful with sporadic bonding of the two surfaces. They were not enriched homogeneously enough with oxygen. Different oxygen plasma generators, including an ICP, a RF plasma barrel etcher (PT 7300) were tested but all produced only partial bonding between the two surfaces due to different reasons.

Finally, a Zepto Oxygen Plasma machine, (Figure 17), consisting of a metal cylindrical sealed chamber in which two metal electrodes at a fixed distance are placed in a reactor, was successful. One electrode was connected to a power supply and the other one is grounded.

This system makes a capacitive coupled plasma by applying a single radio-frequency (RF) power.

Figure 17. Zepto plasma equipment.

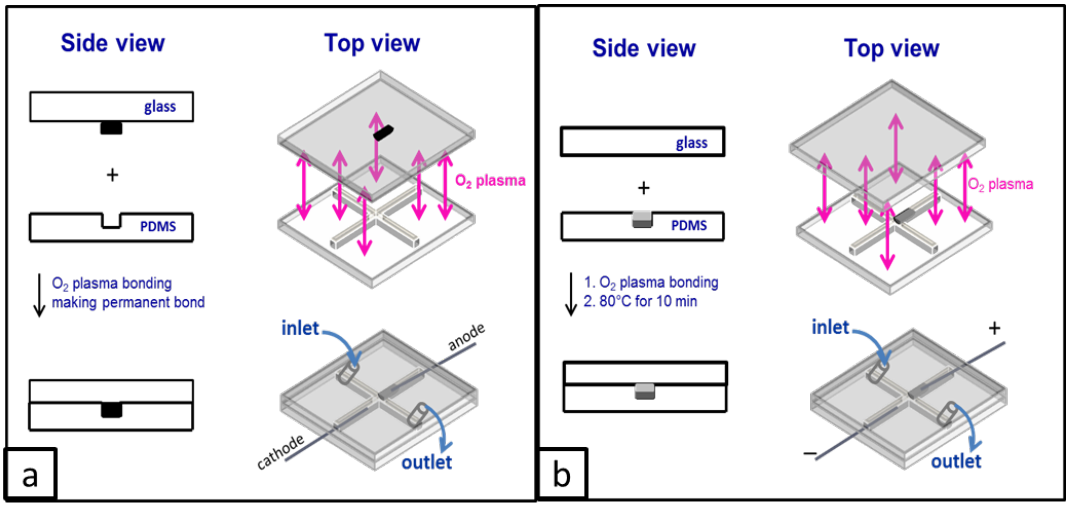

Figure 18. Schematics to show the oxygen plasma bonding process with a) the metal deposited on the glass surface and b) on PDMS.

To ensure that oxygen was flowing in the plasma chamber a colour characterization method was used (Table 2). With this method it is also possible to know whether the oxygen has been contaminated with air or other substances possibly existing within the chamber.

Table 2. Colour characterization of plasma purity and oxygen flow purity inside the oxygen plasma equipment., depending of the vacuum and time of the flow.

Parameters		**Plasma colour**	**Oxygen flowing**
Vacuum (mbar)	High (10^{-6})	light sky blue	Grey (highly pure)
	Medium (10^{-4})	blue	Purple (pure, but nitrogen contaminated)
	Low (10^{-2})	dark blue	Pink (air contaminated)
Flow time (sec)		A darkening of the plasma is observed when the plasma chamber is not left to pump down to a low pressure.	When the oxygen starts flowing each characteristic colour gives the feedback of the purity of the chamber. This is based on the different wavelength of light that each gas emits. The combination of two gases can explain the colour in the chamber.

Once both surfaces, PDMS and glass, were thoroughly cleaned using the method explained above, they were both exposed to oxygen plasma by placing them in a chamber with a plasma power 25 W, oxygen flow 25 sccm for 25-30 seconds. The chemical behaviour of the PDMS surface after oxygen plasma treatment can be seen in Figure 19.

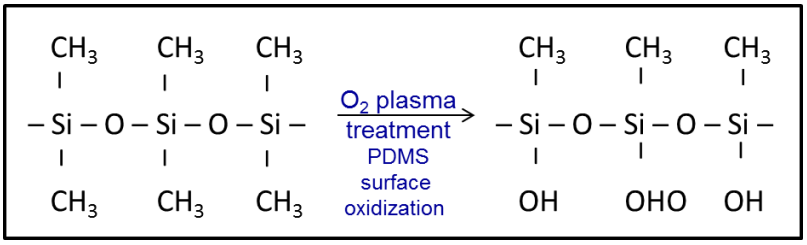

Figure 19. The poly-dimethyl siloxane (PDMS) chemical formula in which the outer methyl groups changes to hydroxyl groups after oxygen plasma exposure known as surface oxidization.

The outer methyl groups were changed to hydroxyl groups after exposure to oxygen plasma and the superhydrophobic behaviour of the PDMS surface changed to superhyrdophilic. This result is stable for a couple of hours; after this time, contact with air returns the PDMS to its initial superhydrophobic chemical behaviour. To prolong the hydrophilic state, the PDMS sample has to be immersed in water (Ma et al., 2011). Once both substrates were removed from the plasma chamber they were brought into immediate contact. The sample was now complete and placed in the oven for 10 minutes at 70-80 °C to harden the bond and make it permanent. The chemical formula of the permanent bond between PDMS and glass surfaces under heating treatment can be seen in Figure 20.

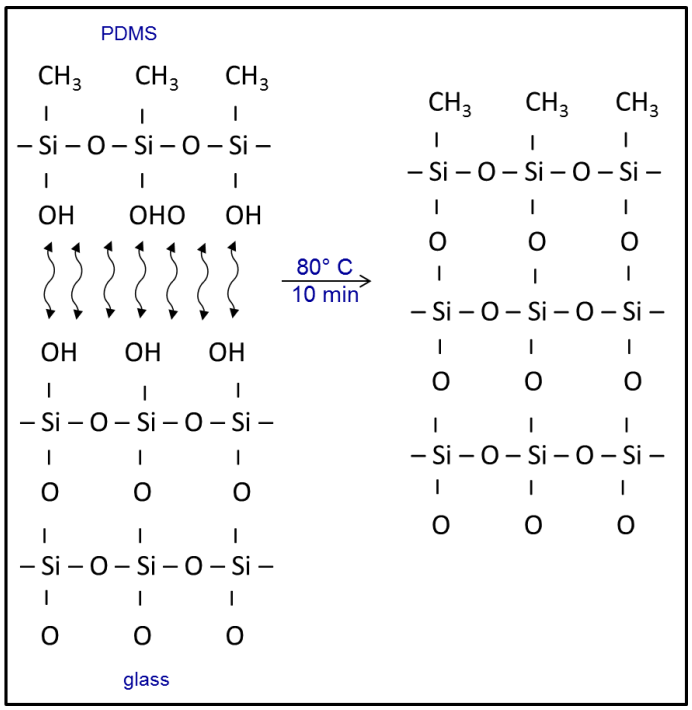

Figure 20. Permanent bond occurs between PDMS and glass surfaces after oxygen plasma treatment and heating.

The PDMS and glass bond is now irreversible. Traces of PDMS on the glass slide can be seen when there is an attempt to peel the PDMS off from the glass surface (Figure 21). The bonded materials can no longer be restored to their original state.

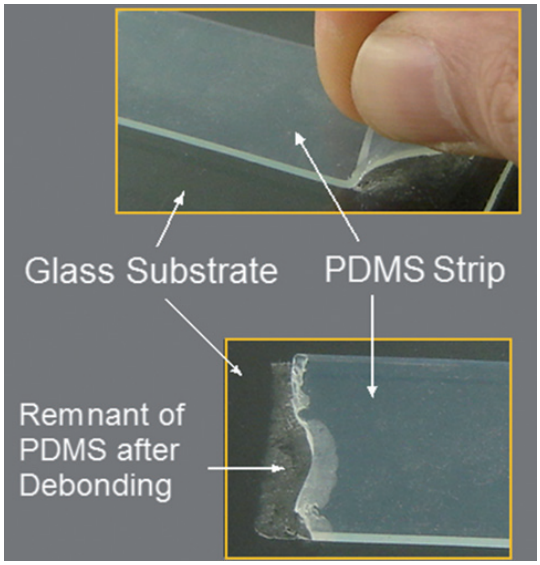

Figure 21. Traces of PDMS on glass surface after peeling is an indication of the irreversible bond and permanent adhesion. The thickness of the PDMS in this picture is 1.6 mm. (Sofla and Martin, 2010)

The two surfaces should be perfectly aligned in order to place the metal part inside the microchannel. The alignment of the PDMS microchannel with the metal was carried out under a stereo microscope. A droplet of water was flowed inside the microchannel in order to observe whether or not the microchannel was open. Due to the difficulty to visually capture the water flow inside the microchannel, a fluorescent dye was added to the droplet. It was then possible to clearly see whether the microchannel was open or not and to see whether the fluid was only in the microchannel in front of the metal and not on top of the metal (Figure 22).

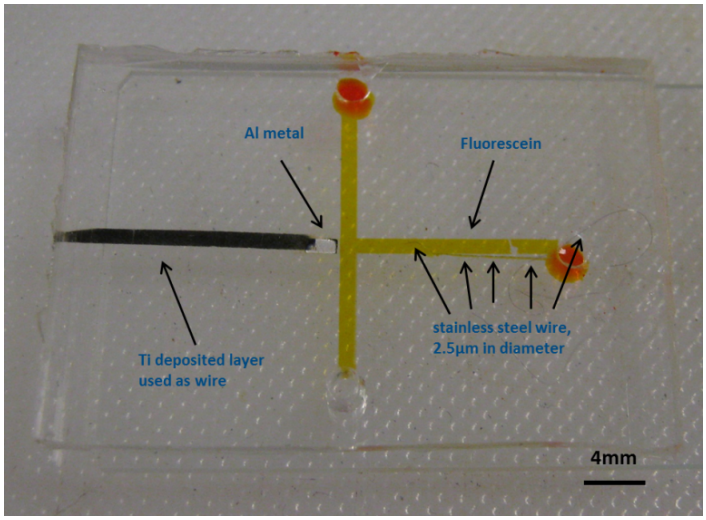

Figure 22. Fluorescent dye dissolved in DI water and flowed inside the microchannel to capture the filling of the microchannel with water.

The change in surface chemistry of the PDMS and glass before and after oxygen plasma treatment was demonstrated with contact angle measurements. When a drop of liquid comes into contact with a solid flat surface, a contact angle can be defined using Young's equation (Bekou and Mattia, 2011):

$$\gamma_{LV}\cos\theta = \gamma_{SV} - \gamma_{SL} \qquad [8]$$

where θ is the contact angle, γ_{LV} is the liquid-vapor surface tension, γ_{SV} is the solid-vapor surface tension and γ_{SL} solid-liquid surface tension, see the triple line in Figure 23.

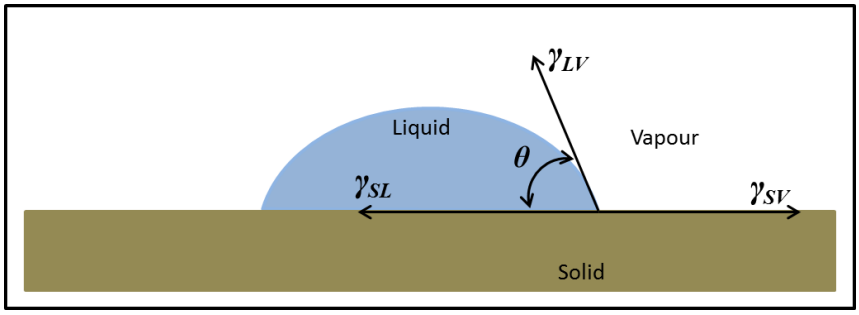

Figure 23. Contact angle measurement on a solid flat surface.

The tendency of a solid surface to be liquid-wet is the wettability. For example, when the water drop tends to spread out on the surface and cover it. A small contact angle, $\theta < 90^{o}$, demonstrates a hydrophilic surface, i.e. strong wettability. A large contact angle, $\theta > 90^{o}$, demonstrates a hydrophobic surface, i.e. weak wettability.

Figure 24 shows the wettability of the PDMS surface before and after plasma treatment. The top left hand side image shows the PDMS surface before the oxygen plasma treatment with a drop of water on top; the hydrophobic behaviour is clear (Ahmed, 2001). In comparison, the bottom left hand side image where the glass surface has a drop of water on top shows a contact angle of 30°, which is clearly more hydrophilic than the PDMS. On the right-hand side image, both surfaces present superhydrophilic behaviour as the water drop spreads all over the surface and it is difficult to calculate the contact angle from the image. At this stage, if the two surfaces come into contact they make a permanent bond with irreversible chemical conditions as described in Figure 21 previously.

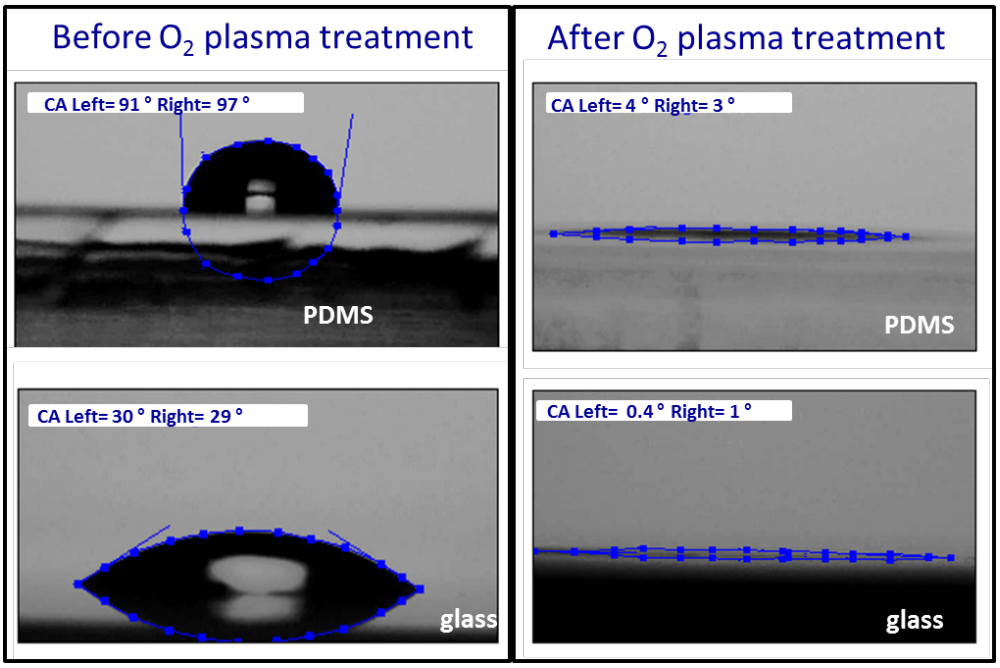

Figure 24. Contact angle measurements: on the left hand side of the figure show a water drop on top of the PDMS surface with an angle of 91-97 ° and on top of the glass surface with an angle of 29-30 °. On the right hand side the same measurements on the same surfaces after oxygen plasma treatment and the contact angle was quasi zero.

3.1.6. Wire connections and holes punched to reach the microchannels

Once the metal deposition is complete and before the oxygen plasma treatment, holes were punched, and wires were connected to the device. The wires are necessary to connect the device to a power supply, acting as the electrodes of the device. The holes are necessary in order to leave the microchannels open so solvents can flow freely in the channels. The holes were created using a hole-punch (Neilsen hole punch set) (Figure 25).

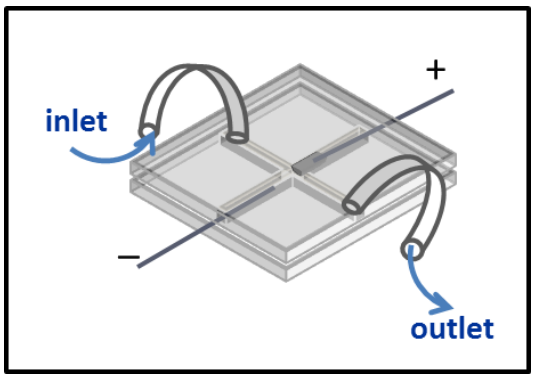

Figure 25. Lab-on-a-chip with aluminium layer deposited in the middle of the cross, connected with electrodes and tubing fitted across the other microchannel.

Three types of electrode assemblies were tested (Figure 26): The first one was used to deposit a metal, i.e. Ti, in one microchannel containing the determining (i.e. aluminium or gold) metal layer and leaving the other crossing microchannel free. The titanium metal-wires deposition took place straight after the metal in determination deposition using physical vapor deposition method, as explained int 3.1.4. section. The second one was used to deposit Ti metal on the side containing the determining metal layer and on the other side make a small incision on the PDMS surface and stabilize the wires inside the polymer. The third one was used to make two small incisions in the PDMS surface and place a wire in each one, thus contacting the metal layer.

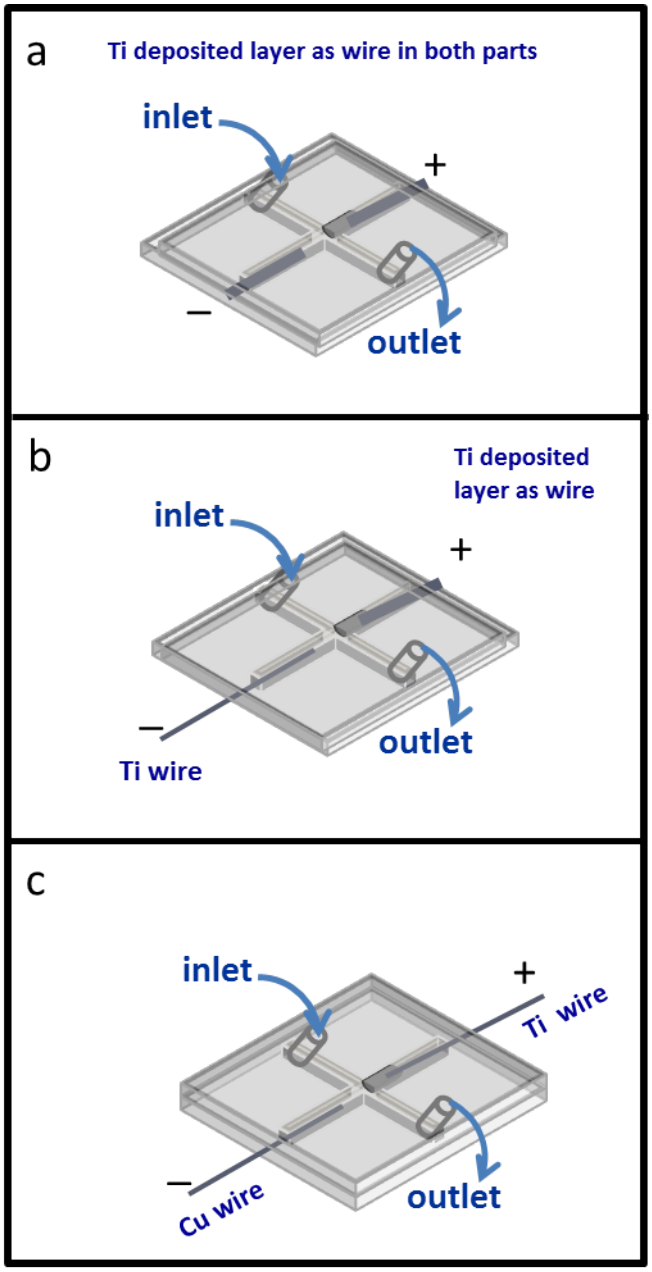

Figure 26. Three methods to introduce wires into the device: a. A titanium layer was deposited inside the microchannel; b. in one part a titanium layer was deposited inside the microchannel and a titanium wire was placed in the microchannel on the other part; and c. a titanium wire and a copper wire were placed inside the microchannel.

The first method (Figure 26a) caused problems and was very difficult to handle. When the deposited layer was on the glass surface, the banana-clip connectors would scratch the

metal layer off. On the other hand, when the layer was on the PDMS surface there were small, up to nanometre, gaps in between the metal molecules, resulting in no current. The third assembly worked best: A thin wire, 25-75 μm in diameter, was placed on the PDMS substrate and stabilized, i.e. left in place, inside the small incision which made it easier to handle. The oxygen plasma sealing follows once the wires have been placed on the device.

3.2 Lab-on-a-chip for aluminium anodization

The device was connected to an external syringe pump in order to carry out aluminium anodization. The tubing was stabilized in place with silicon glue, to avoid ejection during the pressure build up when using the syringe pump. Prior to applying the silicon glue the PDMS surface was coated with a primer to improve adhesion. The silicon glue was the only glue capable of retaining the flexibility of the tubing for easier handling. The first experiment was to carry out aluminium anodization.

3.2.1. Aluminium anodization

The aim of anodizing the deposited aluminium inside the microchannel was to obtain long alumina nanopores, namely nanochannels, integrated within the microchannel and parallel to the substrate. A thickness of 1 μm was necessary, achieved only with an e-beam evaporator could this be achieved.

The lab-on-a-chip was connected to a syringe pump (Figure 27) to pump the electrolyte solution into the microchannel and the wires were connected to a power supply.

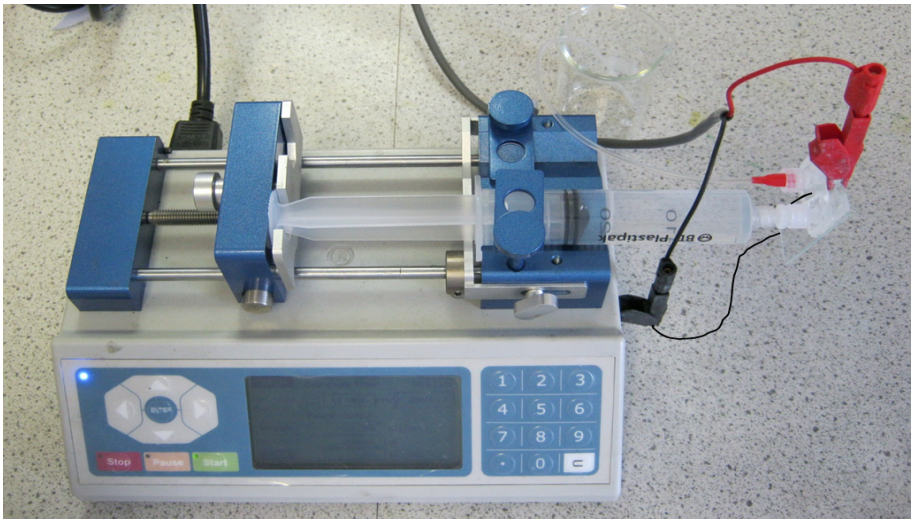

Figure 27. A syringe pump connected to the lab-on-a-chip, to pump acid inside the microchannel in order to carry out aluminium anodization.

The aluminium anodization process involves the formation of an aluminium oxide (Al_2O_3) layer through an electrochemical process resulting in a porous structure. The main objective of this experiment was to create nanopores that were parallel to the microchannel. This was achieved through a number of steps: First the aluminium deposited sample was removed from the e-beam hence exposing aluminium to air which made an aluminium oxide layer. While the acid was flowing through the channel, it came into contact with the oxide and reacted with it. This exposed the aluminium metal underneath the oxide leading to the anodization of the top surface instead of the very thin edges. This reaction is energetically favourable.

An experiment was also carried out to prove that titanium metal can protect aluminium metal from atmospheric oxygen. This experiment was repeated with zinc metal and silicon dioxide.

3.3 Lab-on-a-chip with gold for biosensing

For the biosensing experiments the device contained a gold layer. The gold deposition was carried out with the thermal evaporator for a thickness of 100 nm. It is also useful to note that the e-beam evaporator can be used for smaller thicknesses, from 1-100 nm, but with an important disadvantage. The quantity of the material necessary to carry out a deposition is at least 1 g of metal, which makes it inconvenient to use with metals as expensive as gold. It is important to note that the gold with the glass has poor adhesion (Khoury and Atoui, 2010). For this reason, the gold cannot be deposited directly on to glass surface. An intermediate metal, such as chrome or titanium has to be used to link them together.

Once the device had been sealed with oxygen plasma, and the wires connected, it was ready for use. It was processed for biosensing use without any intermediate step of washing the gold layer. Once the sample had been exposed to the oxygen plasma - in order to bind the glass with the PDMS - the gold layer had been cleaned and was ready for the following DNA immobilization step.

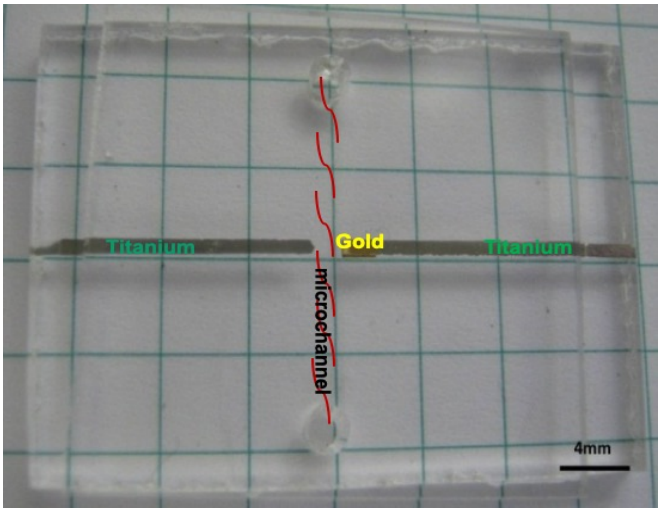

Figure 28. The device containing a gold layer and electrodes across the gold with deposited titanium.

The first sample was made as a two-electrode cell (Figure 28) connected to a potentiostat for cyclic voltammetry (CV) and electrochemical impedance spectroscopy (EIS) measurements. Cyclic voltammetry is an electrochemical technique applied in an electrolytic cell to measure the quantity of the developed electric charge under conditions (Isaacs et al., 2006). Electrochemical impedance of an electrochemical system determines the amplitude of the current to an applied potential. Electrochemical impedance spectroscopy (EIS) is a characterization method of an electrochemical process, namely: characterization of the changes at a surface under specific system parameters and tailored system parameters in order to obtain a desirable effect on a surface.

Table 3 describes the electrical elements, resistance and capacitance depending on current, voltage and impedance and their equations. The impedance of a resistor is independent of frequency and has no imaginary component. With only a real impedance component, the current through a resistor stays in phase with the voltage across the resistor.

The impedance of an inductor increases as frequency increases. Inductors only have an imaginary impedance component. As a result, the current through an inductor is given with respect to the voltage. The impedance versus frequency behaviour of a capacitor is opposite to that of an inductor. A capacitor's impedance decreases as the frequency is increased. Capacitors also only have an imaginary impedance component. The current through a capacitor is given with respect to the voltage (further calculations and relation to each other can be seen in Appendix 2 section 8.2.2.).

Table 3. Common Electrical elements

Component	Current versus Voltage	Impedance
Resistance (Ω)	$E = I\,R$	$Z = R$
Capacitance (F)	$I = C\,\frac{dE}{dt}$	$Z = \frac{1}{i\omega C}$

The device was used for two experiments involving DNA. The DNA strand can be strongly linked onto the gold layer using a thiol linker (Yan et al., 2005). In both experiments a thiol linker with different DNA chains was used. The DNA strand was an aptamer which was able to recognize and capture a biological molecule. The biological molecules in examination were ochratoxin A (OTA) (see Figure 29) and α-human thrombin (see Figure 30).

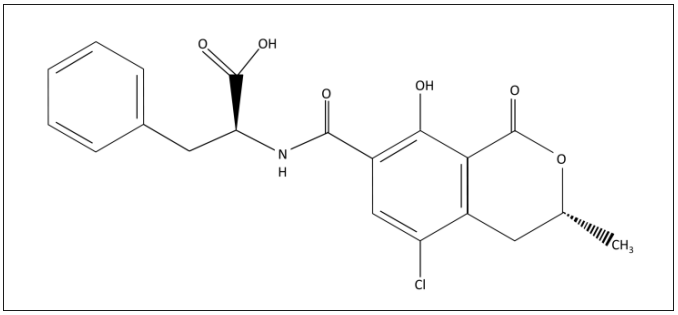

Figure 29. Chemical structure of ochratoxin A; structurally consists of a para-chlorophenolic group containing a dihydroisocoumarin moiety that is amide-linked to L-phenylalanine (Khoury and Atoui, 2010).

Figure 30. Structure of complex involving α-human thrombin in blue (Maryanoff, 1993) .

3.3.1. Recognition and capture of ochratoxin A

The first experiment was DNA immobilization on the gold surface for recognition and capture of ochratoxin A. The potentiostat can maintain a constant potential on the working electrode, with respect to the reference electrode by adjusting the current at the counter electrode. The physical setup for a two-electrode cell presents the current and sense leads connected together, i.e. Reference (R) and Counter (C) inputs in the potentiostat are connected together. In Figure 31, the two-electrode cell set is shown; on the left hand side is

the two electrode cell set up and on the right hand side is the representative circuit consisting of a counter/reference electrode and a working electrode.

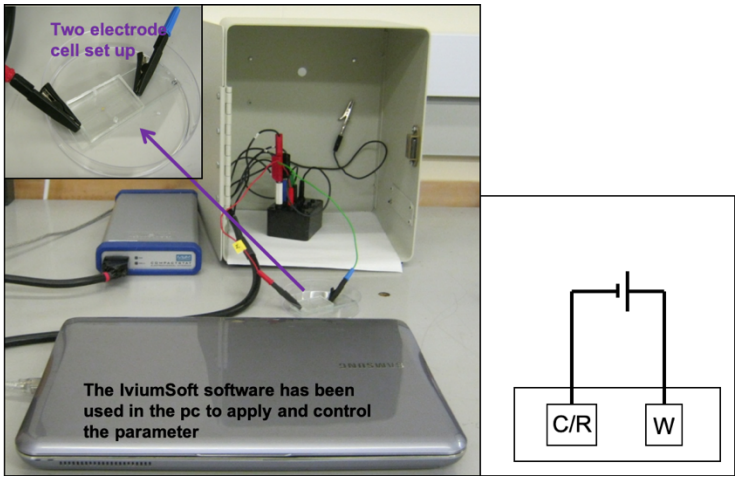

Figure 31. Two electrode cell set up using a sample with wires as electrodes.

The DNA molecules are negatively charged hence they migrate towards the positive gold electrode where they are immobilized. The electrochemical process was able to quantify the amount of immobilized DNA as the increase in DNA molecules deposited on the gold electrode surface led to an increase in the electric current (Demeke and Jenkins, 2010). The entire gold electrode surface area was fully covered with DNA molecules, as shown by the measurement of a constant current. The DNA immobilization on the gold surface facilitated the recognition and capture of ochratoxin A. Figure 32 shows schematically the procedure of DNA immobilization on the gold surface and the capture of ochratoxin A.

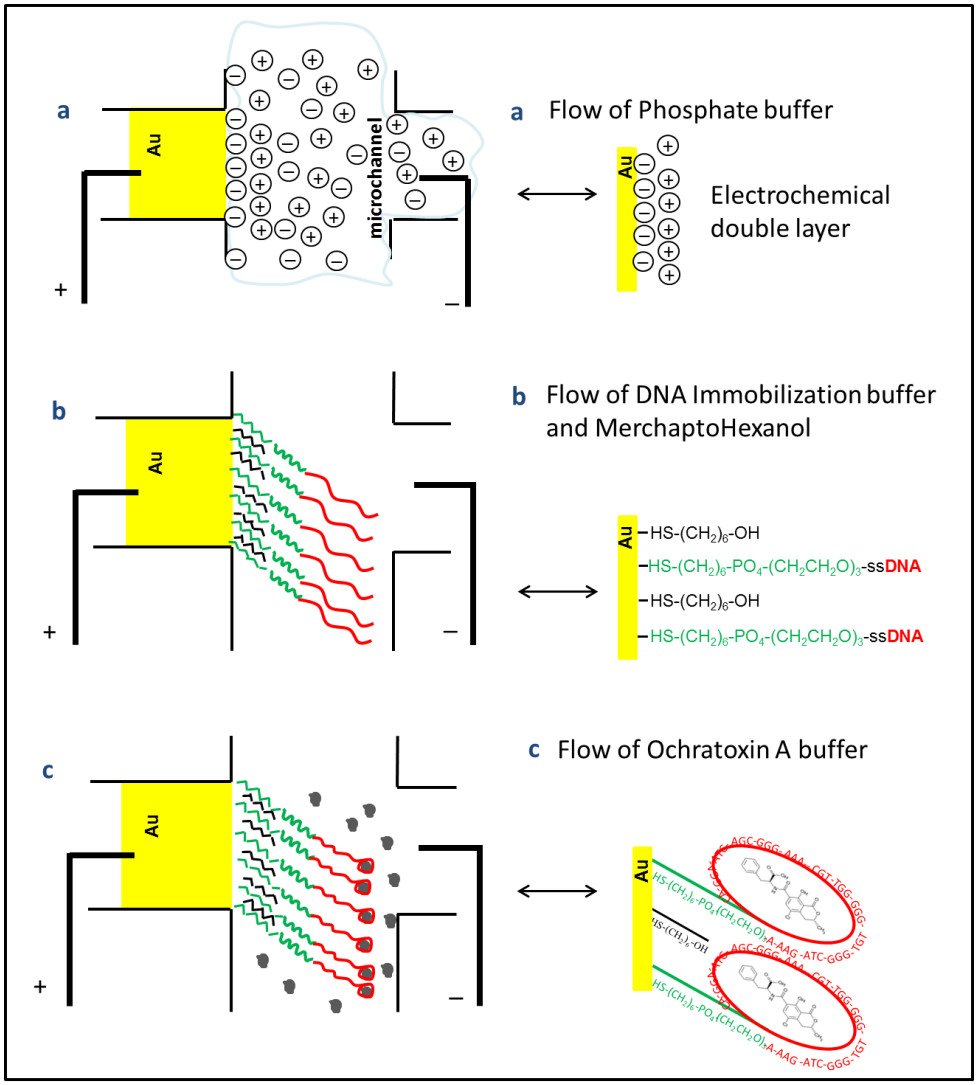

Figure 32. Schematic to represent a) the immobilization procedure b) for immobilizing DNA on the gold surface and c) capturing of ochratoxin A.

3.3.2. Recognition and capture of α-human thrombin

Recognition and capture of α-human thrombin was the next biosensing experiment to be conducted using the same size microchannel width as the first experiment (100 µm). However, the phosphate buffer step was not included to prevent salt from sticking on the

gold electrode's surface. The process was started by filling the microchannel with DNA-immobilization buffer and left overnight in humid conditions.

α-human thrombin (Sigma Aldrich) is obtained from zymogen prothrombin proteolytic activation. α-human thrombin exists in the form of a two-chain serine protease of mass 37 kDa. The active part of α-human thrombin is located within the massive chain. It has high specificity for a particular arginine bond present in the protein substrates. The primary substrate refers to the fibrinogen through which the conversion of thrombin to fibrin through a cleavage process of 4-arginyl-glycyl peptide bonds is facilitated. α-human thrombin plays a significant role in the activation of platelets, protein C, TAFI (Plasma procarboxypeptidase B) and factor C (Berscheid et al., 1992).

Thrombin detection in blood plays a significant role in the clinical analysis process. The interaction between thrombin and fibrinogen leads to the clotting of blood. Additionally, thrombin also functions as a hormone during platelet activation and thrombosis. The thrombin concentration in the blood varies - it is absent in normal conditions of the blood but coagulation processes may see it reach low-micro-molar concentrations (Butenas et al., 1999).

Aptamers are recognized bioanalytical tools for sensitive and rapid detection of protein and development of protein arrays. One well-known thrombin inhibitor is the thrombin aptamer (a single-stranded DNA oligonucleotide 5'-GGTTGGTGTGGTTGG-3'). The interaction mechanism includes aptamer binding to the exosite anion, acting as a platelet thrombin receptor and thrombin inhibitor. The particular thrombin/aptamer binding interaction has been used to develop biosensors similar to the one used in the research

presented here. Electrochemical impedance spectroscopy has created a very sensitive thrombin biosensor whose effectiveness stretches below the picomolar range (Mir et al., 2006).

In the experiment, the α-human thrombin was added to the microchannel. The first step involved the removal of magnesium from the microchannel through the addition of a 10 mM EDTA solution dissolved in phosphate buffer. After the DNA-strands had been deposited on the gold surface, various solutions were added including ferro-/ferri-cyanide solution (5 mM) comprising of 10 mM potassium hexacyanoferrate II ($C_6FeK_4N_6.3H_2O$ II) and 10 mM potassium ferrocyanide III ($K_3Fe(CN)_6$ III), and α-human thrombin solution (500 nM) containing 426 µL ferro-/ferri-cyanide solution and 1 µL thrombin. To determine if the bond had been formed between the DNA-aptamer and thrombin, the microchannel was rinsed with a solution of ferro-/ferri-cyanide and EIS measurements was conducted (Wang et al., 2011).

The selective detection of thrombin using the gold membrane, upon binding the aptamer folds onto its secondary structure, increasing the DNA charge density close to the electrode and hence increasing the electrostatic repulsion to the negatively charged redox marker. In this case, the $[Fe(CN)_6]^{4-}$ as a result of the formed thrombin/aptamer complex. This blockade is evidenced by a reduced voltammetric oxidation signal of $[Fe(CN)_6]^{3-}$ from $[Fe(CN)_6]^{4-}$, therefore allowing thrombin detection and quantification. Notably, the reduced voltammetric signal after aptamer/thrombin complex formation can be linked to dual effect founded on charge repulsion and the steric blockade effect (Huang and Zhu, 2009). The individual aptamer leads to a reduced signal strength in comparison to bare membrane signals (Hu et al., 2009).

Since the aptamer carries a negative charge, it repels the $[Fe\ (CN)_6]^{4-}$ which is also negatively charged. This leads to a reduction in ionic diffusion at the gold electrode and later a reduction in voltammetric re-oxidation. This signifies a successful formation of the thrombin/aptamer complex, a reaction that facilitates recognition and quantification of thrombin. 1 mM $K_3[Fe(CN)_6]$ / 0.1 M $NaNO_3$ acts as a redox indicator at pH 7.5 which enables thrombin to exist with a negative charge (Liu et al., 2010b). It is the combination of the negative charge of thrombin and the charge density change of the DNA aptamer that enables it to repel $[Fe(CN)_6]^{4-}$ resulting in reduced voltammetric signals. The average size of thrombin is 4 nm, and it is this size that makes it create a higher steric blockade of the nanochannel than that of a free aptamer. Use of a gold positive electrode amplifies the entire process of thrombin detection and quantification.

3.4 Conclusions

Throughout this chapter the techniques used for the fabrication of lab-on-a-chip devices have been discussed in detail. It is possible to use the devices for different applications by changing only one step in the fabrication procedure. i.e. the metal deposition procedure. The metals of interest for the lab-on-a-chip applications were namely aluminium and gold. The aluminium was used for aluminium anodization and the gold for biosensing. Furthermore, an optimization procedure was discussed to improve the devices and achieve the desired and planned results.

4. Results

4.1 Lab-on-a-chip devices

4.1.1. Lab-On-A-Chip Device Fabrication

The fabrication process involved various processes namely wet chemical etching for microhill fabrication and poly-dimethyl-siloxane (PDMS) for microchannel fabrication. The wet chemical etching done was an anisotropic process. 1 mL hydrochloric acid (HCl) and 10 mL of silicon dioxide etchant mix (comprising of ammonium chloride and hydrofluoric acid) (20:1) were used as etchants. These chemicals were used due to their corrosive nature. This etching process facilitated the creation of microhills on a glass substrate. The depth of the microhills were 4 µm with a width of 1 mm and were observed using a profilometer with the results shown in Figure 33.

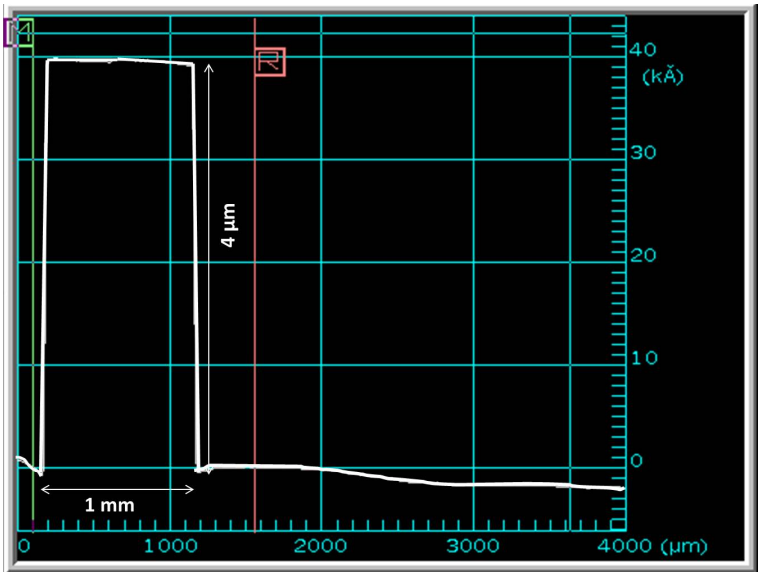

Figure 33. Profilometer measurement shows the microhill with depth 4 µm and width 1 mm.

4.1.2. Fabrication of microhills by wet chemical etching

Silicate glass wet chemical etching in aqueous HF solution has been explored for a long period. The etching process of silicate glass involves dissolving a part of the surface in an HF aqueous solution. The reaction involved in the etching of silicate glass is represented using the chemical formula:

$$SiO_2 + 6HF \rightarrow H_2SiF_6 + 2H_2O$$

The above equation represents the reaction that is involved in the heterogeneous dissolution of SiO_2. The crystalline or vitreous SiO_2 is made up of tetragonal units that are linked at all four corners with SiO_4 covalent units. This system forms a three-dimensional structure that is covalently interconnected. The aqueous HF, therefore, has to overcome the strength of the four siloxane bonds so as to dislodge silicon from the glass (Hnatovsky et al., 2006).

The etching of silicate glass in the experiment relied on the activation energy of ultraviolet (UV) light. Notably, the surfaces of the glass wafer that were to be protected from the effect of the HF acid and the UV light activation energy were protected using an etchant mask. In the experiment, the depositing and patterning of the mask on the wafer were done using lithography techniques. The chrome metal, in this case, acted as the etchant protection mask due to its ability to absorb UV light and reduce reflection of a particular wavelength. The chrome protection mask in this experiment acted as a photomask and because the photomask was under UV light to produce a specific imprint, the entire process is known as photolithography. The etching rate also depends on etchant composition and its concentration, temperature levels during the etching process, the accuracy of etching and

material to be etched. The etch rate is inconsistent. Due to this inconsistency, the rate of etching was determined in advance before the etching process was started. After the etching process was complete, the sample was withdrawn from the chemical bath then washed thoroughly with water as pointed out in the methodology section. The photoresist material now protectively covered the formed microhills. The formed microhills were exposed through the removal of the photoresist using acetone where they were then further analysed and characterized. As pointed out in the methodology section, the microhills were characterized using an optical microscope (Zeiss microscope) at 10x magnification. The observed microhills had straight lines and rounded corners (Figure 34). The characterization of the microhill width, height and roughness were performed using a stylus profiler (Dektak 6M) profilometer. The microhill formed was 1 mm wide and 4 μm high.

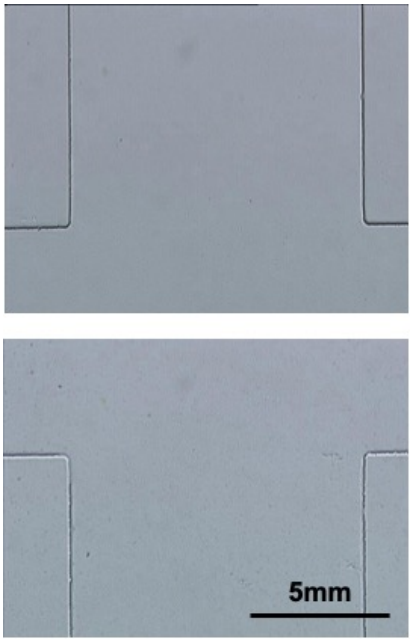

Figure 34. Picture taken under Zeiss microscope using 10x lens. The glass substrate was anisotropically etched, showing microhills on the surface.

4.1.3. Microchannel Fabrication using poly-dimethyl-siloxane (PDMS)

The microfluidic chips are defined by their microchannel features and size. Sizes below 100 μm are beneficial to the field of science since they transport substances for short distances through special flow characteristic (Tang et al., 2006). Various microfluidic fabrication techniques have been developed leading to the emergence of various micro-flow technologies. Microchannel fabrication methods are commonly based on photolithography. Microchannels are routinely being fabricated using conventional soft lithographical techniques. However, the photolithography technique is hard-to-command and expensive, and therefore not worthwhile using in the fabrication and prototyping of some special microstructural patterns. PDMS is a cheaper material compared to traditional microfabrication materials including glass and silicon. PDMS also has good optical properties (transparent from a wavelength of 230-700 nm within 190-700 nm range). In these experiments, PDMS was transparent after it was poured onto the surface of the etched glass slide.

4.1.4. Physical Vapour Deposition of Metal on the Wafer

The physical metal deposition is done either by evaporation or sputtering. This method is applied in the deposition of thin films onto substrates layer by layer. The method utilizes both thermodynamic and mechanical means in order to produce thin films, and it depends on a low-pressure environment for the process of vaporization to occur successfully. The experiment used the physical vapour metal deposition method to deposit a controlled thickness of evaporated metal films to a solid surface under vacuum.

The metal deposition was completed in a vacuum to allow the wolfram coil to generate an electron beam which, upon bombarding the metal vapour, makes these particles to travel to the target substrate directly without colliding with the air molecules. The vacuum was maintained at 3.6×10^{-6} mbar so as to provide ample space for evaporation and travel of the metal particles. The vacuum created a free space to prevent a scenario where the deposited material was a metal compound arising from the reaction between the free metal particles and gas molecules. In one of the experiments, the deposited material had oval pores implying that it was not pure. The oval porous aspect of the deposited material from this unsuccessful experiment was due to the deposition of alumina instead of the intended aluminium metal. The use of the Edwards Electron Beam Evaporator Auto 306 (e-beam) and the Thermal Evaporator FL 400 depended on the desired thickness of the metal deposit and the quantity of the metal in use.

The desired metal was placed in in a tungsten boat. Tungsten metal was selected for this procedure due to its high melting and boiling point. After placing the metal on the tungsten boat, the boat was connected across to two electrodes and a suitable current was passed through the boat to melt and vaporize the metal. A slow rate of deposition was used to ensure that a smooth metal layer was deposited. The e-beam was used to form a layer approximately 1 μm thick, unlike thermal evaporation that can achieve a 300 nm thickness. Table 4 shows the current, boat, crucible and deposition rate parameters to perform metal deposition using e-beam and thermal evaporators.

Table 4. The crucible type and the amount of current used for each different metal, using thermal and e-beam evaporators. The crucible type differs for each different metal in order to remain inert during the evaporation process.

metal / ***Thermal evaporator***	**Aluminium (Al)**	**Titanium (Ti)**	**Chromium (Cr)**	**Gold (Au)**
Current (Amp)	25-35	30-45	30-35	25-30
Boat	Tungsten (Tg)	Tg	Tg	Tg
Deposition Rate (nm/s)	0.05	0.19	0.3-0.4	0.1-0.3
metal / ***e-beam evaporator***	**Al**	**Ti**	**Zinc (Zn)**	**Silicon Dioxide (SiO_2)**
Current (mAmp)	90-110	80-100	10-15	18-24
Crucible	Boron nitride (BN)	Titanium carbide (TiC)	Aluminium oxide (Al_2O_3)	Al_2O_3

The metal was deposited two different surfaces. The first surface was PDMS and the metal was deposited directly into the microchannels. The second surface was the direct deposition onto a clean glass slide. The PDMS surface was cleaned to remove any sticky substances that would attract dust particles. However, the metal deposition lead to inconsistent results (Figure 35).

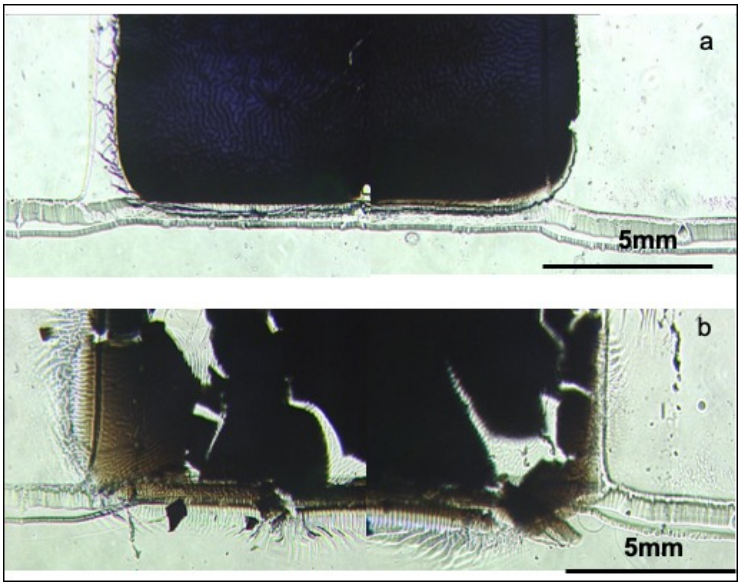

Figure 35. The metal deposition on the PDMS surface initially gave inconsistent results, with both (a) a uniform layer and (b) a broken, flaky one, which also damaged the PDMS.

The method was substituted by metal deposition onto a glass surface. The result of metal deposition on the glass surface was observed under an optical microscope and can be seen in Figure 36. The surface of the metal is smooth with no cracks or gaps. The surface smoothness was also confirmed using a field emission scanning electron microscope (FESEM). Figure 37 shows an image of the surface taken with an FESEM.

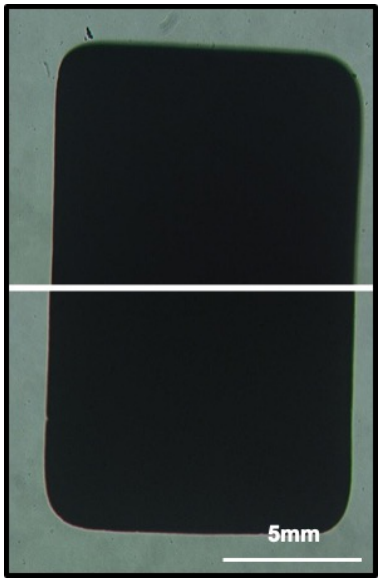

Figure 36. The picture is taken under Zeiss optical microscope, using 20x lens, and show of the layer of metal deposited on a glass surface.

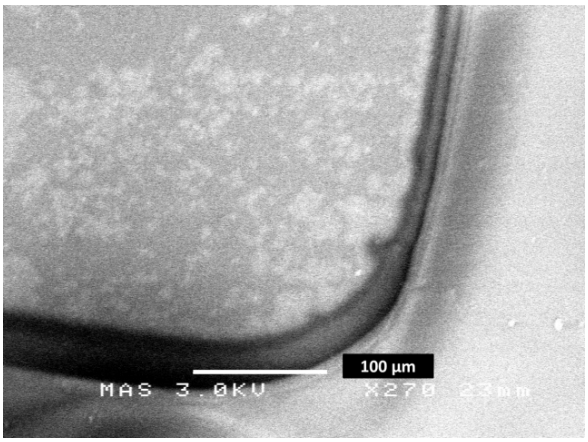

Figure 37. Representation of the aluminium surface before anodization using FESEM.

4.1.5. Oxygen Plasma exposure of PDMS and Glass Surface

Oxygen plasma cleaning systems are frequently used in the fabrication of MEMS to promote adhesion of incompatible materials. The treatment of surfaces with oxygen plasma, also known as surface activation, leads to surface alteration, hence creating a strong bond between the materials that would otherwise have weaker or no bonds (Eddings et al., 2008). PDMS' Oxygen plasma treatment refers to a normal technique that facilitates bonding to glass, silicon, PDMS and other materials so as to seal microfluidic devices.

A Zepto Oxygen Plasma system was used. This system was able to generate capacitively coupled plasma through the application of a single radio-frequency (RF) power. The surfaces of PDMS and glass were cleaned thoroughly and treated with oxygen plasma, aligned and placed in a chamber with plasma power plasma 25 W with an oxygen flow of 25 sccm for 25-30 seconds. The oxygen ions in the plasma react with the superhydrophobic PDMS surface, making the material superhydrophilic. Similarly, the glass surface was hydrophilized by the formation of hydroxyl groups on its surface after exposure to the oxygen plasma. A permanent bond could be established between the plasma-treated glass and PDMS, which also ensured that the metal part was aligned perfectly with the interior of the microchannel. The resulting microchannels proved to be water-tight and without any internal blockage.

4.1.6. Wires connection and holes punched to reach the microchannels

The oxygen plasma treatment process was accompanied by punching holes and connecting wires to the device. These wires were used to link the microchannel device to the power supply. Three types of electrodes were tested including depositing Ti in one

microchannel with either a gold or aluminium metal layer. The second method involved depositing Ti metal on the side containing gold or aluminium where an incision was made on the opposite end to provide stability to the wires located on the inside of the plasma. The third process involved making two incisions on the surface of PDMS and placing a wire in each side to provide a contact with the metal layer. Notably, the first and second methods did not give consistent results. The third method which involved placing a 25-75 μm diameter wire inside the PDMS substrate and stabilizing it later gave the best performance. Figure 38 shows the three different device types.

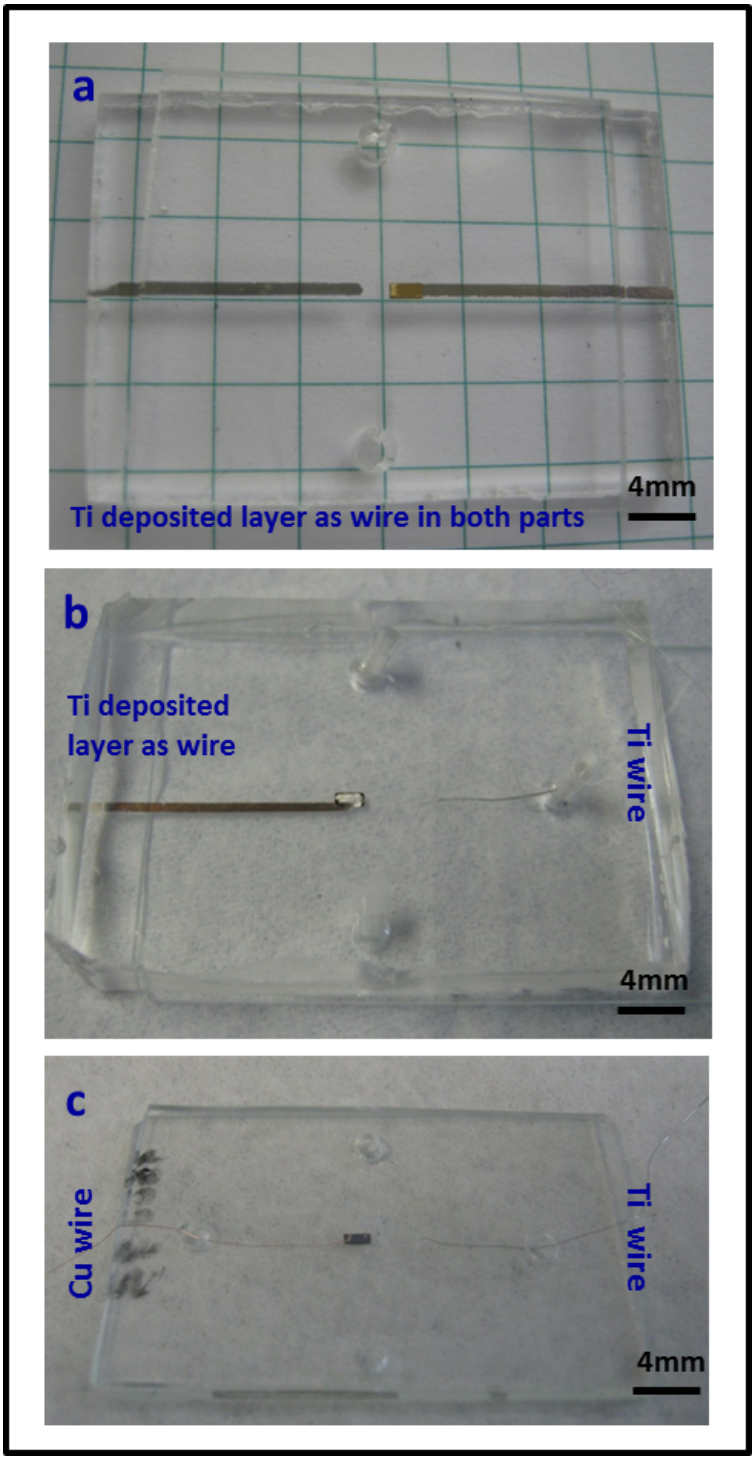

Figure 38. Three different electrode assemblies were used: a) shows the Ti deposited metal layer throughout the channel with the determining metal layer; b) shows the part with the determining metal layer connected with a Ti deposited layer and the other part with a Ti wire fitted; and c) shows Cu and Ti wires connected to the device.

The final lab-on-a-chip device can be seen in Figure 39; the holes were fitted with tubing and sealed with silicon glue. The tubing was used to flow the solvents into the channel safely.

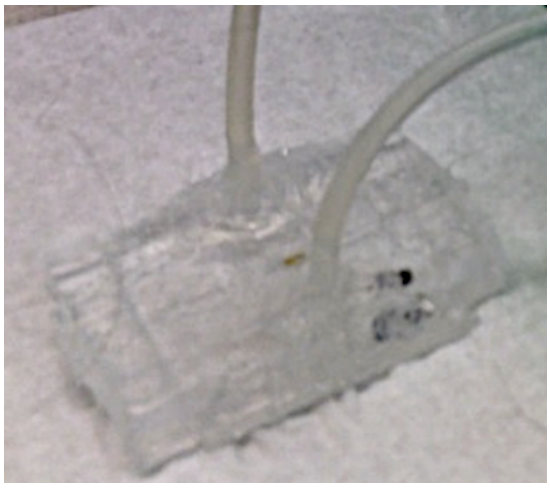

Figure 39. The holes connecting the fabricated channels to the external environment where fitted with tubing and sealed with silicon glue.

4.1.7. Lab-on-a-chip for Aluminium anodization

Anodizing the aluminium deposited in the microchannel was conducted to generate long alumina nanopores referred to as nanochannels. The experimental set-up consisted of a syringe that was used in the pumping of the electrolyte through the microchannel. The wires were linked to the power supply.

The aluminium anodization process formed a layer of aluminium oxide (Al_2O_3) via an electrochemical process. Anodizing the aluminium layer in certain acidic electrolytes by applying a certain voltage can produce a thick oxide coating, containing a high density of

nanopores. The first approach of aluminium anodization by applying a constant voltage was performed by Keller et al. (Keller, 1953). Different acidic electrolytes gave different pore diameters by applying a defined voltage. Firstly, sulphuric acid can be used to give pore sizes between 10-30 nm in diameter by applying 10-25 V. Sulphuric acid has been used in this work. The second acid is oxalic acid which gives pore sizes in the range of 30-80 nm in diameter by applying 35-100 V, which has also been investigated in this work. The third acid commonly used is phosphoric acid giving larger diameters of more than 100 nm by applying a voltage over 100 V, this method is normally used for the fabrication of the commercial alumina discs (anodiscs made by Whatman).

Since both barrier and porous oxide layers are grown on aluminium, the barrier layer was be removed using phosphoric acid (H_3PO_4) to open the formed pores (Fig. 40). The remaining aluminium was removed using copper chloride ($CuCl_2$) (Figure 40). This resulted in the formation of porous alumina nanochannels parallel to the substrate for molecular separation through the nanopores. Once the barrier layer was removed, the aluminium oxide layer presented an open porous layer ready for fluid flow investigations.

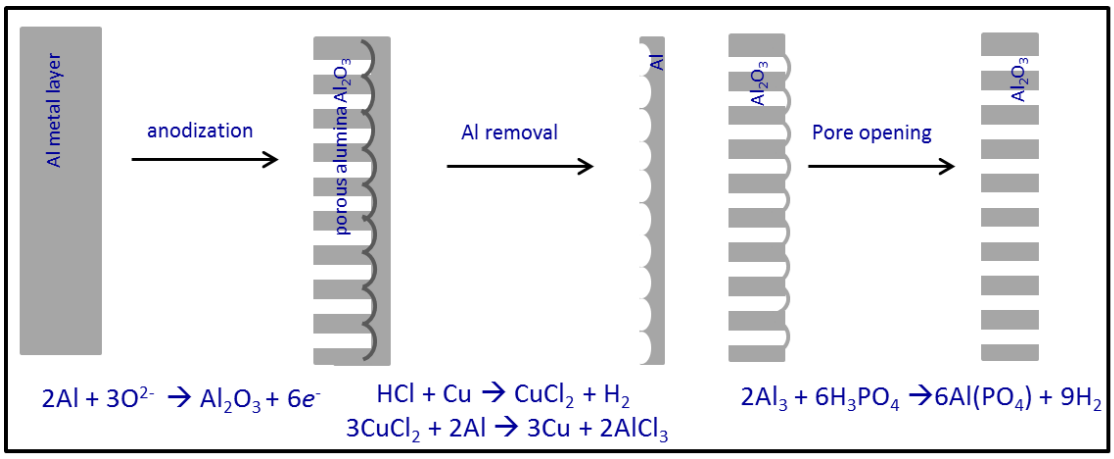

Figure 40. Aluminium anodization procedure.

In the anodization procedure the aluminium piece is the anode by connecting it to a positive terminal of an AC or DC power supply. The cathode is connected to the negative terminal of the power supply. The cathode can be any electronic conductor that is inert in the anodization bath, here stainless steel. Once the circuit is closed, the electrons are drawn away from the metal at the positive terminal, allowing the ions at the metal surface to react with water to form an oxide layer on the metal. The electrons return to the bath at the cathode where they react with hydrogen ions to make hydrogen gas.

Post- anodization, nanopores were observed using a FESEM perpendicular to the substrate rather than parallel to the substrate as hypothesized. The alumina nanopores are shown in Figures 42 and 43. As shown in Figure 42 the nanopores are very disordered with different sizes, this might be because the aluminium layer was not annealed before anodization. Annealing relieves the internal stress of the metal and makes the structure homogeneous and ductile. Furthermore, the porous cross section and the nanodomes of the barrier oxide layer were observed as shown in Figure 43. The experiment was carried out in sulfuric acid at 20V. Figure 41 show the anodization current with time.

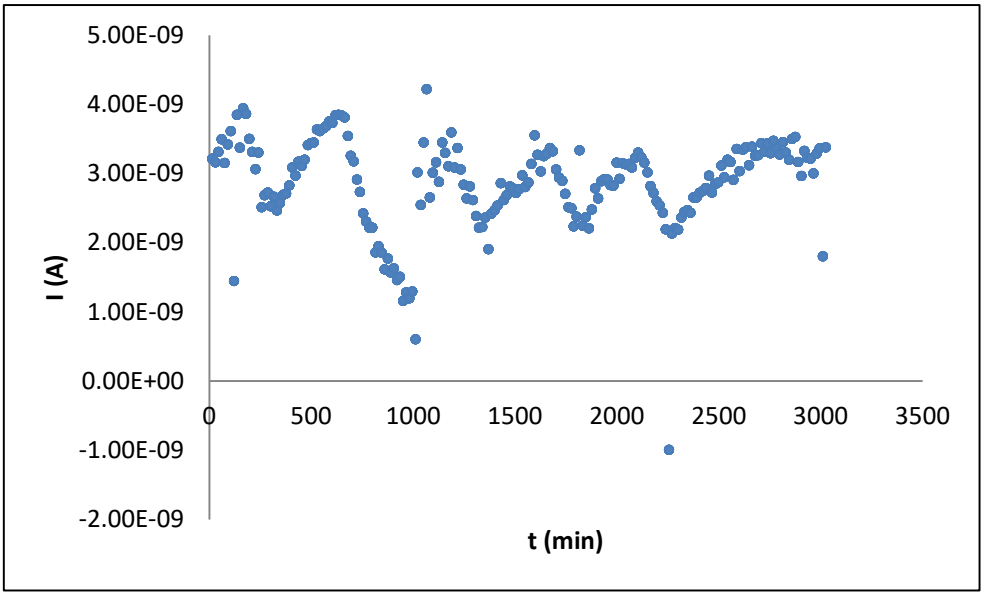

Figure 41. The graph shows the current versus time for aluminium anodization in 0.5M Sulphuric acid at 20 V for 1 hour. The experiment was performed at room temperature.

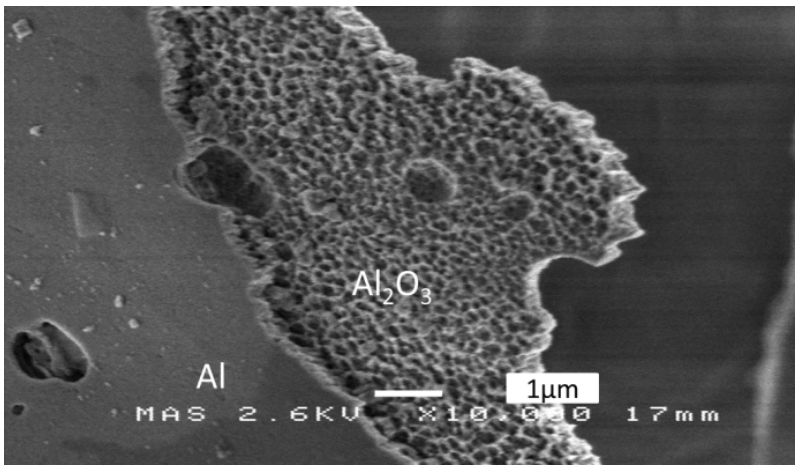

Figure 42. The SEM micrograph shows the transition between metallic aluminium (Al) on the left and anodized aluminium (Al_2O_3) on the right, with visible nanopore formation.

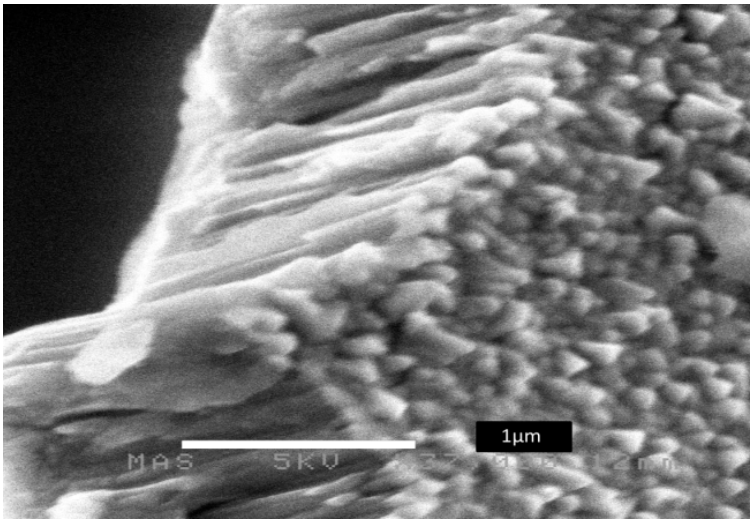

Figure 43. The SEM micrograph shows a cross-section of the anodized alumina, with pores up to 1 µm long and the nanodomes on top which constitute the barrier layer.

A possible explanation for obtaining the nanopores perpendicular to the substrate might be as follows; when the sample was pulled out from the e-beam chamber after aluminium anodization, the aluminium metal immediately came into contact with air and a thin layer of aluminium oxide formed on the surface. When acid flowed into the nanochannel to carry out the anodization it came into contact with the oxide layer and removed it. This removal left a much larger surface area exposed to the acid and thus presented a more favourable reaction pathway in anodizing the top surface rather than the very thin edges.

An experiment was also carried out to prove that titanium metal can protect the aluminium metal from atmospheric oxygen. This experiment was repeated with zinc metal and silicon dioxide.

4.1.8. Aluminium and titanium metals

At this stage, another metal was deposited immediately after aluminium deposition to seal the aluminium layer to prevent contact with air, i.e. seal the aluminium inside the chamber of the e-beam immediately after deposition. This was achieved by depositing a second metal layer on top of the aluminium layer; a metal which does not react with the acid was used.

Thus, a layer of titanium was deposited, at a thickness of 50 nm, immediately after the aluminium layer inside the PDMS-made microchannel. The anodization was then carried out as previously described. Figure 44 shows the aluminium anodization graph, current against time. The result still produced nanopores parallel to the substrate. This time the acid reached the metal surface between the aluminium and PDMS. Figure 45 shows alumina nanodomes which were observed with the titanium flaky layer on top of them. As Figure 45 infers, there isn't good adhesion between the titanium and aluminium, because the titanium layer is completely detached from the aluminium.

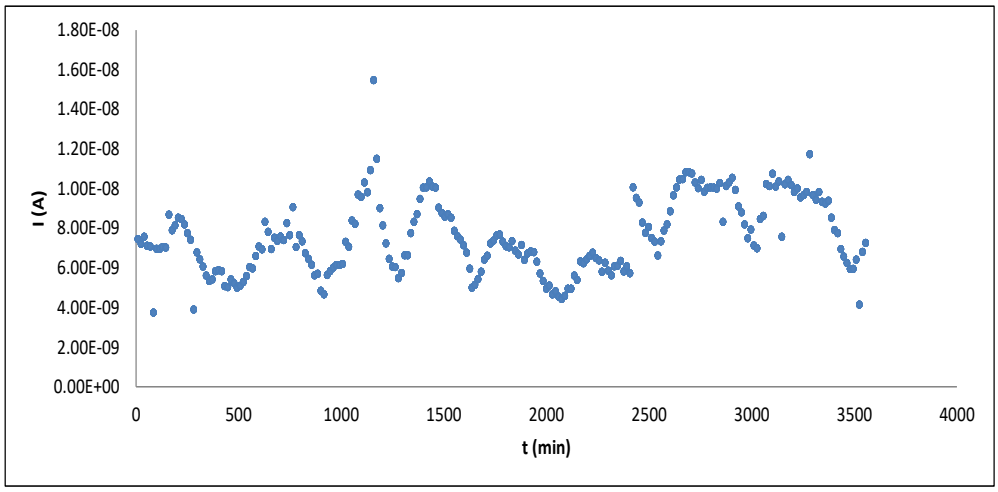

Figure 44. The graph shows the aluminium anodization in 0.5M Sulphuric acid by applying 20V current for 1 hour, performed at room temperature.

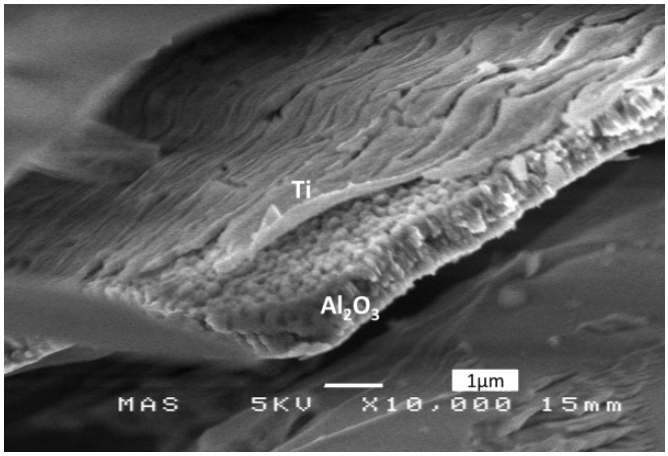

Figure 45. SEM micrograph of alumina nanodomes (Al_2O_3) and a flaky layer of titanium (Ti) on top.

This theory of poor adhesion between the titanium and aluminium layers was completely rejected following the results of the same experiment (Figure 46), where the titanium has taken the same shape of the alumina nanodomes covering the surface after aluminium anodization. In this experiment, the aluminium and titanium deposition were carried out on a glass surface. The fact that the deposition was carried out on a different substrate can affect the adhesion between the metals. It might be caused by heating by the electron beam bombarding the PDMS surface which makes waves throughout the whole deposition time giving unstable results and thus the two metals detach from one another.

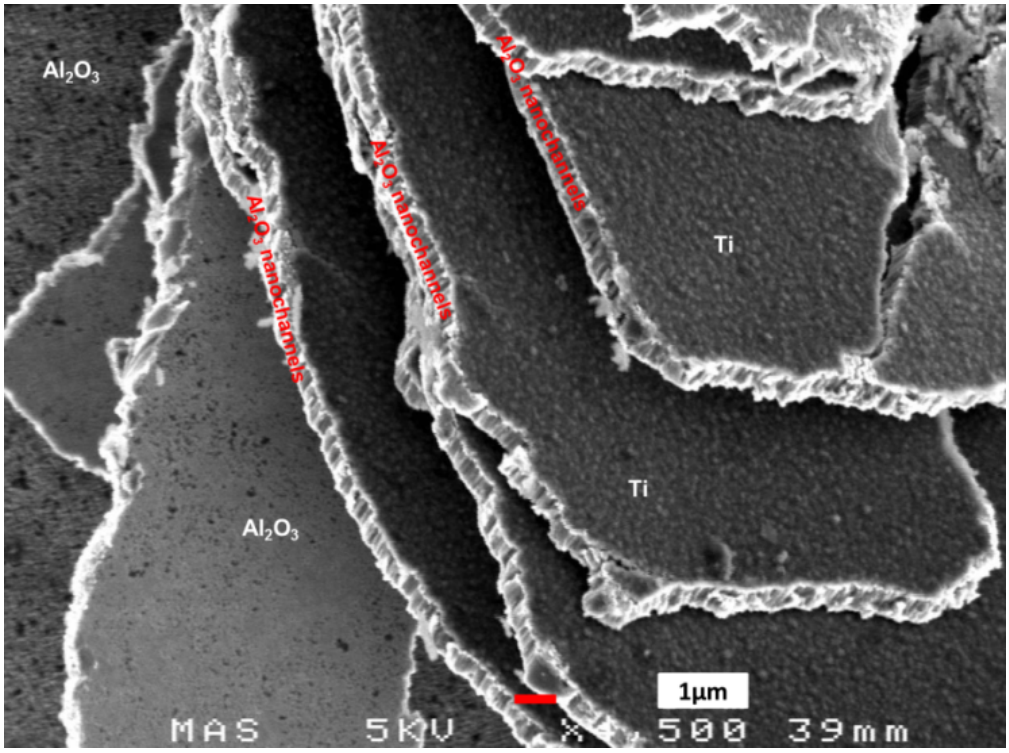

Figure 46. SEM micrograph of Ti nanodomes covering the alumina anodized structured. The bright edges are alumina nanochannels and the opaque surface is porous alumina.

The method of depositing titanium on top of aluminium was repeated several times, with metal deposition on the glass surface as well as using sulphuric acid (0.5 M, in 20 V) and oxalic acid (0.3 M, in 30 V) to carry out the aluminium anodization. Perpendicular pores to the substrate were always observed. At this stage, another metal should be used having better adhesion with aluminium.

4.1.9. Aluminium and zinc metals

The next step was to seal the aluminium layer before coming into contact with air and use another metal (not Ti), due to poor adhesion between titanium and aluminium. The metal

used this time was zinc. The zinc was deposited immediately after the aluminium following the same procedure as described above. The thickness of zinc was again 50 nm.

Figure 47 shows the aluminium-zinc layer under the optical microscope, the layer is smooth without cracks or gaps. The adhesion between the two metals aluminium and zinc was much better than aluminium and titanium (Washburn, 1926 - 1930; 2003).

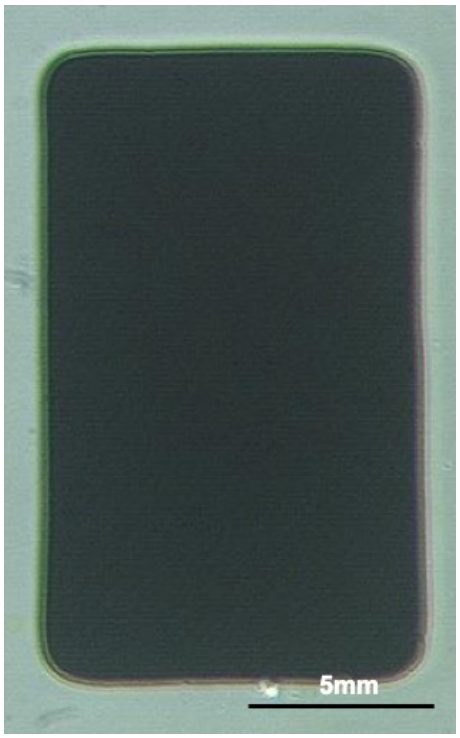

Figure 47. Aluminium-Zinc layer under optical microscope, an n-Plan lens was used.

The aluminium anodization was carried out in sulphuric acid (H_2SO_4) and oxalic acid ($C_2H_2O_4$): $2Al + 3O^{2-} \rightarrow Al_2O_3 + 6e^-$

The two acids produced different result. In both cases the zinc reacted with the acids and gave different structures. The first approach carried out the anodization with sulphuric acid, (see in Figure 48 the anodization graph). The zinc reacted with the acid and gave zinc oxide on top and alumina nanopores on the bottom which were always perpendicular to the substrate. The zinc anodized to zinc oxide (ZnO) together with aluminium giving different structures (see Figure 49) on top of the aluminium. An SEM image is presented below where the ZnO presents two different ZnO structures in the same sample layer, one following the other (Figure 50). In addition, the aluminium on bottom also anodized perpendicular to the substrate, giving porous alumina underneath the ZnO.

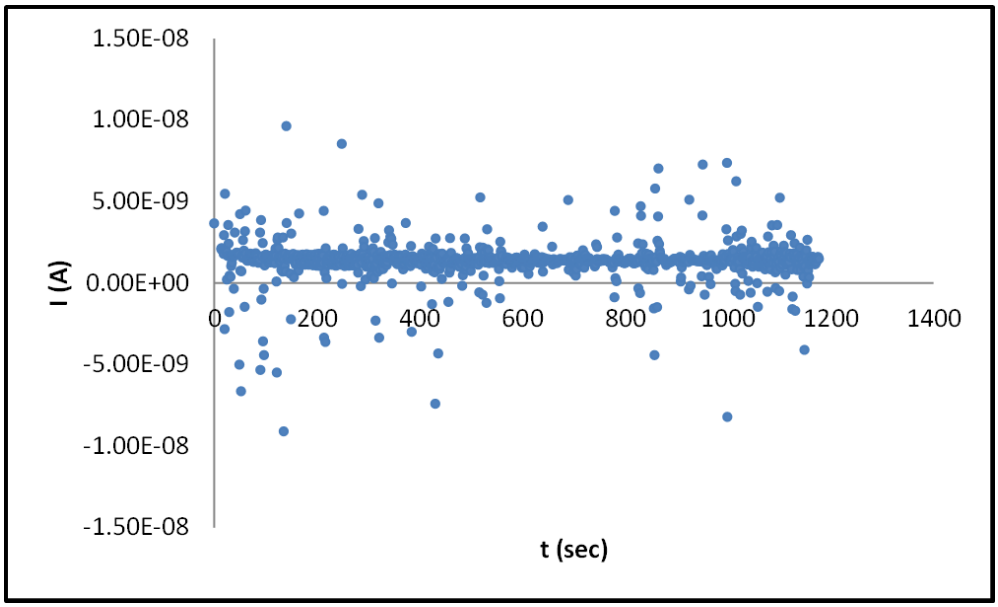

Figure 48. The graph shows the current versus time for the aluminium anodization, performed in sulphuric acid, at 20V for 20 min.

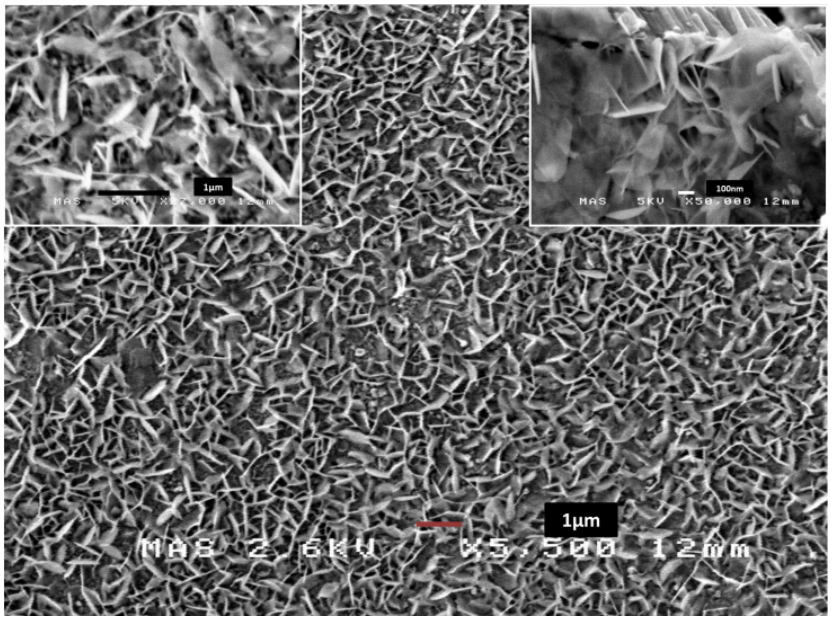

Figure 49. The SEM micrograph shows a zinc oxide petal structure on top and the nanoporous alumina underneath it. The top left inset is the sample at higher magnification where the porous structure can be observed underneath; and the top right inset is a higher magnification micrograph of the same sample showing the nanochannels at the edge of the sample.

This structure has been further analysed in order to demonstrate that it was indeed ZnO all over the sample surface presenting two different structures. The further analysis was a line scan elemental analysis carried out with SEM. The results can be seen in Figure 50 where it is indeed ZnO covering alumina all over the surface. The percentage of aluminium is much bigger than zinc because of the thickness of each metal (see Figure 51b).

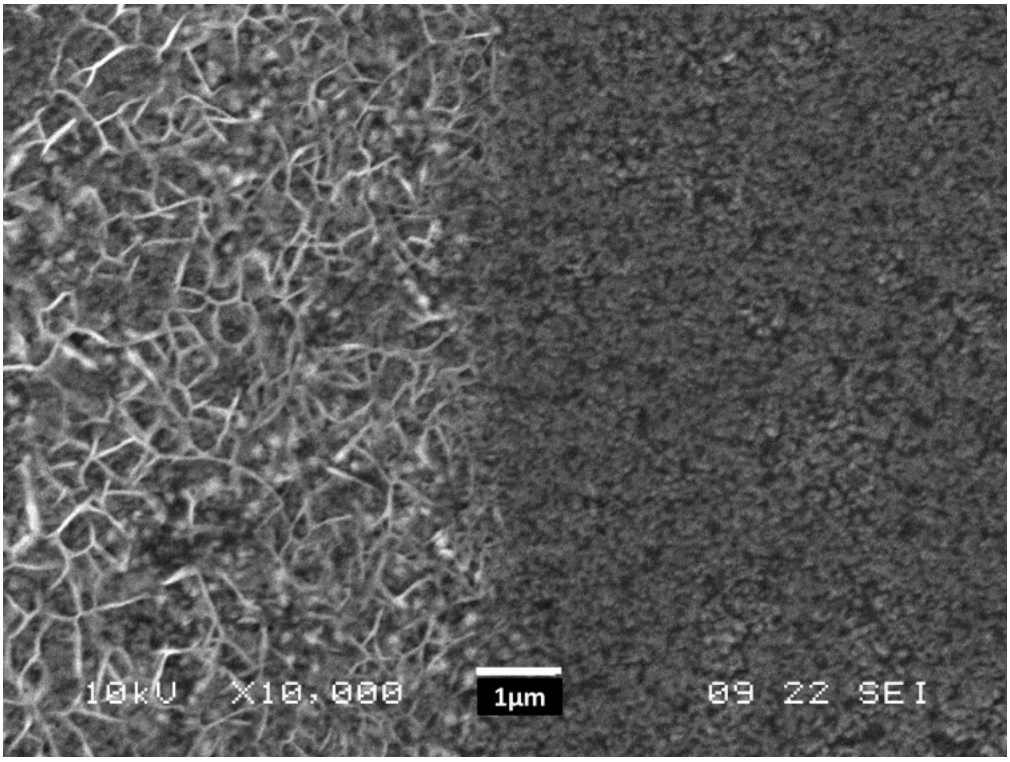

Figure 50. The SEM micrograph shows two types of ZnO structure one following the other in the same sample surface. On the left-hand side is the ZnO petal structure and on the right porous ZnO.

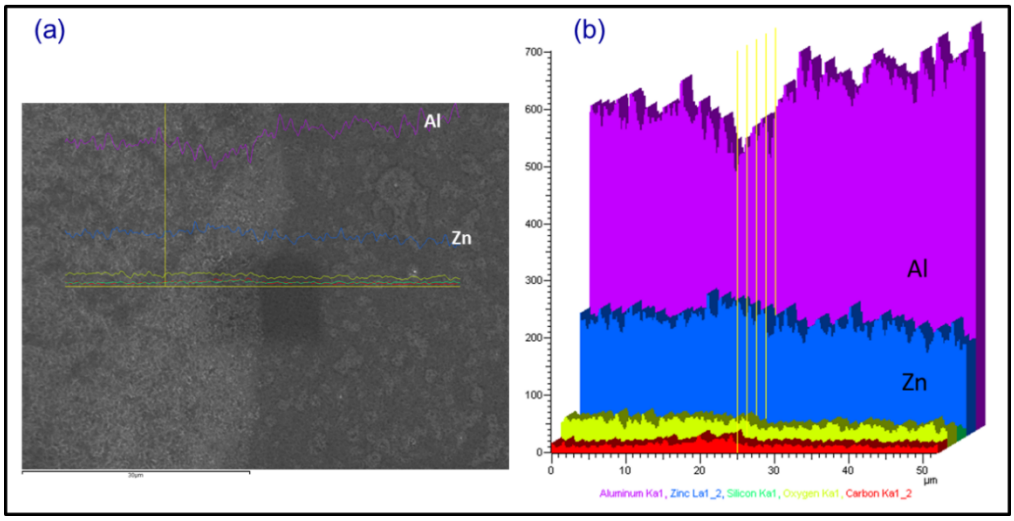

Figure 51. Elemental line analysis on the sample; a) shows the line in analysis and the element curves, b) shows the percentage of each element and the abundance of each in the line in analysis. The Al percentage is much higher than the Zn because of the layer thickness.

The second approach was to carry out the anodization with oxalic acid (30 V for 30min). The zinc again reacted with the acid giving zinc oxalate (C_2O_4Zn) on top of the alumina nanopores (Figure 52). Figure 52 shows the SEM image of the alumina layer with zinc oxalate stone-like structures on top.

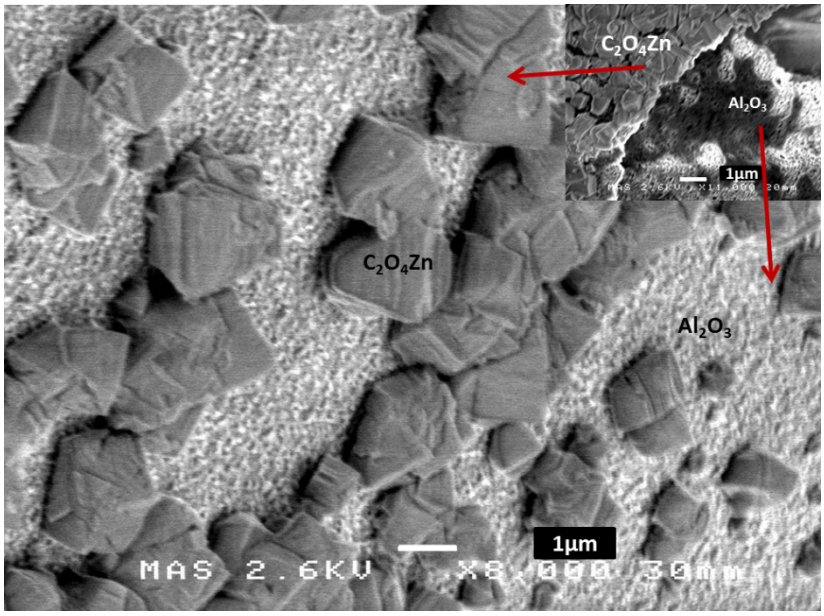

Figure 52. Alumina layer with zinc oxalate stone-like structure on top. The inset at the top right of the picture shows a closer view of the alumina, which is shiny, and the zinc oxalate.

In conclusion, the result of sealing the aluminium layer with zinc again produced perpendicular alumina nanopores to the substrate. Nevertheless, an interesting aspect of making ZnO nanostructures on the top of the alumina nanopores with the same anodization conditions such as the aluminium one when sulphuric acid was observed.

4.1.10. Aluminium with silicon dioxide

One more method was applied in an attempt to achieve the desired result of alumina pores parallel to the substrate. That was to make the surface of the sample rough in order to make the adhesion between the metals stronger. In order to make part of the sample rough where the metal would be deposited, a drop of HF acid was poured on the area for a couple of minutes.

Figure 53 shows the procedure used to make the glass surface rough on a specified area. The method is the same as the one explained in the materials and methods section for making microhills on the glass surface. A photoresist has been applied onto the surface followed by UV-alignment by placing a copper mask this time. This was developed, to leave the desired area exposed for HF treatment. A drop of HF was poured on the exposed area and left for a couple of minutes. After that the sample was thoroughly washed under flowing water for a few minutes and the photoresist was removed with acetone.

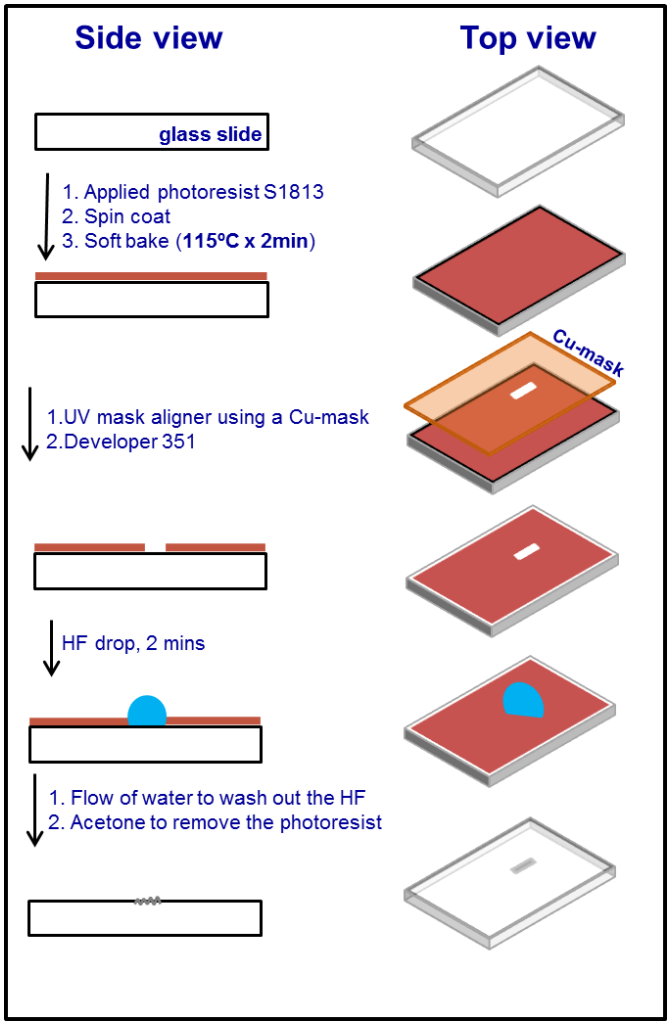

Figure 53. The procedure to roughen the glass surface in a specific area.

The resulting roughened surface can be seen in Figure 54.

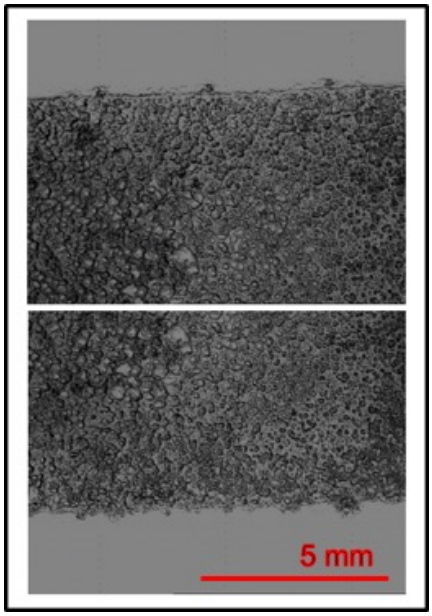

Figure 54. Glass surface after 2 minutes HF treatment, following the procedure shown in Figure 53.

After making the rough surface the usual procedure of making the device was followed as discussed in detail above. The results were not positive.

The anodization (in 0.5 M Sulphuric acid in 20 V for 1 hour) was also perpendicular to the substrate and the sample surface was cracked in many parts. Figure 59 shows the SEM image after the anodization.

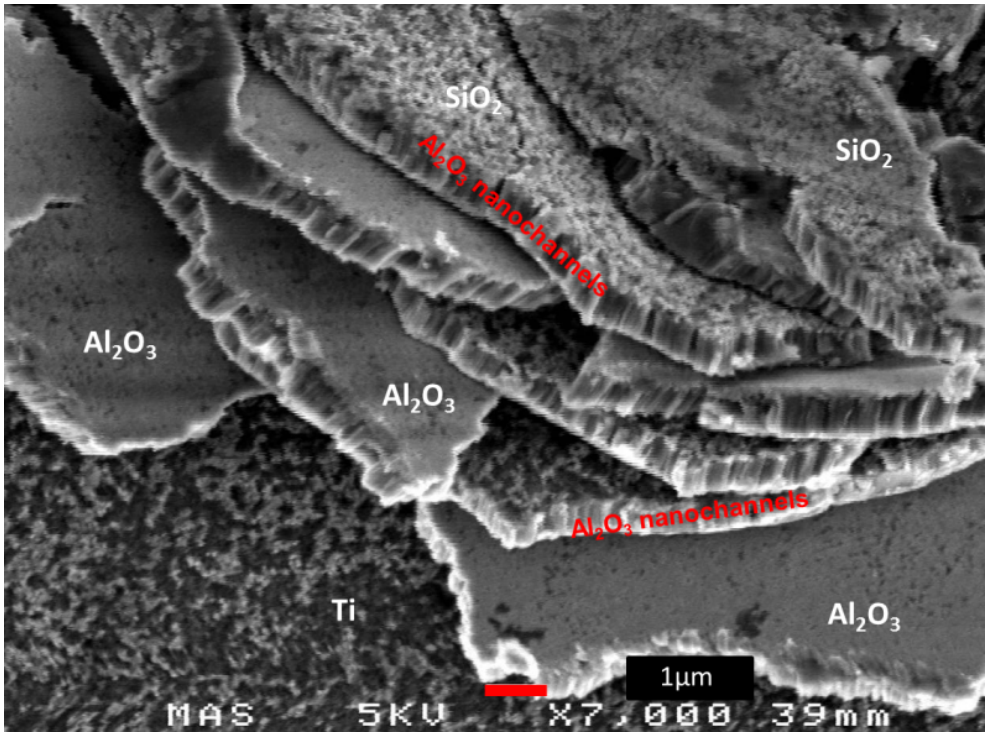

Figure 55. Alumina layers after anodization. The opaque grey with pores is porous alumina, the shiny part with dark on the bottom are SiO_2, and the Ti-dark layer.

4.2 Biomolecular diagnosis

These experiments were carried out by using the same lab-on-a-chip device structure where gold was deposited in place of the aluminium. The lab-on-a-chip with a deposited gold layer was used for biosensing experiments.

4.2.1. Recognition and capture of ochratoxin A

The use of gold in biosensing facilitated the process due to its inert properties during the experiment, giving good interaction and stabilization of the DNA on the gold surface and standing as an electrode in the electrochemical process. In this experiment, the variables used include the voltage, flow rate and the size of the channel between the electrodes. The gold

metal was contained in the lab-on-a-chip. In the methodology section, the method of depositing a 100 nm thick gold layer using a thermal evaporator was fully detailed.

Before using the DNA-aptamer molecule, a primary step was completed, which was to pump a buffer solution inside the microchannel and take CV (Figure 61 blue colour CV1) and EIS (Figure 62 blue colour PB) measurements with the potentiostat as reference. The buffer solution was 0.8 M phosphate buffer (PB) which was prepared by mixing suitable volumes of dipotassium phosphate (K_2HPO_4), potassium phosphate (KH_2PO_4) and sodium chloride (NaCl).

The immobilization of the DNA-aptamer on the gold surface followed, using a DNA chain suitable for recognition and capture of Ochratoxin A, which is: 5'-AAG-ATC-GGG-TGT-GGG-TGG-CGT-AAA-GGG-AGC-ATC-GGA-CA. A syringe was used to pump the solution into the channel (Figure 56).

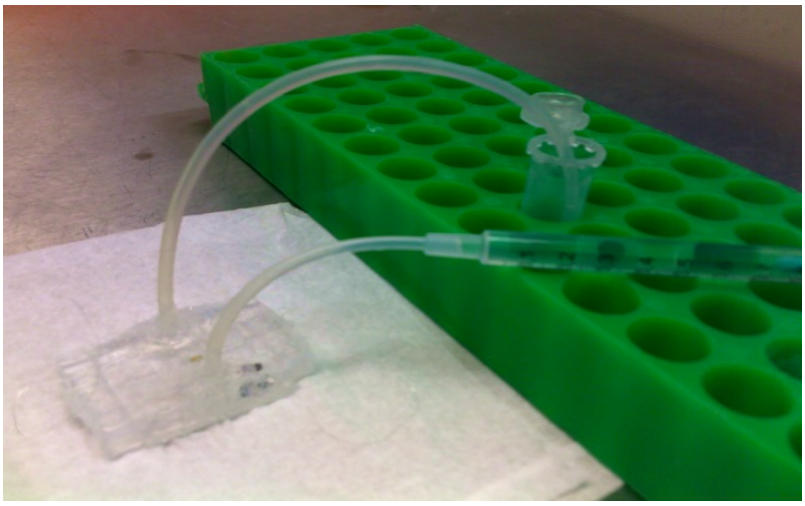

Figure 56. A syringe was used to pump the solution continuously through the microchannel and out to a collection vial.

Once the microchannel of the lab-on-a-chip was filled with DNA, the immobilization buffer was left over night in humid conditions inside the fridge, to give enough time to bind to the gold surface. The following day, the lab-on-a-chip was removed from the fridge and the procedure known as “washing” was carried out by using a decreasing concentration method in order to determine the sensitivity of the biosensor (Yan et al., 2005). All the next steps were carried out at room temperature. The microchannel was rinsed with 1 mM PB in order to remove excess DNA and MCH. This step was repeated using 100 mM PB. In order to remove any excess $MgCl_2$, the microchannel was rinsed with a mix of 10 mM PB and 10 mM EDTA. Finally, to remove any remaining EDTA the microchannel was rinsed with 10 mM PB. After the washing step, 1 mM MCH was pumped inside the microchannel and left for one hour at room temperature under humid conditions in order to fill any remaining spaces between the DNA chains.

After one hour, the microchannel was rinsed with 10 mM PB to wash out any excess MCH. At this stage, the DNA immobilization was complete, and the sample was ready for the first measurements of CV and EIS (Figures 57 red colour CV2 and 58 red colour DNA, respectively). These measurements were compared with the initial run using PB only to observe any changes between the control (without DNA) and with DNA in the microchannel (Figures 57 blue colour CV1 and 58 blue colour PB, respectively). Once the CV and EIS measurements were carried out in the microchannels, ochratoxin A was added, 1 μg per mL was diluted in 200 mL, and left for 30 minutes at room temperature in humid conditions in order to encourage binding. After 30 minutes, the CV and EIS measurements were repeated to compare whether the toxin was captured by the DNA-aptamer or not by giving a different

signal to the first run (Figures 58 green colour CV3 and 63 green colour OTA). Figure 57 shows the cyclic voltammetry graph, where there appears to be no change between the steps CV2 and CV3, i.e. adding DNA-chain and adding ochratoxin A respectively. For this reason, more analyses were completed.

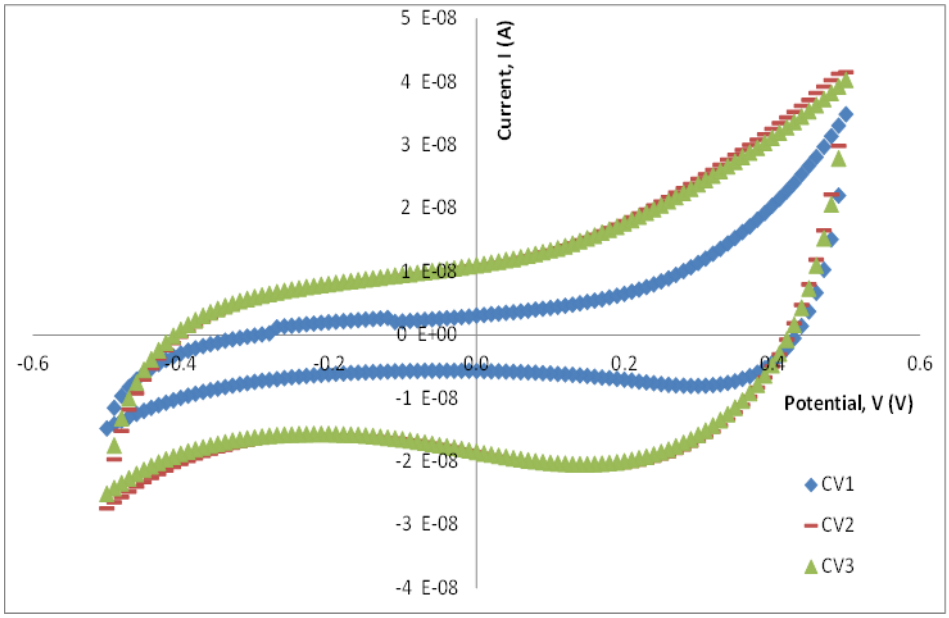

Figure 57. Cyclic voltammetry measurement for the Ochratoxin A: This is the representation of the quantity of the developed electric charge in the electrochemical cell when: (i) only phosphate buffer was in the microchannel across the electrodes, CV1; (ii) the DNA-aptamer was added in the microchannel, CV2; and (iii) when the ochratoxin A was in the microchannel, CV3.

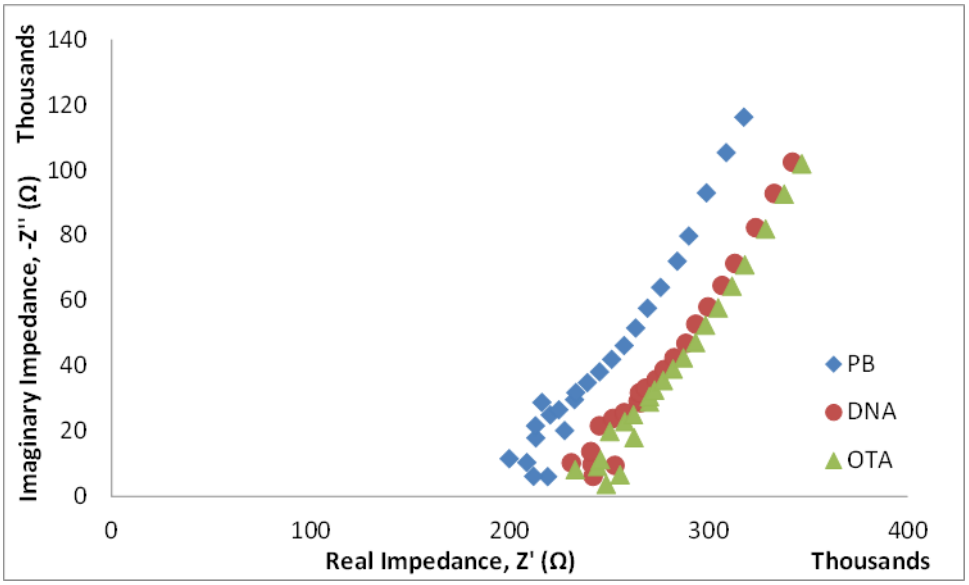

Figure 58. Electrochemical impedance spectroscopy measurements. The blue diamond shape is for phosphate buffer, the red circle shape is for DNA chain and the green triangle is for ochratoxin A.

Figure 58 shows the electrochemical impedance plot, where a shift of the curve between DNA and OTA was observed, when adding a DNA-chain and adding ochratoxin A, respectively.

In addition, other measurements were carried out in order to verify the results; whether or not the DNA-aptamer captured the ochratoxin A. These measurements were the capacitance (Figure 59) and the resistance (Figure 60) both against frequency. Wherein, the different starting position of the curve can be observed by adding each different substances.

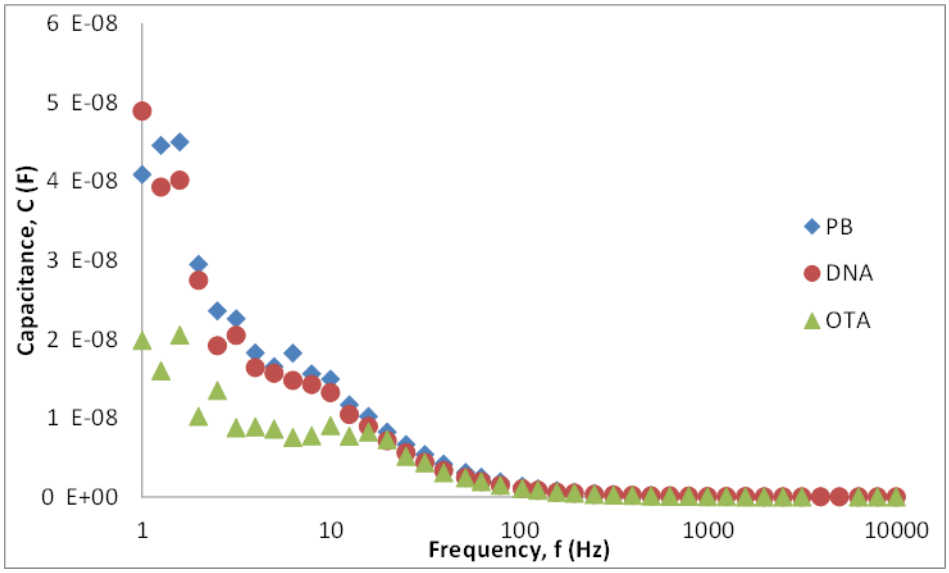

Figure 59. The graph shows the decrease of the capacitance over the range of frequencies tested. The blue diamond data points are for phosphate buffer, the red circles for DNA chain and the green triangles for ochratoxin A. The starting position of the graph changes each time a new substance is inserted.

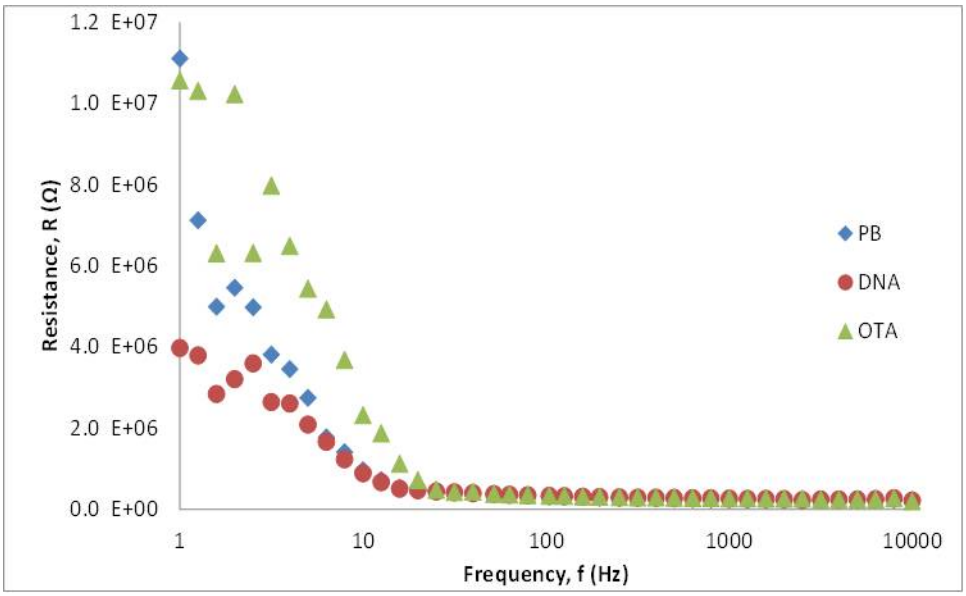

Figure 60. The resistance between the electrodes increases as the frequency increases: The blue diamondsi are data points for phosphate buffer, the red circles for DNA chain and the green triangles for ochratoxin A.

The last two measurements were much more encouraging. The different starting position of the graph can be clearly observed by adding each different substance.

4.2.2. Recognition and capture of α-human thrombin

The next biosensing experiment was carried out to find whether the molecule α-human thrombin could be recognized and captured or not, in the same type of device. The method was similar to the one described above. This time the phosphate buffer step was excluded to avoid any salt sticking on the gold surface. The microchannel was immediately filled with DNA-immobilization buffer and left-over night in humid conditions in the fridge. The DNA-immobilization buffer was composed of: 10 μL DNA-aptamer (100 μM), the sequence used was 5'-T-GG-TGT-GGT-TGG-3'; 987 μL immobilization buffer with magnesium, made in pH 7.3, by 40 mL NaCl (5 M), 20 mL 1 M KH_2PO_4, 140 mL 1 M K_2HPO_4, 100 mL $MgSO_4$ (1 M) and 400 μL EDTA (0.5 M); and 3 μL MCH (1 mM). EDTA 0.5 M and MCH 1 mM were dissolved in phosphate buffer. Phosphate buffer or EIS-buffer for this experiment, in pH 7, was composed of 3.45 mL monobasic KH_2PO_4 (1 M), 6.54 mL dibasic K_2HPO_4 (1 M), 40 mL K_2SO_4 solution (500 mM) and 150.1 mL DI water.

The washing procedure of the microchannel followed, concluding with addition of the α-human thrombin and then starting analyses. The first approach was to fill the microchannel with EDTA 10 mM solution dissolved in the phosphate buffer and leave it for 10 minutes in order to remove the magnesium. After that, the microchannel was rinsed with EIS-buffer to remove any excess EDTA. The back-fill step follows after washing, which was to flow MCH in the microchannel and leave it for precisely one hour in order to fill any remaining unfilled

spaces between DNA-chains. After one hour, the stabilization step follows, which was to flow EIS-buffer in the microchannel and leave it for one hour to remove any MCH chains in excess. At the end of this hour the DNA-chains were linked on to the gold surface and the device was ready to carry out analyses. The first solution added was ferro-/ferri-cyanide solution (5 mM); which was composed of potassium ferrocyonide III ($K_3Fe(CN)_6$ III) 10 mM, and potassium hexacyonoferrate II ($C_6FeK_4N_6.3H_2O$ II) 10 mM, both prepared in EIS buffer, and the EIS measurement was carried out (see Figure 61 BT 1 and 2, circles dark blue and red). Then α-human thrombin solution (500 nM) was added, which contained 1μL thrombin, 426 μL ferro-/ferri-cyanide solution, and the EIS measurement was carried out (see Figure 61 WT1 and 2, triangles blue and pink). Finally, the microchannel was rinsed with ferro-/ferri-cyanide solution and the EIS measurement was carried out to observe whether or not thrombin was bonded with the DNA-aptamer (Figure 61 AT 1 and 2, squares light blue and green).

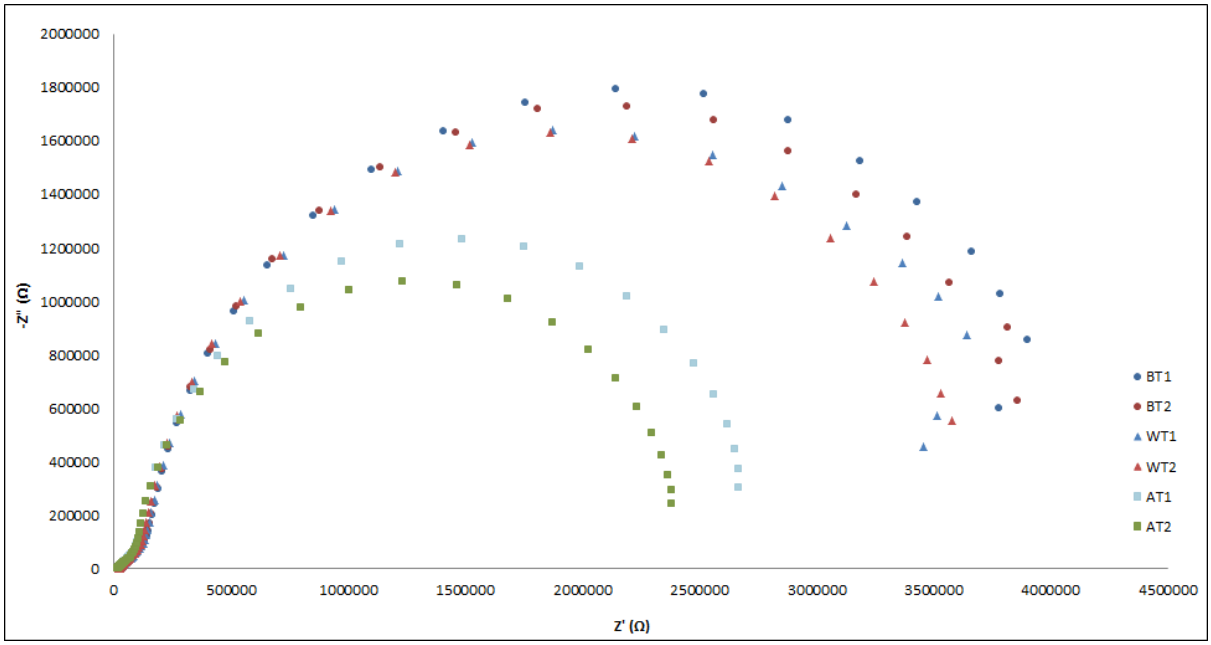

Figure 61. EIS measurements showring the change of the surface properties of the electrode where: BT is before the addition of α-human thrombin in the microchannel, WT is when α-human thrombin has been added in solution in the microchannel and AT is after rinsing off the α-human thrombin.

Regarding the results shown in Figure 61 the most important are the before α-human thrombin measurements and after α-human thrombin, so BT1,2 and AT1,2 respectively. The intermediate step which is with α-human thrombin cannot be taken into consideration because the microchannel is full of the thrombin which can be attached everywhere and can shift to the semi-circle. Thus, after rinsing the excess α-human thrombin it was possible to observe whether or not the thrombin stayed linked to the DNA-aptamer by observing a shift in the curve (Figure 62).

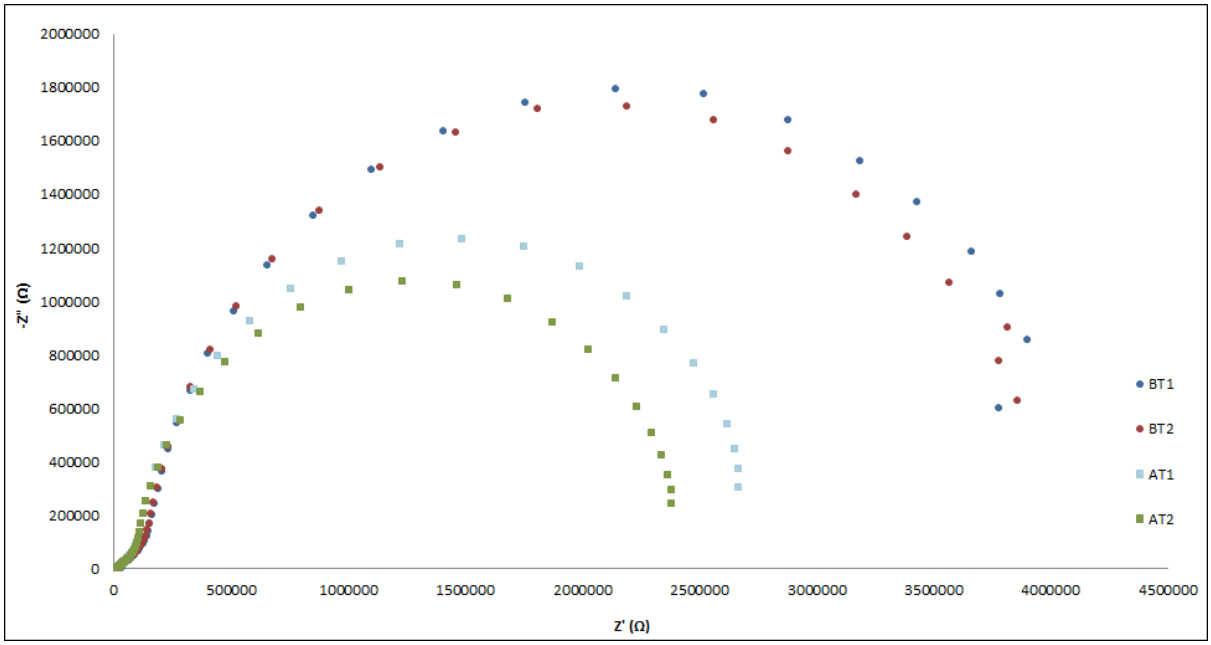

Figure 62. EIS measurement showing the interaction of the analyte with the molecules immobilized on the electrodes surface: BT (before the addition of α-human thrombin in the microchannel) and AT (after rinsing off the excess α-human thrombin). There is a shift of the curve before and after the introduction α-human thrombin, which represents the change of the surface properties of the electrode.

There is a clear curve shift before and after the addition of α-human thrombin in the chip. These results using a two-electrode system look very promising but not as expected. The expected curve based on literature is the curve showing the DNA-chain bonded with the α-human thrombin higher than the curve showing the DNA-chain only (Keighley et al., 2008). At this point, an interesting step forward was to improve the device and repeat the experiment. As the experiment gives a clear curve shift it was very reasonable to try again in order to achieve results comparable with the literature that could be characterized as more reliable. The optimization of the device involved transforming it into a three-electrode cell

set-up instead of the two-electrode cell. The new design of the device is demonstrated in Figure 63.

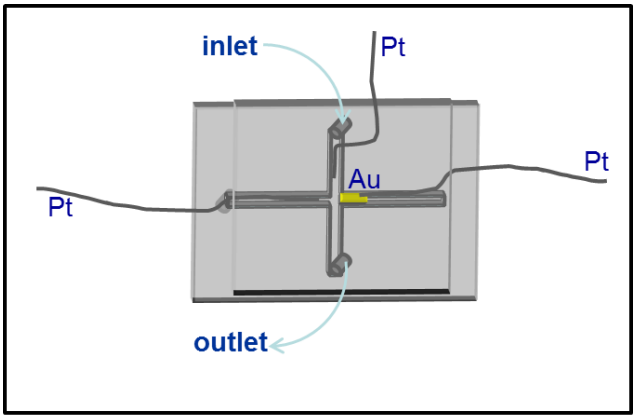

Figure 63. Three electrode cell set-up of the device, consists of a working gold electrode, a counter and a reference platinum electrode.

Figure 63 shows the device with one more electrode on the side of the inlet, which is the reference electrode. The working electrode is the gold layer and the counter electrode is the platinum opposite the gold. Furthermore, Figure 64a shows the device connected to the outlet of the potentiostat and tubes connected to a Cole-Palmer peristaltic pump. Figure 64b shows the distribution of the three-electrode system and shows where the current and the voltage were measured.

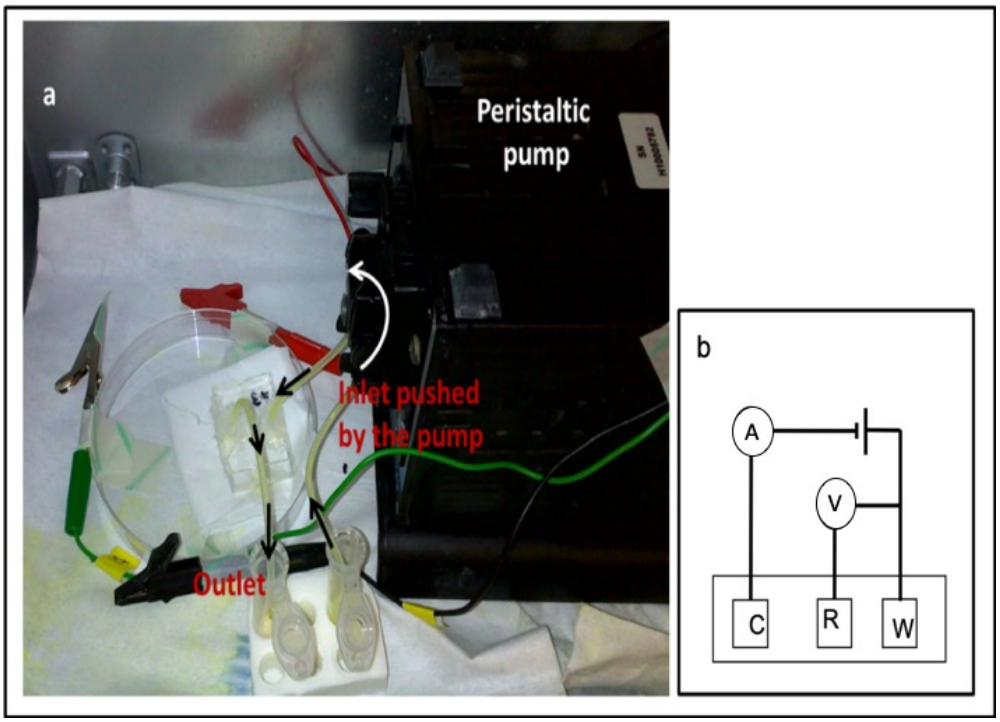

Figure 64. The three-electrode cell set-up is presented; a) as it is used in the laboratory, connected to a peristaltic pump which pumped the solvents in the microchannel and b) the set-up system showing how the voltage and current were measured.

The whole procedure to immobilize the DNA-chain on the gold surface and the α-human thrombin flow was kept exactly the same as for the two-electrode cell set up. However, one further step was added at the end, the removal of the thrombin with NaCl: A solution of 2 M NaCl was injected inside the microchannel after rinsing the α-human thrombin off and kept for about 10 minutes. Then EIS-buffer was added and left for 1 hour. After an hour time, the ferro-/ferri-cyanide solution was flowed inside the microchannel and EIS measurements were carried out. This step should shift the curve back to the starting point i.e. before the α-human thrombin one.

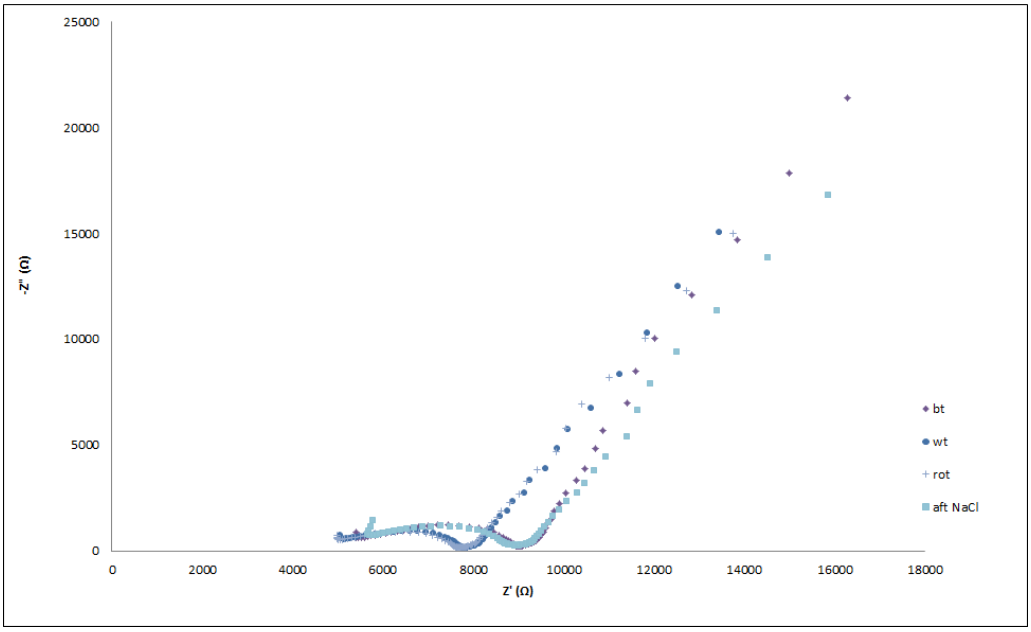

Figure 65. EIS measurements: the measurement starts with the buffer solution, bt. Then, the a-human thrombin is in the microchannel; and the change of the surface properties of the electrode change resulting in a shift of the curve, wt. Rinsing off α-human thrombin, the change of the surface properties of the electrode change. The next step was to add NaCl and remove the thrombin. The graph's curve goes back the initial stage, bt.

Indeed, as it can be seen in the graph in Figure 65, the purple diamond, bt, and the light blue square, aft NaCl, are in the same place, which represent the measurement before adding the α-human thrombin and after the removal of the α-human thrombin. The remaining curves wt, blue circle, and rot, light blue cross, are in the same place and present the step when the α-human thrombin was added to the channel and the step when the channel was rinsed off with ferro-/ferri-cyanide solution.

At this stage the result shows clearly that the device works as planned. The curves fall exactly at the expected place in Figure 65, but with one only unexpected parameter which

was the different initial values. The initial value is the resistance of the solution and this has changed from curve to curve in the same experiment, which means the applied force in between the electrodes was high. Considering this, one more improvement had to be made in order to show for certain that this method works. Based on literature, this was to change the material of the electrodes, which means keeping the counter electrode as platinum, the working electrode as gold and the reference was changed to silver (Estrela et al., 2005).

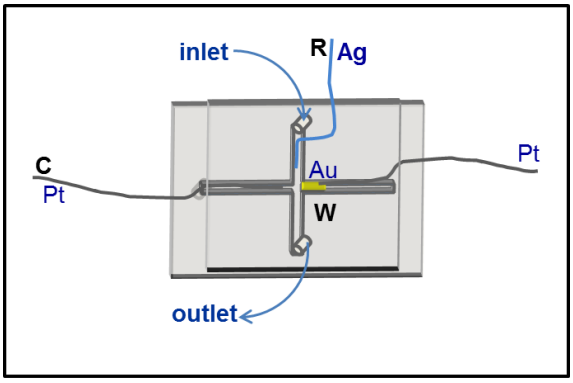

Figure 66. Three-electrode cell set up with electrodes: gold (Au) as working, platinum (Pt) as counter and silver (Ag) as reference.

This new design shown in Figure 66 gave more reliable results, as it can be seen from the EIS measurements in Figure 67. Figure 67 shows the EIS measurements before thrombin, bt, (Figure 67 green diamond), with thrombin, wt, (Figure 67 red circle), rinsing off the thrombin, rot, (Figure 67 purple square) and when the thrombin is removed with NaCl, aft NaCl, (Figure 67 yellow triangle). The measurement bt and aft NaCl are in the same place, which means that thrombin was attached to the DNA chain and when it was removed the

signal of the curve went back to the starting point (i.e. before thrombin). At this stage the device was fully optimized and the results reliable.

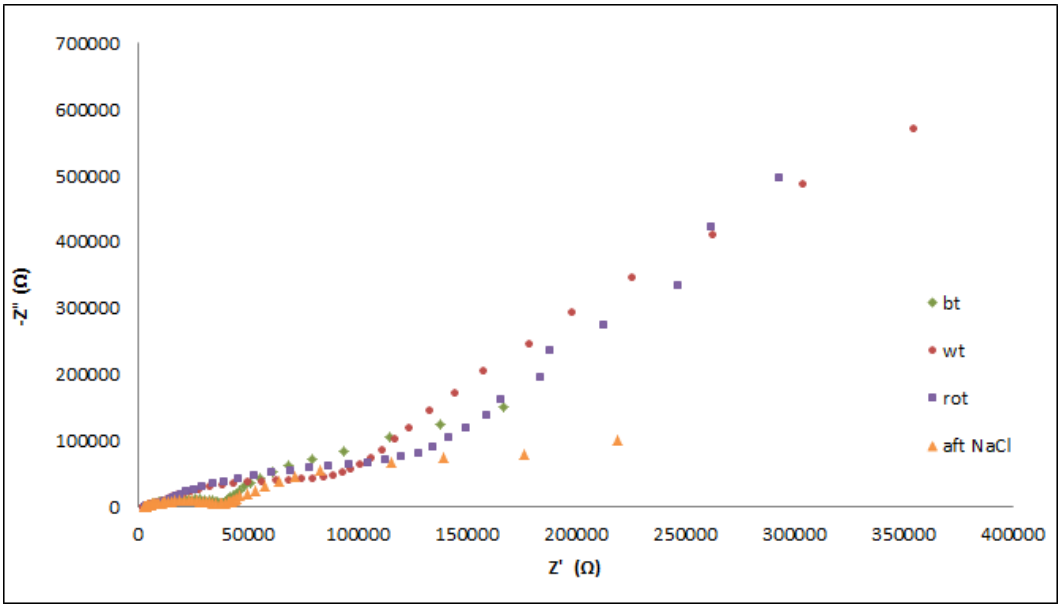

Figure 67. EIS measurements of α-human thrombin in a three-electrode cell set-up with electrodes gold (Au) as working, platinum (Pt) as counter and silver (Ag) as reference (see Figure 71), and where: bt is the measurement before to add the thrombin, wt is when thrombin is added in the microchannel, rot is when the thrombin was rinsed off and aft NaCl is when the thrombin was removed by using NaCl.

Even though the results were exactly as expected, further analyses were carried out to prove the full reliability of the results. Figure 68 shows the capacitance measurements before thrombin, bt, (Figure 68 red line 3rd measurement), with thrombin, wt, (Figure 68 green line 3rd measurement), rinsing off the thrombin, rot, (Figure 68 orange line 3rd measurement). The measurement wt and rof are in the same place, which means that the thrombin was attached

to the DNA chain and was not removed after rinsing off the channel. The signal of the curve stayed in exactly the same place.

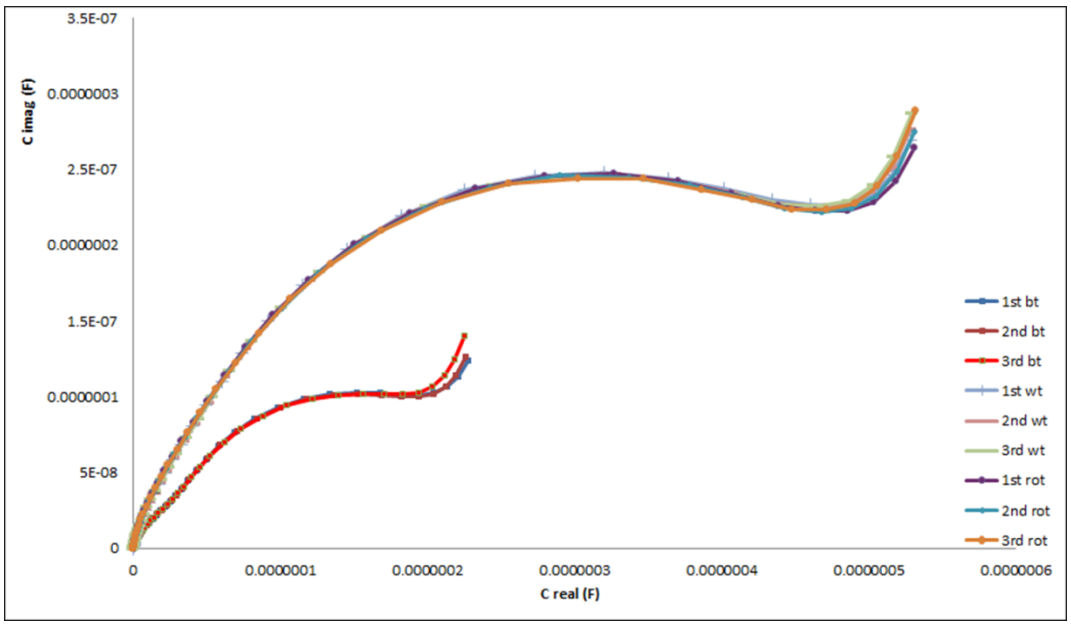

Figure 68. Capacitance measurements of α-human thrombin in a 3-electrode cell set-up with electrodes gold (Au) as working, platinum (Pt) as counter and silver (Ag) as reference, and where: bt is the measurement before to add the thrombin, wt is when thrombin is added in the microchannel, rot is when the thrombin was rinsed off and aft NaCl is when the thrombin was removed by using NaCl. Each measurement was repeated 3 times in order to make sure that the signal does not change over the time.

In conclusion, the biosensing devise through a number of optimization steps has now been thoroughly optimized and gave the desired and expected results.

4.2.3. Discussion

The entire experiment revolved around the interaction of ions in the electrolysis process. In this case, the buffer acted as the electrolyte. The completion of a circuit created a potential difference between the negative electrode and the positive electrode.

The DNA strands are negatively charged. DNA strands were repelled by the negatively charged polyelectrolyte multilayer (PEM) surface and attracted towards the positively charged gold electrode. The DNA strands bind via thiol bond to the positive electrode thus increasing the amount of current in the circuit. The DNA strands were deposited on the surface of the gold electrode where the continued deposition increased the amount of electric current in the circuit. However, the process ended when the entire surface of the gold electrode was fully covered meaning that no more surface was left for the contact between the gold electrode and immobilization buffer.

The buffer solution containing DNA molecules was conducted in two phases. Phase one involved running the buffer in the absence of the DNA molecules. The graphs show that the buffer alone did not alter the magnitude of the current flowing through the circuit. However, when the DNA molecules were pumped into the immobilization buffer, the Ammeter deflection increased continuously until a point where the deflection stopped.

4.3 Oxygen Plasma Equipment Fabrication

While the oxygen plasma experiments were performing, oxygen plasma equipment was attempted to be fabricated. The way to change the hydrophobic behaviour of both surfaces, glass and PDMS, is to enrich them with oxygen but with lower plasma power. An oxygen

plasma equipment fabrication was engineered. A fully sealed chamber to produce inductively coupled plasma using a coil rounded to a tube. With the help of Master student Long Ding, supervised by Dr. Pedro Estrela, an inductively coupled plasma chamber was engineered. It was a type of plasma source in which the energy was applied with electric current which was produced by electromagnetic induction. This equipment is similar to (but simplified) the ICP equipment mentioned before, but in this equipment the electromagnetic field is uniformly made around the chamber. By varying the time the magnetic field becomes stronger. Figure 69 shows the engineered plasma chamber.

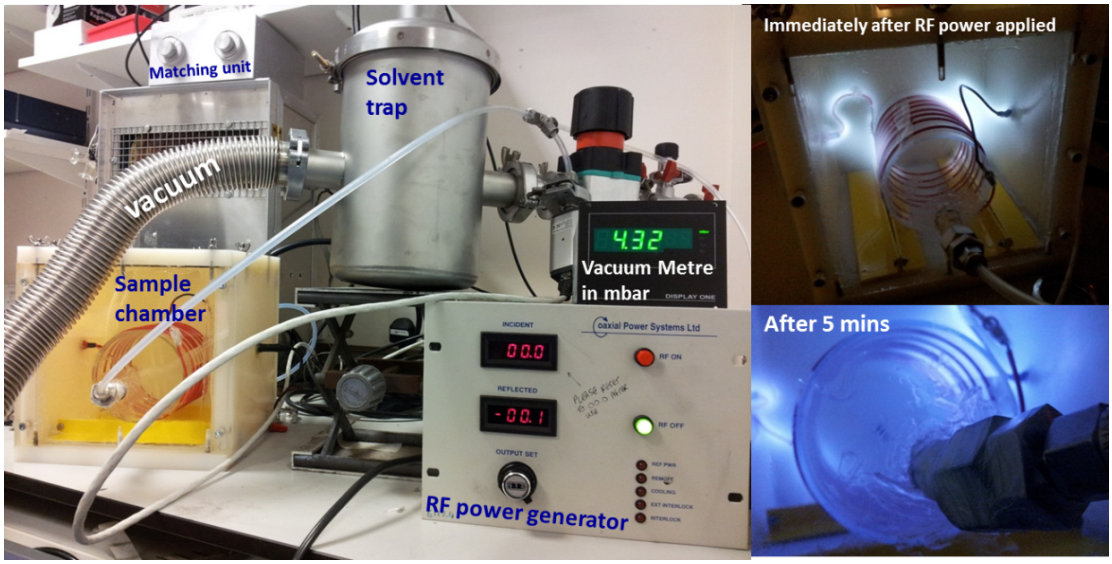

Figure 69. The sample chamber fabricated in the lab can be seen here. It is connected to a vacuum pump, a solvent trap, a vacuum gauge and a power generator. Once the vacuum is under 10^{-2} mbar a radio frequency (RF) power is applied and immediately plasma produced around the rounded coil; after 5 minutes, the plasma is extended to the entire chamber.

Figure 69 shows that after applying the RF power, plasma was generated initially only around the coil, but after 5 minutes the plasma spread everywhere in the chamber. The quality

of the plasma, which is essential to have a uniform surface functionalisation of the substrates was assessed via it colour, with an initial blueish tinge transforming in a deep blue one, which shows a very clean and fully vacuumed chamber.

5. Conclusions

The aim of this research work was to design a common device architecture that could be used to carry out different experiments in nature. The device was firstly designed and fabricated through a series of different optimization steps. A crucial step, namely the type of metal deposited, determined the device experimental type: A lab-on-a-chip microfluidic device or a biosensor microfluidic device. The main metals used in this work were aluminium and gold, respectively.

The aluminium metal was deposited inside the microchannel and then anodized to form alumina. Aluminium anodization can give controllable shape, size and charge of alumina pores based on the electrochemical anodization parameters applied such as acid type and concentration and applied voltage. Based on the initial knowledge of the anodization process, the alumina nanochannels were supposed to form parallel to the microchannel, to be used for biomolecule separation based on shape, diameter and charge of the pores. This plan was not achieved fully: Although the aluminium anodization was performed successfully inside the microchannel, the formed alumina nanochannels were perpendicular to the microchannel, rather than parallel. This can be explained in terms of energy minimisation, with the perpendicular orientation opposing less resistance to the electrochemical process than the

parallel one. Even though the results were not the expected ones they were still considered useful for the formation of lab-on-a-chip devices and further attempts at optimizing the structure were done: A second metal was deposited on top of the metal to prevent the top aluminium surface from oxidizing when it came into contact with the atmospheric air. This experiment was repeated with different metals such as titanium and zinc and gave interesting results which could be the base for future research and analysis in future work.

Gold was deposited inside the lab-on-a-chip device and biosensing experiments were performed. This device can be used for test analysis on samples to prove whether the analyte contains a specific biomolecule. As a model experiment, a DNA aptamer was immobilized on the gold surface. The gold metal was carefully chosen to be used in these experiments due to the properties; its ability to attract the DNA aptamer and act as an electrode during the electrochemical experiment and being inert throughout the experiment. Two different biosensing experiments were performed with successful results, both experiments involving the recognition and capture of the "target biomolecule". The two biomolecules were a toxin and a thrombin, namely ochratoxin A and α-human thrombin. The experiments in both cases consisted of three standard steps, namely buffer flow in the channel, followed by DNA aptamer addition and finally the addition of the target molecule. Each step was investigated via impedimetric and voltammetric measurements. Curve shifts demonstrated the different state of the solution. When the ochratoxin A was the target the whole plot shifted further and the presence of the toxin in the analyte was observed. The second target was α-human thrombin. The very first experimental attempt using the device gave positive results. However, the impedimetric and voltammetric measurements returned as lower reference curve compared to the literature. This was attributed to the fact that the present device had a

two-electrode cell compared with three-electrode cells used in the literature. The device has gone through a series of optimization steps due to promising results and each time the results were improved. These optimization steps were conducted to give a strong, more reliable and repeatable result. A biosensor device was successfully fabricated for the recognition and capture of α-human thrombin. In addition, it can be reusable, as it was possible to fully wash away the α-human thrombin as the curves went back to their initial point. Therefore, the gold-based biosensor device can be cost effective.

6. Future work

Based on the results presented in this thesis, the future work could include the development of a multiple channel DNA-template device for multiple analysis in parallel. The device could be kept in a humid environment to allow the DNA-template to be fresh and ready for use. Preservatives are not necessary due to the strong interaction between the DNA strands and gold metal. In addition, after the completion of these investigations the device can be reused by washing off all the analyte.

The device could also be used as a PCR microfluidic device. The polymerase chain reaction (PCR) refers to a repeatable temperature cycles that plays a significant role in the amplification of nucleic acid. The PCR array-on-chip replicates small nucleic acid samples into huge quantities. The PCR process consists of three thermal cycle steps that promote the replication process; namely heating of samples to temperatures between 90 and 95 °C (denaturation), cooling of samples to temperatures of 50 °C (annealing) and warming the samples slightly to temperatures between 60 and 70 °C (elongation) (Zhang et al., 2006).

Although PCR include the three-time zones, the progress of the cycle on a chip would not depend on the normal PCR cycle time. This is due to the small size of the PCR microfluidic chip allowing them to handle small volumes of liquids.

Appendices

Appendix 1

Publication

Sofia Bekou and Davide Mattia, **Wetting of Nanotubes**, *Current Opinion in Colloid and Interface Science*, Vol. 16, Issue 4, August 2011, Pages 259-265

Conferences & Workshops

22-24/03/2010, *Principal and Applications of Micro- and Nanofluidics at the Center of Smart Interfaces*, TU Darmstadt, Short Course in Technische Universität Darmstadt, Germany

06/08/2012, *International Mini Symposium on Sensing and Drug Delivery Systems (SDDS12)*, University of Bath

22-25/11/2012, *Essentials in Microscopy*, Olympus KeyMed, Southend-on-Sea, Certificate of attendance and knowledge taken

09/11/2013, *Microscopy and Analysis Conference 2013*, University of Bath, First poster price awarded

Appendix 2

Cleanroom definition

The whole photolithographic procedure took place in a room without windows and under yellow light which completely blocked all radiation with wavelength less than 500 nm, because the photoresist is photosensitive and can degrade in white light; usually this room is called cleanroom. The cleanroom is a special and appropriate laboratory in which all the nanofabrication techniques take place. The cleanroom is given its name because it has a low level of environmental pollutants such as dust, which is a critical condition for making nanodevices.

Appendix 3

Calculations for Nernst equation

Nernst equation under non-standard conditions:

$$\boldsymbol{E = E^{\circ}_{\,reduction} - E^{\circ}_{oxidization}} \quad \textbf{[9]}$$

Where, E is the electrode potential and E^{o} in the standard electrode potential.

When, E^{o} in positive the reaction is spontaneous.

E^{o} is negative the reaction is not spontaneous.

The Gibbs free energy (ΔG) involves the electrode potential and the spontaneity of the reaction:

$$\Delta G = -nFE \quad [\,10\,]$$

Where, *n* is the number of the electrons transferred in the reaction and *F* is the Faraday constant 96485 C/mol. Under standard conditions this equation becomes:

$$\Delta G^o = -nFE^o \quad [\,11\,]$$

Since, $$\Delta G = \Delta G^o - RTlnQ \quad [\,12\,]$$

Where *Q* in reaction quotient: $$\boldsymbol{Q = \frac{Concentration\ of\ products}{concentration\ of\ reactants}} \quad [13\,]$$

Substituting Eq. 7 and 8 to Eq. 9: $$-nFE = -nFE^o - RTlnQ \quad [\,14\,]$$

Divided both sides of the equation with – *nF*: $$\boldsymbol{E = E^o + \frac{RT}{nF}\,lnQ} \quad [\,15\,]$$

Calculation for electrochemical impedance spectroscopy and cyclic voltammetry

Impedance can be calculated as: $$\mathbf{z = z_{real} + iz_{imaginary}} \quad [\,16\,]$$

Where is $$\boldsymbol{z = \frac{1}{iwC} + R} \quad [\,17\,]$$

But, $\boldsymbol{i = \sqrt{-1}}$, so $\frac{1}{i}$ found in eq. 14 can be: $$\frac{1}{i} \times \frac{i}{i} = \frac{i}{i^2} = \frac{i}{-1} = -i \quad [\,18\,]$$

Substituting eq. 15 to 14: $$\boldsymbol{z = R - i\,\frac{1}{wC}} \quad [\,19\,]$$

Where **C** is the **capacitance**, which can be calculated as: $$\boldsymbol{C = \frac{-1}{\omega z''}} \quad [\,20\,]$$

and where **ω** is the angular **frequency**, which can be calculated as: $$\boldsymbol{\omega = 2\pi f} \quad [\,21\,]$$

Taking in consideration *C, R* and $|z|$ as:

$$\boldsymbol{C = \frac{-z}{\omega|z|^2} = -\frac{z''}{\omega(z'^2 + z''^2)}} \quad [\,22\,]$$

$$\boldsymbol{R = \frac{|z|^2}{z'} = \frac{z'^2+z''^2}{z'}} \quad \textbf{[23]}$$

$$\boldsymbol{|z| = \sqrt{z'^2 + z''^2}} \quad \textbf{[24]}$$

Substituting eqs. 20 and 21 to 19, the **capacitance** become: $\boldsymbol{C = \frac{-z''}{2\pi f(z'^2+z''^2)}}$ **[25]**

7. References

ADAMS, J. D., THÉVOZ, P., BRUUS, H. & SOH, H. T. 2009. Integrated acoustic and magnetic separation in microfluidic channels. *Applied Physics Letters,* 95**,** 254103.

AHMED, T. 2001. *Reservoir Engineering Handbook*, Elsevier.

ALI, M. A., SRIVASTAVA, S., SOLANKI, P. R., REDDY, V., AGRAWAL, V. V., KIM, C., JOHN, R. & MALHOTRA, B. D. 2013. Highly efficient bienzyme functionalized nanocomposite-based microfluidics biosensor platform for biomedical application. *Scientific Reports,* 3.

BAHADORIMEHR, A. & MAJLIS, B. Y. 2011. Fabrication of glass-based microfluidic devices with photoresist as mask. *Informacije MIDEM,* 41**,** 193-196.

BANGE, A., HALSALL, H. B. & HEINEMAN, W. R. 2005. Microfluidic immunosensor systems. *Biosensors and Bioelectronics,* 20**,** 2488-2503.

BASSOUS, E., TAUB, H. & KUHN, L. 1977. Ink jet printing nozzle arrays etched in silicon. *Applied Physics Letters,* 31**,** 135-137.

BECKER, F. F., WANG, X. B., HUANG, Y., PETHIG, R., VYKOUKAL, J. & GASCOYNE, P. R. C. 1995. Separation of human breast cancer cells from blood by differential dielectric affinity. *Proceedings of the National Academy of Sciences of the United States of America,* 92**,** 860-864.

BEECH, J. 2011. *Microfluidics Separation and Analysis of Biological Particles.* Lund University

BEKOU, S. & MATTIA, D. 2011. Wetting of nanotubes. *Current Opinion in Colloid & Interface Science,* 16**,** 259-265.

BERSCHEID, G., GRÖTSCH, H., NEUBAUER, H., PÜNTER, J., REINDL, J. & SEIPP, P. 1992. Determination of rDNA hirudin and a-human thrombin-hirudin complex in plasma samples: enzyme linked immunosorbent assays for hirudin and complex vs. chromogenic thrombin substrate assay. *Thrombosis research,* 66**,** 33-42.

BIZET, K., GABRIELLI, C. & PERROT, H., 1999. Biosensors based on piezolectric transducers. Analusis, 27(7), pp.609-616

BONNER, W. A., HULETT, H. R., SWEET, R. G. & HERZENBERG, L. A. 1972. Fluorescence Activated Cell Sorting. *Review of Scientific Instruments,* 43**,** 404-409.

BRATTON, D., YANG, D., DAI, J. Y. & OBER, C. K. 2006. Recent progress in high resolution lithography. *Polym. Adv. Technol***,** 17, 94–103.

BREVNOV, D. A., BARELA, M. J., BROOKS, M. J., LÓPEZ, G. P. & ATANASSOV, P. B. 2004. Fabrication of anisotropic super hydrophobic/hydrophilic nanoporous membranes by plasma polymerization of C4F8 on anodic aluminium oxide. *Journal of the Electrochemical Society,* 151**,** B484-B489.

BUSTILLO, J. M., HOWE, R. T. & MULLER, R. S. 1998. Surface micromachining for microelectromechanical systems. *Proceedings of the IEEE,* 86**,** 1552-1574.

BUTENAS, S., VAN'T VEER, C. & MANN, K. G. 1999. "Normal" Thrombin Generation. *Presented in part at the XVIth Congress of the International Society on Thrombosis and Haemostasis, June 6-12, 1997, Florence, Italy (abstr PS-1653), at the 15th International Congress on Thrombosis, October 16-21, 1998, Antalya, Turkey (abstr 234), and at the 40th Annual Meeting of the American Society of Hematology, December 4-8, 1998, Miami Beach, FL (abstr 151).* 94**,** 2169-2178.

BYRNE, B., STACK, E., GILMARTIN, N. & O'KENNEDY, R. 2009. Antibody-based sensors: Principles, problems and potential for detection of pathogens and associated toxins. *Sensors,* 9**,** 4407-4445.

CAO, Z., TONG, R., MISHRA, A., XU, W., WONG, G. C. L., CHENG, J. & LU, Y. 2009. Reversible Cell-Specific Drug Delivery with Aptamer-Functionalized Liposomes. *Angewandte Chemie International Edition,* 48**,** 6494-6498.

CASH JR, W.C., 2000. Focused X Rays. X-ray collimator for lithography. U.S. Patent 6,049,588.

CHEN, W., WU, J.-S. & XIA, X.-H. 2008. Porous Anodic Alumina with Continuously Manipulated Pore/Cell Size. *ACS Nano,* 2**,** 959-965.

CHOI, K., NG, A. H. C., FOBEL, R. & WHEELER, A. R. 2012. Digital microfluidics. *Annual Review of Analytical Chemistry.*

CHOI, K., NG, A.H., FOBEL, R. & WHEELER, A.R., 2012. Digital microfluidics. Annual review of analytical chemistry, 5, pp.413-440.

CHU, S. Z., INOUE, S., WADA, K., HISHITA, S. & KUMSHIMA, K. 2005. Self-organized nanoporous anodic titania films and ordered titania nanodots/nanorods on glass. *Advanced Functional Materials,* 15**,** 1343-1349.

CHURCH, C., ZHU, J., NIETO, J., KETEN, G., IBARRA, E. & XUAN, X. 2010. Continuous particle separation in a serpentine microchannel via negative and positive dielectrophoretic focusing. *Journal of Micromechanics and Microengineering,* 20**,** 065011.

CROWLEY, T. A. & PIZZICONI, V. 2005. Isolation of plasma from whole blood using planar microfilters for lab-on-a-chip applications. *Lab on a Chip,* 5**,** 922-929.

DAINTITH, J. 2008. *Dictionary of Chemistry*, Oxford University Press.

DARWISH, I. A. 2006. Immunoassay methods and their applications in pharmaceutical analysis: basic methodology and recent advances. *Int J Biomed Sci,* 2**,** 217-235.

DAW, R. & FINKELSTEIN, J. 2006. Lab on a chip. *Nature,* 442**,** 367-367.

DEMEKE, T. & JENKINS, G. R. 2010. Influence of DNA extraction methods, PCR inhibitors and quantification methods on real-time PCR assay of biotechnology-derived traits. *Analytical and bioanalytical chemistry,* 396**,** 1977-1990.

DEUBEL, M., VON FREYMANN, G., WEGENER, M., PEREIRA, S., BUSCH, K. & SOUKOULIS, C. M. 2004. Direct laser writing of three-dimensional photonic-crystal templates for telecommunications. *Nature Materials,* 3**,** 444-447.

DI CARLO, D., EDD, J. F., IRIMIA, D., TOMPKINS, R. G. & TONER, M. 2008. Equilibrium separation and filtration of particles using differential inertial focusing. *Analytical Chemistry,* 80**,** 2204-2211.

DIDAR, T. F. & TABRIZIAN, M. 2010. Adhesion based detection, sorting and enrichment of cells in microfluidic Lab-on-Chip devices. *Lab on a Chip,* 10**,** 3043-3053.

DITTRICH, P. S. & MANZ, A. 2006a. Lab-on-a-chip: microfluidics in drug discovery. *Nat Rev Drug Discov,* 5**,** 210-218.

DITTRICH, P. S. & MANZ, A. 2006b. Laser processing for bio-microfluidics applications (part II). *Anal.Bioanal. Chem***,** 385, 1362–1369.

DOH, I. & CHO, Y.-H. 2005. A continuous cell separation chip using hydrodynamic dielectrophoresis (DEP) process. *Sensors and Actuators A: Physical,* 121**,** 59-65.

DRUMMOND, T. G., HILL, M. G. & BARTON, J. K. 2003. Electrochemical DNA sensors. *Nature Biotechnology,* 21**,** 1192.

EDDINGS, M. A., JOHNSON, M. A. & GALE, B. K. 2008. Determining the optimal PDMS–PDMS bonding technique for microfluidic devices. *Journal of Micromechanics and Microengineering,* 18**,** 067001.

ELAM, J. W., ROUTKEVITCH, D., MARDILOVICH, P. P. & GEORGE, S. M. 2003. Conformal Coating on Ultrahigh-Aspect-Ratio Nanopores of Anodic Alumina by Atomic Layer Deposition. *Chemistry of Materials,* 15**,** 3507-3517.

ESTRELA, P., MIGLIORATO, P., TAKIGUCHI, H., FUKUSHIMA, H. & NEBASHI, S. 2005. Electrical detection of biomolecular interactions with metal–insulator–semiconductor diodes. *Biosensors and Bioelectronics,* 20**,** 1580-1586.

FUJII, T. 2002. PDMS-based microfluidic devices for biomedical applications. *Microelectronic Engineering,* 61–62**,** 907-914.

GESCHKE, O., KLANK, H. & TELLEMAN, P. 2004. *Microsystem Engineering of Lab-on-a-Chip Devices*, Wiley-VCH Verlag GmbH & Co. KGaA.

GOLBERG, A., LINSHIZ, G., KRAVETS, I., STAWSKI, N., HILLSON, N. J., YARMUSH, M. L., MARKS, R. S. & KONRY, T. 2014. Cloud-enabled microscopy and droplet microfluidic platform for specific detection of Escherichia coli in water. *PloS one,* 9**,** e86341.

GOMEZ, F. A. 2008. *Biological applications of microfluidics*, John Wiley & Sons.

GONG, D., GRIMES, C. A., VARGHESE, O. K., HU, W., SINGH, R., CHEN, Z. & DICKEY, E. C. 2001. Titanium oxide nanotube arrays prepared by anodic oxidation. *Journal of Materials Research,* 16**,** 3331-3334.

GOSSETT, D. R., WEAVER, W. M., MACH, A. J., HUR, S. C., TSE, H. T. K., LEE, W., AMINI, H. & DI CARLO, D. 2010. Label-free cell separation and sorting in microfluidic systems. *Analytical and Bioanalytical Chemistry,* 397**,** 3249-3267.

H.A. STONE, A.D. STROOCK, A. & AJDARI, A. 2004. ENGINEERING FLOWS IN SMALL DEVICES. *Annual Review of Fluid Mechanics,* 36**,** 381-411.

HARALDSSON, K. T. 2005. *Fabrication of polymeric microfluidic devices via photocurable liquid monomers* (Doctoral dissertation, KTH).

HARRISON, D. J., FLURI, K., SEILER, K., FAN, Z., EFFENHAUSER, C. S. & MANZ, A. 1993. Micromachining a miniaturized capillary electrophoresis-based chemical analysis system on a chip. *Science,* 261**,** 895-897.

HNATOVSKY, C., TAYLOR, R., SIMOVA, E., RAJEEV, P., RAYNER, D., BHARDWAJ, V. & CORKUM, P. 2006. Fabrication of microchannels in glass using focused femtosecond laser radiation and selective chemical etching. *Applied Physics A,* 84**,** 47-61.

HU, L., BIAN, Z., LI, H., HAN, S., YUAN, Y., GAO, L. & XU, G. 2009. [Ru (bpy) 2dppz] 2+ electrochemiluminescence switch and its applications for DNA interaction study and label-free ATP aptasensor. *Analytical chemistry,* 81**,** 9807-9811.

HUANG, H. & ZHU, J.-J. 2009. DNA aptamer-based QDs electrochemiluminescence biosensor for the detection of thrombin. *Biosensors and Bioelectronics,* 25**,** 927-930.

ISAACS, A., DAINTITH, J., MARTIN, E., 2006, Dictionary of science, , fourth edition, Oxford University press Inc, New York.

ISSADORE, D. & WESTERVELT, R. M. 2013. *Point-of-Care Diagnostics on a Chip*, Springer Berlin Heidelberg.

JOLLY, P., FORMISANO, N. & ESTRELA, P. 2015. DNA aptamer-based detection of prostate cancer. *Chemical Papers,* 69**,** 77-89.

KEIGHLEY, S. D., LI, P., ESTRELA, P. & MIGLIORATO, P. 2008. Optimization of DNA immobilization on gold electrodes for label-free detection by electrochemical impedance spectroscopy. *Biosensors and Bioelectronics,* 23**,** 1291–1297.

KELLER, F., HUNTER, M. S., ROBINSON, D. L. 1953. Structural features of oxide coatings on aluminium. *Journal of The Electrochemical Society,* 100**,** 411- 419.

KHOURY, A. & ATOUI, A. 2010. Ochratoxin A: General overview and actual molecular status. *Toxins,* 2**,** 461-493.

KIM, J. A., LEE, J. Y., SEONG, S., CHA, S. H., LEE, S. H., KIM, J. J. & PARK, T. H. 2006. Fabrication and characterization of a PDMS–glass hybrid continuous-flow PCR chip. *Biochemical Engineering Journal,* 29**,** 91-97.

KOROTKAYA, E. 2014. Biosensors: design, classification, and applications in the food industry. *Foods and Raw materials,* 2.

KOVACS, G. T. A., MALUF, N. I. & PETERSEN, K. E. 1998. Bulk micromachining of silicon. *Proceedings of the IEEE,* 86**,** 1536-1551.

KOYUN, A., AHLATCOLU, E., KOCA, Y. & KARA, S. 2012. Biosensors and their principles. *A Roadmap of Biomedical Engineers and Milestones*.

KRATZ , A., FERRARO , M., SLUSS , P. M. & LEWANDROWSKI , K. B. 2004. Normal Reference Laboratory Values. *New England Journal of Medicine,* 351**,** 1548-1563.

KUMAR, C. S. 2010. *Microfluidic devices in nanotechnology: applications.*, John Willey & Sons, Inc., Hoboken, New Jersey

KUMAR, S., KUMAR, S., ALI, M. A., ANAND, P., AGRAWAL, V. V., JOHN, R., MAJI, S. & MALHOTRA, B. D. 2013. Microfluidic-integrated biosensors: Prospects for point-of-care diagnostics. *Biotechnology Journal,* 8**,** 1267-1279.

KUMERIA, T., SANTOS, A. & LOSIC, D. 2014. Nanoporous anodic alumina platforms: engineered surface chemistry and structure for optical sensing applications. *Sensors,* 14**,** 11878-11918.

KÖHLER, M. & FRITZSCHE, W. 2007. *Nanotechnology, An Introduction to Nanostructuring Techniques*, Wiley-VCH.

LAMBERT, J., GUTHMANN, C., ORTEGA, C. & SAINT-JEAN, M. 2002. Permanent polarization and charge injection in thin anodic alumina layers studied by electrostatic force microscopy. *Journal of Applied Physics,* 91**,** 9161-9169.

LAW, C. S., SANTOS, A., NEMATI, M. & LOSIC, D. 2016. Structural Engineering of Nanoporous Anodic Alumina Photonic Crystals by Sawtooth-Like Pulse Anodization. *ACS applied materials & interfaces*.

LEE, H., WESTERVELT M., R. & HAM, D. 2007a. *CMOS Biotechnology*, Springer Science+Business Media, LLC

LEE, J.-O., SO, H.-M., JEON, E.-K., CHANG, H., WON, K. & KIM, Y. H. 2008. Aptamers as molecular recognition elements for electrical nanobiosensors. *Analytical and Bioanalytical Chemistry,* 390**,** 1023-1032.

LEE, K.-H., SU, Y.-D., CHEN, S.-J., TSENG, F.-G. & LEE, G.-B. 2007b. Microfluidic systems integrated with two-dimensional surface plasmon resonance phase imaging systems for microarray immunoassay. *Biosensors and Bioelectronics,* 23**,** 466-472.

LEE, S. W., SHANG, H., HAASCH, R. T., PETROVA, V. & LEE, G. U. 2005. Transport and functional behaviour of poly (ethylene glycol)-modified nanoporous alumina membranes. *Nanotechnology,* 16**,** 1335.

LEE, W. 2010. The anodization of aluminium for nanotechnology applications. *JOM,* 62**,** 57-63.

LEE, W., JI, R., GOSELE, U. & NIELSCH, K. 2006. Fast fabrication of long-range ordered porous alumina membranes by hard anodization. *Nat Mater,* 5**,** 741-747.

LEE, W., JIN, M.-K., YOO, W.-C. & LEE, J.-K. 2004. Nanostructuring of a polymeric substrate with well-defined nanometer-scale topography and tailored surface wettability. *Langmuir,* 20**,** 7665-7669.

LEESE, H. 2013. *Electroosmosis in Nanoporous Membranes: Connecting Material Properties to Flow Behaviour.* PhD, University of Bath.

LILLO, M. & LOSIC, D. 2009. Ion-beam pore opening of porous anodic alumina: The formation of single nanopore and nanopore arrays. *Materials Letters,* 63**,** 457-460.

LIU, C., LAGAE, L. & BORGHS, G. 2007. Manipulation of magnetic particles on chip by magnetophoretic actuation and dielectrophoretic levitation. *Applied Physics Letters,* 90.

LIU, K.-K., WU, R.-G., CHUANG, Y.-J., KHOO, H. S., HUANG, S.-H. & TSENG, F.-G. 2010a. Microfluidic systems for biosensing. *Sensors,* 10**,** 6623-6661.

LIU, X., LI, Y., ZHENG, J., ZHANG, J. & SHENG, Q. 2010b. Carbon nanotube-enhanced electrochemical aptasensor for the detection of thrombin. *Talanta,* 81**,** 1619-1624.

LUKA, G., AHMADI, A., NAJJARAN, H., ALOCILJA, E., DEROSA, M., WOLTHERS, K., MALKI, A., AZIZ, H., ALTHANI, A. & HOORFAR, M. 2015. Microfluidics integrated biosensors: A leading technology towards lab-on-A-chip and sensing applications. *Sensors (Switzerland),* 15**,** 30011-30031.

MA, K., RIVERA, J., HIRASAKI, G. J. & BISWAL, S. L. 2011. Wettability control and patterning of PDMS using UV–ozone and water immersion. *Journal of Colloid and Interface Science,* 363**,** 371-378.

MAIRHOFER, J., ROPPERT, K. & ERTL, P. 2009. Microfluidic systems for pathogen sensing: A review. *Sensors (Switzerland),* 9**,** 4804-4823.

MAJUMDER, M., CHOPRA, N., ANDREWS, R. & HINDS, B. J. 2005. Nanoscale hydrodynamics: Enhanced flow in carbon nanotubes. *Nature,* 438.

MAKAL, T. A., LI, J.-R., LU, W. & ZHOU, H.-C. 2012. Methane storage in advanced porous materials. *Chemical Society Reviews,* 41**,** 7761-7779.

MALEK, C. G. 2006. Laser processing for bio-microfluidics applications (part I). *Anal.Bioanal. Chem***,** 385, 1351–1361.

MARTINEZ, A. W., PHILLIPS, S. T., WHITESIDES, G. M. & CARRILHO, E. 2010. Diagnostics for the Developing World: Microfluidic Paper-Based Analytical Devices. *Analytical Chemistry,* 82**,** 3-10.

MARYANOFF, B. E. Q., X.; PADMANABHAN K. P.; TULINSKY A.; ALMOND, H. R.; ANDRADE-GORDON, JR. P.; GRECO, M. N.; KAUFFMAN, J. A.; NICOLAOU, K. C.; LIU, A. 1993. Molecular basis for the inhibition of human alpha-thrombin by the macrocyclic peptide cyclotheonamide A. *Proc. Natl. Acad. Sci. USA,* 90**,** 8048-8052.

MASUDA, H. & SATOH, M. 1996. Fabrication of Gold Nanodot Array Using Anodic Porous Alumina as an Evaporation Mask. *Japanese Journal of Applied Physics,* 35**,** L126.

MASUDA, H., YAMADA, H., SATOH, M., ASOH, H., NAKAO, M. & TAMAMURA, T. 1997. Highly ordered nanochannel-array architecture in anodic alumina. *Applied Physics Letters,* 71**,** 2770-2772.

MÁTÉFI-TEMPFLI, S., MÁTÉFI-TEMPFLI, M. & PIRAUX, L. 2008. Characterization of nanopores ordering in anodic alumina. *Thin Solid Films,* 516**,** 3735-3740.

MCDONALD, J. C., DUFFY, D. C., ANDERSON, J. R., CHIU, D. T., WU, H., SCHUELLER, O. J. A. & WHITESIDES, G. M. 2000. Fabrication of microfluidic systems in poly(dimethylsiloxane). *Electrophoresis,* 21**,** 27-40.

MELNGAILIS, J. 1993. Focused ion beam lithography. *Nuclear Instruments and Methods in Physics Research Section B: Beam Interactions with Materials and Atoms,* 80**,** 1271-1280.

MENAPACE, J. A., PENETRANTE, B., GOLINI, D., SLOMBA, A. F., MILLER, P. E., PARHAM, T. G., NICHOLS, M. & PETERSON, J. Combined advanced finishing and UV-laser conditioning for producing UV-damage-resistant fused-silica optics. Boulder Damage, 2002. International Society for Optics and Photonics, 56-68.

MICHALAK, D. J., AMY, S. R., AUREAU, D., DAI, M., ESTEVE, A. & CHABAL, Y. J. 2010. Nanopatterning Si(111) surfaces as a selective surface-chemistry route. *Nat Mater,* 9**,** 266-271.

MIR, M., VREEKE, M. & KATAKIS, I. 2006. Different strategies to develop an electrochemical thrombin aptasensor. *Electrochemistry Communications,* 8**,** 505-511.

MOHAMMED, M. I., HASWELL, S. & GIBSON, I. 2015. Lab-on-a-chip or Chip-in-a-lab: Challenges of Commercialization Lost in Translation. *Procedia Technology,* 20**,** 54-59.

NGUYEN, T.C., KISS, J.E., GOLDMAN, J.R. & CARCILLO, J.A., 2012. The role of plasmapheresis in critical illness. Critical care clinics, 28(3), pp.453-468

NGUYEN, N.-T. & WERELEY, S. 2006. *Fundamentals and Applications of Microfluidics,* Boston/ London, Artech Haouse.

OSMANBEYOGLU, H. U., HUR, T. B. & KIM, H. K. 2009. Thin alumina nanoporous membranes for similar size biomolecule separation. *Journal of Membrane Science,* 343**,** 1-6.

PARK, J. H. & SUDARSHAN, T. S. 2001. *Chemical Vapor Deposition*, ASM International.

PEYRET, R. 1996. *Handbook of computational fluid mechanics*, Academic Press.

PIERCE, D. T. & ZHAO, J. X. 2011. *Trace Analysis with Nanomaterials*, Wiley.

QIAN, C., HUANG, H., CHEN, L., LI, X., GE, Z., CHEN, T., YANG, Z. & SUN, L. 2014. Dielectrophoresis for bioparticle manipulation. *International journal of molecular sciences,* 15**,** 18281-18309.

RANA, J., JINDAL, J., BENIWAL, V. & CHHOKAR, V. 2010. Utility biosensors for applications in agriculture–a review. *Journal of American Science,* 6**,** 353-375.

REETZ, M.T., 2016. What are the limitations of enzymes in synthetic organic chemistry?. The Chemical Record, 16(6), pp.2449-2459.

RIVET, C., LEE, H., HIRSCH, A., HAMILTON, S. & LU, H. 2011. Microfluidics for medical diagnostics and biosensors. *Chemical Engineering Science,* 66**,** 1490-1507.

SAHA, B., TOH, W. Q., LIU, E., TOR, S. B., HARDT, D. E. & LEE, J. 2015. A review on the importance of surface coating of micro/nano-mold in micro/nano-molding processes. *Journal of Micromechanics and Microengineering,* 26.

SCHWIRN, K., LEE, W., HILLEBRAND, R., STEINHART, M., NIELSCH, K. & GÖSELE, U. 2008. Self-Ordered Anodic Aluminium Oxide Formed by H2SO4 Hard Anodization. *ACS Nano,* 2**,** 302-310.

SEYED-YAGOOBI, J. 2005. Electrohydrodynamic pumping of dielectric liquids. *Journal of Electrostatics,* 63**,** 861-869.

SINGH, P. K., SHARMA, V., TANWAR, V. K. & JAIN, S. C. 2007. Soft-lithography: Its application in solar cells, microelectronics and life sciences. *Journal of Optoelectronics and Advanced Materials,* 9**,** 127-133.

SOFLA, A. Y. N. & MARTIN, C. 2010. A vapor-assisted method for adhering polydimethylsiloxane and glass. *Lab on a chip,* 10**,** 250-253.

SOLTYSINSKI, T. 2016. Advanced Approaches to Diagnose and Treat the Chronic Autoimmune Disorders: Multimadal Molecular Imaging. *In:* FOTIADIS, D. I. (ed.) *Handbook of Research on Trends in the Diagnosis and Treatment of Chronic Conditions.* Hersey PS, USA 17033: Medical Iformation Science Reference (an imprint of IGI Global).

SONG, S., WANG, L., LI, J., FAN, C. & ZHAO, J. 2008. Aptamer-based biosensors. *TrAC Trends in Analytical Chemistry,* 27**,** 108-117.

SOPER, S. A., BROWN, K., ELLINGTON, A., FRAZIER, B., GARCIA-MANERO, G., GAU, V., GUTMAN, S. I., HAYES, D. F., KORTE, B., LANDERS, J. L., LARSON, D., LIGLER, F., MAJUMDAR, A., MASCINI, M., NOLTE, D., ROSENZWEIG, Z., WANG, J. & WILSON, D. 2006. Point-of-care biosensor systems for cancer diagnostics/prognostics. *Biosensors and Bioelectronics,* 21**,** 1932-1942.

SRINIVASAN, V., PAMULA, V., POLLACK, M. & FAIR, R. A digital microfluidic biosensor for multianalyte detection. Proceedings of the IEEE Micro Electro Mechanical Systems (MEMS), 2003. 327-330.

STANKEVIČIUS, E., GEDVILAS, M., VOISIAT, B., MALINAUSKAS, M. & RAČIUKAITIS, G. 2014. Fabrication of periodic micro-structures by holographic lithography. *Lithuanian Journal of Physics,* 53.

STEINGOETTER, I. & FOUCKHARDT, H. 2005. Deep fused silica wet etching using an Au-free and stress-reduced sputter-deposited Cr hard mask. *Journal of Micromechanics and Microengineering,* 15**,** 2130.

SUDARSAN, A.P. & Ugaz, V.M*., 2004.* Printed circuit technology for fabrication of plastic-based microfluidic devices. *Analytical chemistry*, 76(11), pp.3229-3235.

SUDARSAN, A.P., Wang, J. and Ugaz, V.M., 2004, September. Novel thermoplastic elastomers for microfluidic device construction. In Proc. MicroTAS (Vol. 2, pp. 22-24)

LAURELL, T. & CHEMISTRY, R. S. O. (eds.) *Micro Total Analysis Systems 2004: Proceedings of [Mu] TAS 2004 8th International Conference on Miniaturized Systems for Chemistry and Life Sciences, Malmö, Sweden, September 26-30, 2004.* Royal Society of Chemistry.

SULKA, G. 2008. 2008. Highly ordered anodic porous alumina formation by self-organized anodizing. Nanostructured materials in electrochemistry, 1, pp.1-116.

EFTEKHARI, A. (ed.) *Nanostructured materials in electrochemistry.* John Wiley & Sons, 2008.

TANG, K., LIAO, E., ONG, W., WONG, J., AGARWAL, A., NAGARAJAN, R. & YOBAS, L. Evaluation of bonding between oxygen plasma treated polydimethyl siloxane and passivated silicon. Journal of Physics: Conference Series, 2006. IOP Publishing, 155.

TERRY, S. C., JERMAN, J. H. & ANGELL, J. B. 1979. A gas chromatographic air analyzer fabricated on a silicon wafer. *IEEE Transactions on Electron Devices,* 26**,** 1880-1886.

WANG, Y., BAO, L., LIU, Z. & PANG, D.-W. 2011. Aptamer Biosensor Based on Fluorescence Resonance Energy Transfer from Upconverting Phosphors to Carbon Nanoparticles for Thrombin Detection in Human Plasma. *Analytical Chemistry,* 83**,** 8130-8137.

WANG, H., CHEN, L. & SUN, L., 2017. Digital microfluidics: A promising technique for biochemical applications. Frontiers of Mechanical Engineering, 12(4), pp.510-525.

WASHBURN, E. W. 1926 - 1930; 2003. *International Critical Tables of Numerical Data, Physics, Chemistry and Technology*.

WINKLER, T., BALLAV, N., THOMAS, H., ZHARNIKOV, M. & TERFORT, A. 2008. Micrometer-Scale Protein-Resistance Gradients by Electron-Beam Lithography. *Angewandte Chemie International Edition,* 47**,** 7238-7241.

WU, J. & GU, M. 2011. Microfluidic sensing: state of the art fabrication and detection techniques. *Journal of Biomedical Optics,* 16**,** 080901-080901-12.

XIAO, K. & GRIER, D. G. 2010. Sorting colloidal particles into multiple channels with optical forces: Prismatic optical fractionation. *Physical Review E,* 82**,** 051407.

YAN, F., ESTRELA, P., MO, Y., MIGLIORATO, P. & MAEDA, H. 2005. Polycrystalline silicon ISFETs on glass substrate. *Sensors,* 5**,** 293-301.

YASUDA, H. & WANG, C. 1985. Plasma polymerization investigated by the substrate temperature dependence. *Journal of Polymer Science: Polymer Chemistry Edition,* 23**,** 87-106.

YOO, E.-H. & LEE, S.-Y. 2010. Glucose biosensors: an overview of use in clinical practice. *Sensors,* 10**,** 4558-4576.

YU, Y. & ZHANG, G. 2013. Colloidal Lithography. *Updates in Advanced Lithography; Hosaka, S., Ed.; InTech*.

ZALEVSKY, Z. & ABDULHALIM, I. 2014. *Integrated nanophotonic devices*, Elsevier.

ZAYTSEVA, N. V., GORAL, V. N., MONTAGNA, R. A. & BAEUMNER, A. J. 2005. Development of a microfluidic biosensor module for pathogen detection. *Lab on a Chip - Miniaturisation for Chemistry and Biology,* 5**,** 805-811.

ZHANG, C., XU, J., MA, W. & ZHENG, W. 2006. PCR microfluidic devices for DNA amplification. *Biotechnology Advances,* 24**,** 243-284.

ZhAO, C., Illumina Inc, 2016. Efficient biomolecule recycling method and system. U.S. Patent 9,322,063.

ZHANG, Q. & AUSTIN, R. H. 2012. Applications of Microfluidics in Stem Cell Biology. *BioNanoScience,* 2**,** 277-286.

ZHOU, Q., KWA, T., GAO, Y., LIU, Y., RAHIMIAN, A. & REVZIN, A. 2014. On-chip regeneration of aptasensors for monitoring cell secretion. *Lab on a Chip,* 14**,** 276-279.

Back cover

PhD 2019 S.BEKOU
